

Solution-processed $\text{Cu}_2\text{ZnSn}(\text{S}_x\text{Se}_{1-x})_4$ thin films based on binary and ternary chalcogenide nanoparticle precursors and their application in solar cells

vorgelegt von
Xianzhong Lin
aus **Guangdong, China**

von der Fakultät III - Prozesswissenschaften
der Technischen Universität Berlin
zur Erlangung des akademischen Grades

Doktor der Ingenieurwissenschaften
-Dr.-Ing.-

genehmigte Dissertation

angefertigt am Helmholtz-Zentrum Berlin für Materialien und Energie
Institut für Heterogene Materialsysteme

Promotionsausschuss:

Vorsitzender: Prof. Dr. Frank Behrendt

Berichter: Prof. Dr. John Banhart

Berichter: Prof. Dr. Martha Ch. Lux-Steiner

Tag der wissenschaftlichen Aussprache: 15 November 2013

Berlin, 2013

D83

Abstract

$\text{Cu}_2\text{ZnSn}(\text{S}_x\text{Se}_{1-x})_4$ (CZTSSe) is considered as a promising candidate for low-cost and high efficiency solar cells. In this thesis a cost-effective solution processing for the deposition of CZTSSe thin film absorbers by spin coating of ZnS, SnS and Cu_3SnS_4 (CTS) nanoparticles inks was developed. CZTSSe thin films were deposited by a four-step process.

In the first step, ZnS, SnS and CTS nanoparticles were separately synthesized by a heating-up colloidal route using oleylamine as both solvent and surfactant. ZnS, SnS and CTS nanoparticles were mixed together in hexanthiol to form stable inks, which were used as the precursors for the formation of CZTSSe thin films. In the second step, the Cu-Zn-Sn-S precursors' thin films were deposited by spin coating of the ZnS, SnS and CTS nanoparticle inks. To remove the solvent and surfactant surrounding the nanoparticles, heat treatments at 170°C and 350°C were carried out as a third step. The Designed thickness can be achieved by repeating step two and step three. To form the $\text{Cu}_2\text{ZnSn}(\text{S}_x\text{Se}_{1-x})_4$ ($0 \leq x < 1$) absorbers, an annealing step was carried out in the temperature range between 400°C and 580°C under sulfur/selenium-containing atmosphere.

Prior to the deposition of CZTSSe thin films, the structural and morphological properties and the stoichiometry of the ZnS, SnS and CTS nanoparticles were characterized by X-ray diffraction (XRD), transmission electrons microscop (TEM) and energy-dispersive X-ray spectroscopy (EDX). The growth kinetic of CTS nanoparticles was studied by taking out aliquots from the reaction solution throughout the reaction and analyzing them by TEM. The influence of the reaction temperature and precursor ratio of SnCl_2 : S on the structure and morphology of the resulting nanoparticles was studied.

The influence of the annealing temperature (400 – 580 °C) and atmosphere (Ar-Se and Ar- H_2S (5%)) on morphological and structural properties of the resulting CZTSSe films was studied by means of scanning electron microscopy (SEM), XRD and Raman spectroscopy. It was found that annealing in Se-containing atmosphere was necessary for grain growth. To reduce the carbon content arising from organic surfactant of the nanoparticle precursors in the resulting CZTSSe thin films, an additional ligand-exchange with a $(\text{NH}_4)_2\text{S}$ step was performed before going to the heat treatment at 350 °C. The influence of the ligand-exchange process on the morphological properties of the resulting CZTSSe thin films was studied.

Abstract

To study the defect properties of CZTSSe thin films prepared under different conditions, temperature and excitation power dependent photoluminescence (PL) spectroscopy measurements were performed. CZTSSe thin films generally show broad emission spectra involving donor-acceptor pair recombination. The PL peak energies shift towards lower energies and the PL signals increase with increasing selenium content in CZTSSe thin films.

The effect of the processing conditions of CZTSSe thin films on the surface photovoltage (SPV) properties was studied. The SPV signals strongly increased with decreasing sulfur content in CZTSSe. A diffusion length of above 1 μm was estimated for photo-generated electrons in $\text{Cu}_2\text{ZnSn}(\text{S}_x\text{Se}_{1-x})_4$ thin films with $x=0.28$. $[\text{Zn}_{\text{Sn}} + \text{Zn}_{\text{Cu}}]$ defect clusters were found in $\text{Cu}_2\text{ZnSn}(\text{S}_x\text{Se}_{1-x})_4$ thin films with $x=0.28$ using the temperature dependent SPV measurements.

Finally, as a proof of concept, the CZTSSe-based thin film solar cells were fabricated. The photovoltaic performance of the devices was studied by current density-voltage and quantum efficiency measurements. By optimizing the deposition procedures of CZTSSe thin films, devices with efficiencies up to 3.0 % were achieved. Temperature-dependent j-V analysis revealed that the loss mechanism of the device performance was dominated by the CZTSSe/CdS interface recombination.

Zusammenfassung

$\text{Cu}_2\text{ZnSn}(\text{S}_x\text{Se}_{1-x})_4$ (CZTSSe) ist ein vielversprechendes Material um günstige Solarzellen mit hoher Effizienz herzustellen. In dieser Arbeit wurde ein kosteneffizienter Prozess für die Abscheidung von dünnen Schichten aus CZTSSe Absorbern entwickelt. Mittels Rotationbeschichtung von ZnS, SnS und Cu_3SnS_4 (CTS) Nanopartikel-Tinte wurden die CZTSSe Absorber in einem vierstufigen Prozess hergestellt.

Im ersten Schritt werden jeweils ZnS, SnS und CTS Nanopartikel durch Aufheizen in einem kolloidalen Prozess mit Oleylamin als Lösungsmittel und als Ligand hergestellt. Die ZnS, SnS und CTS Nanopartikel bilden eine stabile Tinte, wenn sie in Hexanthiol gemischt werden. Diese Tinte dient als Präkursor zur Bildung von CZTSSe Dünnschichten. Im zweiten Schritt wird die Cu-Zn-Sn-S Präkursor dünnschicht mittels Rotationsbeschichtung von der ZnS/SnS/CTS-Nanopartikel-Tinte aufgebracht. Um das Lösungsmittel und die Liganden von den Nanopartikeln zu entfernen, wird ein Ausheizprozess bei 170 °C und 350 °C durchgeführt. Hierbei handelt es sich um den dritten Prozessschritt. Durch die Wiederholung des zweiten und des dritten Schrittes kann die Schichtdicke variiert werden. Um den $\text{Cu}_2\text{ZnSn}(\text{S}_x\text{Se}_{1-x})_4$ ($0 \leq x < 1$) Absorber herzustellen, wird ein Ausheizschritt bei Temperaturen zwischen 400 °C und 580 °C in einer Schwefel/Selen Atmosphäre durchgeführt.

Vor der Abscheidung der CZTSSe Dünnschichten wurden die strukturellen und morphologischen Eigenschaften und die Stöchiometrie der ZnS, SnS und CTS Nanopartikel mittels Röntgendiffraktometrie (XRD), Transmissionselektronenmikroskopie (TEM) und Energie dispersiver Röntgenspektroskopie (EDX) charakterisiert. Die Wachstumskinetik der CTS Nanopartikel wurde durch Entnahme aliquoter Teile der Reaktionslösung während der Reaktion studiert, indem sie mit dem TEM analysiert wurden. Der Einfluss der Reaktionstemperatur und das Präkursorverhältnis von SnCl_2 : S auf die Struktur und Morphologie der resultierenden Nanopartikel wurde untersucht.

Der Einfluss der Ausheiztemperaturen (400 °C – 580 °C) und der Atmosphären (Ar-Se und Ar- H_2S (5%)) auf die morphologischen und strukturellen Eigenschaften der CZTSSe Schichten wurde mit Hilfe der Rasterelektronenmikroskopie (REM), XRD und Raman Spektroskopie untersucht. Dabei wurde herausgefunden, dass das Ausheizen in Selenhaltiger Atmosphäre für das Kornwachstum notwendig ist.

Um den Kohlenstoffgehalt zu reduzieren, der sich aus den organischen Lösungsmitteln der Nanopartikel Präkursor ergibt, wurde ein zusätzlicher Ligandenaustausch mit $(\text{NH}_4)_2\text{S}$ vor der Ausheizbehandlung bei 350°C durchgeführt. Der Einfluss dieses Schrittes auf die Morphologie der resultierenden CZTSSe Schichten wurde untersucht.

Um die Defekteigenschaften der CZTSSe Dünnschichten, die unter verschiedenen Versuchsbedingungen hergestellt wurden, zu untersuchen, wurden temperatur- und anregungsintensitätsabhängige Photolumineszenz (PL) Messungen durchgeführt. CZTSSe Dünnschichten zeigen ein weites Emissionsspektrum mit Donor-Akzeptor-Paar Rekombinationen. Die Energien der PL Maxima verschieben sich zu niedrigeren Energien und das PL Signal wächst mit steigendem Selengehalt in den Schichten.

Der Einfluss der Prozessbedingungen zur Herstellung von CZTSSe Dünnschichten auf die SPV Spektren wurde untersucht. Das SPV Signal wächst mit abnehmendem Schwefel Gehalt. Eine Diffusionslänge über $1 \mu\text{m}$ konnte für photogenerierte Elektronen in $\text{Cu}_2\text{ZnSn}(\text{S}_x\text{Se}_{1-x})_4$ Dünnschichten mit $x = 0.28$ abgeschätzt werden. Mit Hilfe von Temperaturabhängigen SPV Messungen wurden $[\text{Zn}_{\text{Sn}} + \text{Zn}_{\text{Cu}}]$ Defektcluster in $\text{Cu}_2\text{ZnSn}(\text{S}_x\text{Se}_{1-x})_4$ Dünnschichten mit $x = 0.28$ gefunden.

Schlussendlich wurden zum Überprüfen des gesamten Prozesses CZTSSe basierte Dünnschichtsolarzellen hergestellt. Die photovoltaischen Eigenschaften dieser Solarzellen wurden mit Hilfe von Strom-Spannungs-Messungen und Quanteneffizienzmessungen eingehend studiert. Durch Optimierung der Abscheideprozeduren von CZTSSe Dünnschichten wurden Wirkungsgrade bis zu 3.0 % erzielt. Temperaturabhängige Strom-Spannungs-Messungen zeigen, dass die Verluste, die sich negativ auf die Bauteilleistung auswirken, hauptsächlich durch Rekombination an der CZTSSe/CdS Grenzfläche hervorgerufen werden.

Aknowledgments

It is a great fortune for me to be able to work as a PhD student in Helmholtz-Zentrum Berlin für Materialien und Energie (HZB). I had a great time in the past three years. Here I would like to express my gratitude to all those helping me during my PhD.

First and foremost I would like to thank Prof. Dr. Martha Ch. Lux-Steiner for offering me the opportunity to carry out my PhD thesis in her department at HZB, for the comments and suggestions during every montalk, for spending time on discussion with me throughout this work. I would like to thank Prof. Dr. John Banhart for accepting to be my first supervisor and for the helpful suggestions and discussions on my thesis.

I would like to express my special gratitude to Dr. Ahmed Ennaoui who introduced me to Physical Chemistry Lab and has been helping me since the first day that I came into the Group. Thank you for your guidance on this work. I would also like to thank all the current and former members in Physical Chemistry Group for all the discussions, and the helps in the lab. Particularly, I would like to thank Björn Eckhardt who helped me to get familiar with the lab during the start of the PhD and also Jaison Kavalakkatt who has been helping me on the SEM and Raman spectroscopy measurements.

I am grateful to PD Dr. Thomas Dittrich for introducing me to surface photovoltage measurement, allowing me to carry out the SPV measurement in his lab, and discussing with me on the SPV results. Not to forget Prof. Dr. Susan Schorr for helping me on the analysis of the XRD data and Dr. Sergiu Levcenko for the help on PL measurements and the discussions of the PL results.

Many thanks to Dr. Daniel Abou-Ras and Ulli Bloeck for their help on TEM sample preparation and measurements. I would like to thank Carola Kelch and Michael Kirsch for the helping on deposition of CdS, ZnO, ZnO: Al and grids and Joachim Klaer and Bianka Bunn for the preparation of the Mo substrates. I would like to thank all those who helped me during PhD work but the names are not mentioned above.

I would like to thank China Scholarship Council, Helmholtz Association and HZB for the financial support during my PhD studies.

Aknowledgements

Last but not least, I want to express my deepest gratitude to my parents and my brothers who have been supporting and encouraging me all the time.

List of Abbreviations

AM1.5G	Air Mass 1.5 Global
Ar	Argon
C	Carbon
CB	Conduction Band
CCD	Charge coupled device
CdS	Cadmium sulfide
CIGS	Copper indium gallium sulfide($\text{Cu}_2\text{ZnSnS}_4$)
CTS	Copper tin sulfide (Cu_3SnS_4)
Cu	Copper
Cu_2S	Copper(I) sulfide
CuS	Cooper (II) sulfide
CZTS	Copper zinc tin sulfide($\text{Cu}_2\text{ZnSnS}_4$)
CZTSe	Copper zinc tin selenide($\text{Cu}_2\text{ZnSnSe}_4$)
CZTSSe	Copper zinc tin sulfide selenide ($\text{Cu}_2\text{ZnSn}(\text{S}_x\text{Se}_{1-x})_4$)
DAP	Donor acceptor pair
DDT	1-dodecanethiol
EDX	Energy Dispersive X-ray spectroscopy
EQE	External quantum efficiency
FF	Fill factor
FTO	Fluorine-doped tin oxide
FWHM	Full Width at Half Maximum
HCl	Hydrochloric acid
HRTEM	High-resolution transmission electron microscopy
H_2S	Hydrogen sulfide
IQE	Internal quantum efficiency
ITO	Tin doped indium oxide
IVT	Temperature dependent current-voltage characteristic
JCPDS	Joint Committee on Powder Diffraction Standards
J_{sc}	Short circuit current density

List of Abbreviations

J-V	Current density - voltage
KCN	Potassium cyanide
Mo	Molybdenum
MoS ₂	Molybdenum disulfide
MoSe ₂	Molybdenum diselenide
NCs	Nanocrystals
(NH ₄) ₂ S	Ammonium sulfide
O	Oxygen
OLA	Oleylamine
PL	Photoluminescence
QE	Quantum efficiency
RF	Radio frequency
S	Sulfur
SCR	Space charge region
Se	Selenium
SEM	Scanning electron microscopy
Sn	Tin
SnO	Tin oxide
SnO ₂	Tin dioxide
SnS	Tin sulfide
SnS ₂	Tin disulfide
SPV	Surface photovoltage
TEM	Transmission electron microscopy
VB	Valence Band
VOC	Open circuit voltage
XRD	X-ray diffraction
Zn	Zinc
ZnO	Zinc oxide
ZnO: Al	Aluminum doped zinc oxide
ZnS	Zinc sulfide

Content

Abstract	I
Acknowledgments.....	V
List of Abbreviations.....	VII
1 Introduction	1
2 Materials properties and development of $\text{Cu}_2\text{ZnSn}(\text{S}_x\text{Se}_{1-x})_4$ thin film solar cells	4
2.1 Material properties of $\text{Cu}_2\text{ZnSn}(\text{S}_x\text{Se}_{1-x})_4$	4
2.2 Evolution of $\text{Cu}_2\text{ZnSn}(\text{S}_x\text{Se}_{1-x})_4$ thin film solar cell efficiency.....	6
2.3 $\text{Cu}_2\text{ZnSn}(\text{S}_x\text{Se}_{1-x})_4$ thin film deposition techniques	7
2.3.1 Vacuum-based techniques.....	8
2.3.1.1 Sputtering.....	8
2.3.1.2 Evaporation	9
2.3.1.3 Pulsed laser deposition	10
2.3.2 Non-vacuum solution-based techniques	11
2.3.2.1 Precursor-ink based approach	11
2.3.2.2 Spray pyrolysis	13
2.3.2.3 Electrochemccal deposition	13
2.3.2.4 Nanoparticle-based approach	15
3 Colloidal synthesis of ZnS, SnS and Cu_3SnS_4 nanoparticles	17
3.1 Basic of nanoparticle growth	17
3.1.1 General synthesis strategies	17
3.1.2 Nucleation and growth	19
3.2 Synthesis of nanoparticles	22
3.3 Results and discussions	24
3.3.1 ZnS nanoparticles.....	24
3.3.2 SnS nanoparticles	27
3.3.3 Cu_3SnS_4 nanoparticles	32
3.3.3.1 Characterization of Cu_3SnS_4 nanoparticles	32
3.3.3.2 Statistic analysis of Cu_3SnS_4 growth.....	35

Content

3.3.3.3 Growth mechanism of Cu_3SnS_4 nanoparticles	38
3.3.3.4 Influence of reaction condition on the resulting nanoparticles	39
3.4 Summary	40
4 Preparation, morphology and structure of $\text{Cu}_2\text{ZnSn}(\text{S}_x\text{Se}_{1-x})_4$ thin films.....	42
4.1 Preparation of $\text{Cu}_2\text{ZnSn}(\text{S}_x\text{Se}_{1-x})_4$ thin films.....	42
4.2 Results and discussions	45
4.2.1 Influence of the annealing temperature and atmosphere	45
4.2.1.1 Morphology analyzed by SEM	45
4.2.1.2 Structural characterization by XRD and Raman spectroscopy	53
4.2.2 Influence of ligand exchange on the morphology	66
4.2.2.1 Surface morphology.....	66
4.2.2.2 Cross sectional morphology and EDX analysis.....	68
4.3 Summary	71
5 Photoluminescence spectroscopy studies of $\text{Cu}_2\text{ZnSn}(\text{S}_x\text{Se}_{1-x})_4$ thin film	73
5.1 Basics of photoluminescence.....	73
5.2 Photoluminescence measurements	76
5.3 Results and discussions.....	77
5.3.1 Excitation power dependent photoluminescence analysis	77
5.3.2 Temperature dependent photoluminescence analysis	80
5.4 Summary	83
6 Surface photovoltage analysis of $\text{Cu}_2\text{ZnSn}(\text{S}_x\text{Se}_{1-x})_4$ thin films	85
6.1 Basics of surface photovoltage	85
6.2 Surface photovoltage measurements.....	88
6.3 Results and discussions	89
6.4 Summary	95
7 Photovoltaic performance of $\text{Cu}_2\text{ZnSn}(\text{S}_x\text{Se}_{1-x})_4$ thin film absorbers	96
7.1 Basics of solar cells.....	96
7.1.1 Characteristic parameters of solar cells.....	96
7.1.2 Diode characteristic of solar cells	97

Content

7.1.3 Quantum Efficiency.....	98
7.2 Solar Cells fabrication and characterization	99
7.3 Current-Voltage characteristics and external quantum efficiency.....	100
7.4 Temperature dependent current-voltage characterization	104
7.5 Summary	106
8 Summary	107
Appendix A.....	110
A.1 Overview of samples used for PL and SPV analysis	110
A.2 Relative chemical composition of samples used for PL analysis	110
A.3 XRD patterns of samples used for PL and SPV analysis	111
A.4 EDX line scanning profile of precursors' films	112
Appendix B Synthesis of $\text{Cu}_2\text{Zn}_x\text{Sn}_y\text{Se}_{1+x+2y}$ nanocrystals with wurtzite-derived structure .	113
B.1 Introduction	113
B.2 Experimental details	114
B.3 Results and discussion	116
B.4 Conclusions	123
B.5 Simulation diffraction pattern of kesterite type, wurtzite type and wurtz-stannite type CZTSe	124
References	126
List of publications	142
Curriculum Vitae	144
Declaration	145

Content

1 Introduction

Energy is a great issue for the development of society. Since the amount of fossil fuel is limited, a sustainable development of society requires the development of novel sustainable energy resources. In such a context, solar energy meets the requirement. Recently, Cu(In,Ga)Se₂-based thin film solar cells have achieved efficiencies as high as 20.4 % in the lab scale [1]. However, due to the scarcity and high cost of indium constituent, this material cannot meet the long term goal of the solar energy development. To solve this issue, it is necessary to develop alternative light absorbing materials which are composed of relatively earth abundant elements. In recent years, kesterite CuZnSn(S_xSe_(1-x))₄ with $0 \leq x \leq 1$ (CZTSSe) has emerged as one of the promising candidates for thin film solar cells due to its direct optical band gap of 1.0 to 1.5 eV, high absorption coefficient (over 10^4 cm^{-1}) above the optical band gap and abundant elements on Earth [2, 3]. The CuZnSn(S_xSe_(1-x))₄-based thin film solar cells have achieved an efficiency as high as 11.1 % using a hydrazine-based processing CZTSSe absorbers [4]. This device performance points to the significant promise of CZTSSe as emerging and interesting materials for solar cell applications. However, hydrazine is toxic and explosive, and therefore not favorable for further up-scaling development. Therefore, an alternative deposition approach for the CZTSSe thin film absorber is preferable.

In this thesis, a solution processed approach for the deposition of CZTSSe thin film absorbers is presented using binary and ternary chalcogenide nanoparticles as precursors. The aim of this work is firstly to develop a solution deposition process for CZTSSe thin film absorbers, which does not rely on hydrazine solvent and secondly to study the influence of the processing conditions such as ink precursors and annealing conditions on the structural, optical and electrical properties of CZTSSe thin film absorbers.

In the following, a brief description of the structure of this thesis and the main contents is given.

Chapter 2 starts with a brief introduction of the material properties of CZTSSe and the evolution of Cu₂ZnSn(S_xSe_{1-x})₄-based thin film solar cell efficiency. Furthermore, a literature review on the advance of various deposition techniques for CZTSSe thin films and the best

solar cells fabricated by the corresponding techniques is presented. The deposition techniques are divided into two major categories: vacuum-based processes and non-vacuum solution-based processes. On the one hand, in the vacuum-based processes, sputtering, evaporation and pulsed laser deposition techniques for CZTSSe are reviewed [2, 5, 6]. On the other hand, in the non-vacuum solution-based processes, a review of the precursor-ink based approach, spray pyrolysis, electrochemical deposition, and nanoparticle-based approach is presented [4, 7-9].

Chapter 3 describes the colloidal synthesis of ZnS, SnS and Cu₃SnS₄ nanoparticle precursors using one pot technique. This chapter starts with a brief introduction of the nucleation and crystal growth theory in colloidal chemistry, followed by the experimental details of synthesis of ZnS, SnS and Cu₃SnS₄ nanoparticles. In particular, the influence of the different reaction conditions such as reaction temperatures and reaction precursors on the morphology and phases of the final nanoparticles is described. Finally, the growth kinetic and mechanism of Cu₃SnS₄ nanoparticles are discussed.

Chapter 4 describes the preparation of CuZnSn(S_xSe_{1-x})₄ thin films by annealing the precursors' thin films deposited by successive spin coating of ZnS, SnS and Cu₃SnS₄ nanoparticle ink precursors. The influence of the annealing temperature and atmosphere on the morphology and structure properties of CZTSSe thin films has been discussed. The influence of the ligand-exchange procedures on the morphology of CZTSSe thin films has also been explored. The morphology of CZTSSe thin films has been analyzed by scanning electron microscopy while the structural properties of CZTSSe thin films have been characterized by X-ray diffraction accompanied with Raman spectroscopy.

Chapter 5 describes the defect properties of the CZTSSe thin film absorbers by excitation power dependent and temperature dependent photoluminescence spectroscopy measurements. After a brief introduction of radiative recombination mechanisms, the dominant emissions related to defect states are discussed in the samples prepared under different conditions.

Chapter 6 describes the surface photovoltage (SPV) properties of CZTSSe thin films deposited by different conditions. The aim of this chapter is to show the correlation between the SPV with the processing conditions of the p-type CZTSSe thin films, which helps to optimize the deposition procedure. This chapter firstly starts with a brief introduction on SPV

theory [10, 11] followed by the SPV analysis of CZTSSe samples. The diffusion length of electrons was determined by the modulated SPV.

Chapter 7 studies the performance of $\text{Cu}_2\text{ZnSn}(\text{S}_x\text{Se}_{1-x})_4$ thin films solar cells with Mo/CZTSSe/CdS/ZnO/ZnO:Al/Ni:Al structures. In the beginning, a brief introduction into the theoretical background of solar cells is presented. Furthermore, the fabrication process of the solar cells is described. Finally, a discussion of solar cell performance as characterized by current-voltage characteristics under dark and illumination and by external quantum efficiency is presented. To learn more about the loss mechanism of device performance, temperature dependent current voltage characteristics are analyzed.

This work is completed with a summary and a brief outlook for the further improvement of solar cell performance.

2 Materials properties and development of $\text{Cu}_2\text{ZnSn}(\text{S}_x\text{Se}_{1-x})_4$ thin film solar cells

In this chapter, I will first introduce the fundamental properties of $\text{Cu}_2\text{ZnSn}(\text{S}_x\text{Se}_{1-x})_4$ (CZTSSe). Then I will give a brief review on the deposition method for CZTSSe thin films as well as the evolution of CZTSSe-based thin film solar cells.

2.1 Material properties of $\text{Cu}_2\text{ZnSn}(\text{S}_x\text{Se}_{1-x})_4$

Thin film solar cells based on $\text{Cu}(\text{In,Ga})\text{Se}_2$ (CIGS) have reached the commercialization stage; however, due to the limitation supply and high cost of the indium, this materials cannot meet the long term large scale solar energy development. To solve this issue, it is necessary to develop alternative light absorbing materials which contain earth-abundant constituents. In this context, CZTS(Se) has emerged as one of the most promising candidates for low cost, high efficiencies thin film solar cells. Similar to $\text{Cu}(\text{In,Ga})\text{Se}_2$, CZTSSe is a p-type semiconductor materials but contains much more earth-abundant constituents. Fig.2.1 illustrates the abundances of the elements in nature.

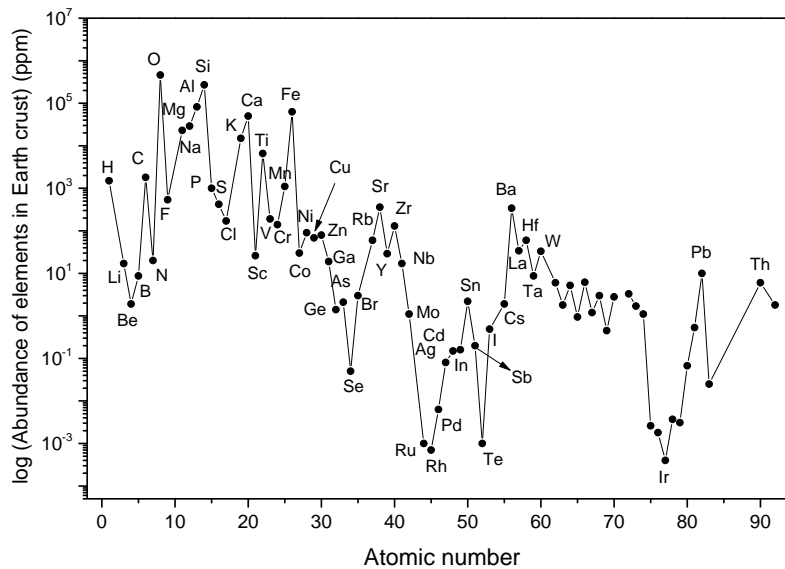


Figure 2.1 Abundances of the chemical elements in the Earth crust [12]

The optical band gap of $\text{Cu}_2\text{ZnSn}(\text{S}_x\text{Se}_{1-x})_4$ thin films can be tuned from 1.0 eV to 1.5 eV by tailoring the ratio of sulfur to selenium in the samples. This optical band gap matches the

solar spectrum very well and therefore this material is ideal for solar energy conversion. Moreover, the optical absorption coefficient of the CZTSSe is over 10^4 cm^{-1} for the light with the energy over the band gap, which means that a very thin layer (1-2 μm) is enough to absorb the incident light [13].

Generally, there are two types well-known tetragonal structure for CZTS(Se) compounds, kesterite type structure and stannite type structure [14]. Both structures consist of a ccp array of anions, with cations occupying one half of the tetragonal voids. Due to the different distribution of the cations, the structures can be attributed to different space groups; with kesterite belonging to $(I\bar{4})$ while stannite belonging to $(I\bar{4}2m)$. When the ordering of the metals is such that Cu and Sn atoms alternate on the $z=0$ and $\frac{1}{2}$ (z =fractional coordinate along the long c -axis of the structure) planes and Cu and Zn atoms alternate on the $z=\frac{1}{4}$ and $\frac{3}{4}$ planes, this is known as the kesterite structure, whereas when Zn and Sn atoms alternate on the $z=0$ and $\frac{1}{2}$ planes and only Cu resides on the $z=\frac{1}{4}$ and $\frac{3}{4}$ planes, this is known as the stannite structure [3, 14]. The schematic representation of the unit cells of kesterite type and stannite type CZTS(Se) was shown in Figure 2.2. Generally, kesterite type structure is the ground-state structure for both CZTS and CZTSe, which has been demonstrated experimentally [14] and theoretically [15]. However, the energy difference between kesterite type and stannite type structures is very small; only about 3 meV per atom, indicating that stannite type structure may also exist under standard preparation conditions.

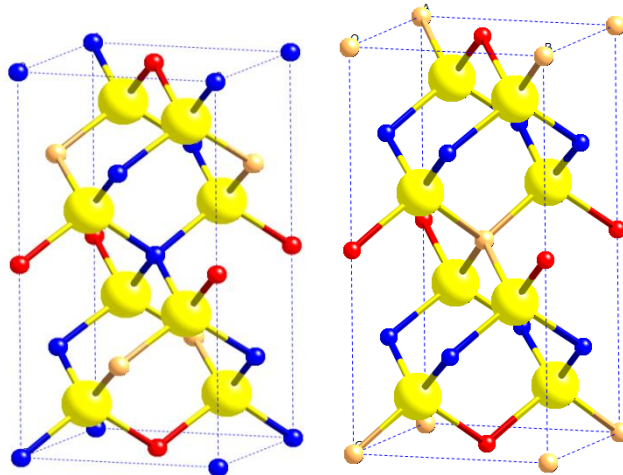


Figure 2.2 Schematic representation of the unit cells of kesterite type (left) and stannite type (right) CZTS(Se) (blue – Cu; orange – Zn; red – Sn; yellow – S/Se)

Since the their potential application of these materials as absorber layers in thin film photovoltaic, these materials have attracted great interest both in scientific and industrial areas in recent years, which can be demonstrated by the evolution of number of publications each year (see Figure 2.3).

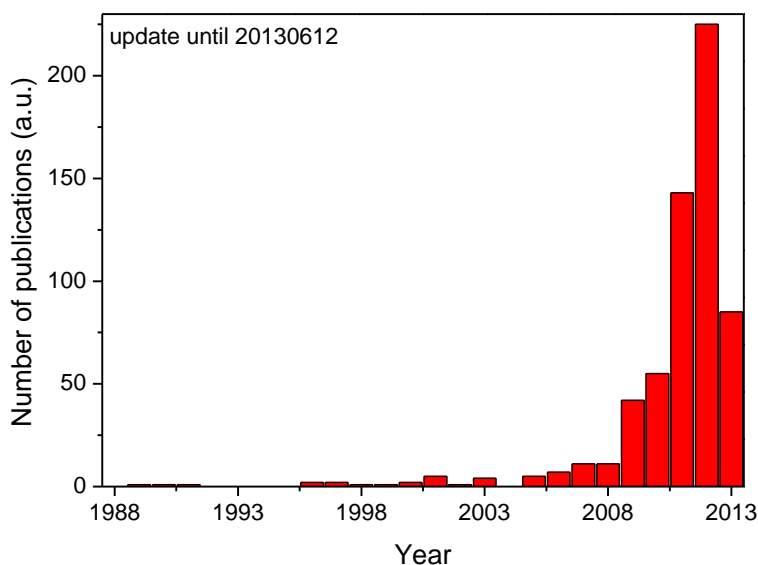


Figure 2.3 Evolution of number of publications per year for $\text{Cu}_2\text{ZnSn}(\text{S}_x\text{Se}_{1-x})_4$ with $0 \leq x \leq 1$ materials undated to June 2013. The number of publication was obtained from the database of Web of Science.

2.2 Evolution of $\text{Cu}_2\text{ZnSn}(\text{S}_x\text{Se}_{1-x})_4$ thin film solar cell efficiency

The first reported photovoltaic effect of CZTS was in 1988 by Iko and Nakazawa from Shinshu University, Japan [2]. They fabricated a heterojunction diode which consisted of a transparent cadmium-tin-oxide thin film and a CZTS thin film on a stainless substrate. The fabricated device gave an open circuit voltage of 165 mV under AM1.5 illumination. In 1997, Katagiri *et al.* [16] reported the first CZTS thin film solar cell devices with a ZnO:Al/CdS/CZTS/Mo/soda lime glass structure. The best device showed an open circuit voltage of 400 mV and a conversion efficiency of 0.66%. The CZTS thin films were prepared by sulfurization of the electron beam deposited Cu/Sn/Zn stacked precursors. In the same year, Friedlmeier *et al.*¹ fabricated thin film solar cells using CZTS as the light absorbing layer showing the best conversion efficiency 2.3% with an open circuit voltage of 470 mV [17]. A

new record, 2.62 %, was set in 1999 by Katagiri *et al.*[17] who prepared the CZTS thin films by sulfurization of Cu/Sn/ZnS stacks deposited by vacuum process. By optimization the annealing process, the efficiency was increased to 5.45 % in 2003 by the same group [17]. In 2008, Katagiri *et al.* found that soaking of CZTS thin films in deionized water allows the etching of the metal oxide particles in the CZTS layer resulting in the device efficiency of 6.7 % [18]. This efficiency was the record efficiency until 2010 where Mitzi *et al.* reported 9.6 % efficient solution processed CZTSSe solar cells [19]. The CZTSSe absorber layers for these devices were deposited using solution process by spin-coating precursors containing metal binary chalcogenides dissolved in hydrazine followed by sulfurization or selenization. In 2011, the efficiency was further improved to 10.1 % by the same group [20, 21]. The latest reported conversion efficiency for CZTSSe-based solar cells was increased to 11.1 % by the same group, which is currently the highest efficiency for CZTS(Se)-based thin film solar cells. The evolution of the conversion efficiency of CZTS(Se)-based thin solar cells has been summarized in Figure 2.3.

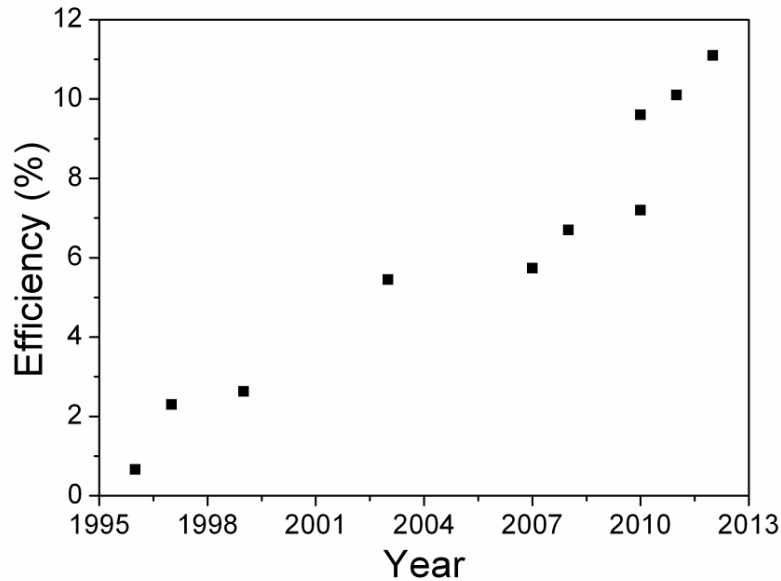


Figure 2.3 Evolution of the record efficiency of CZTS(Se) solar cells as a function of years.

2.3 $\text{Cu}_2\text{ZnSn}(\text{S}_x\text{Se}_{(1-x)})_4$ thin film deposition techniques

CZTSSe thin films have been deposited by a variety of techniques such as evaporation, sputtering, spin coating, and screen printing and so on. All these methods can be summarized

as two major categories: vacuum-based processes and non-vacuum solution-based processes. In the following section, we will review the advance of various deposition techniques for CZTSSe thin films and the best solar cells fabricated from the corresponding techniques.

2.3.1 Vacuum-based techniques

The vacuum-based deposition techniques, including sputtering, evaporation and pulsed laser deposition, mainly involve the deposition of CZTSSe constituents such as metal or binary chalcogenides on substrates under certain temperature and low pressure. The most pronounced advantages for these techniques are the easy control of stoichiometry and the homogeneity of the resulting thin films.

2.3.1.1 Sputtering

Sputtering deposition technique is a physical vapour deposition method, which involves ejecting material from a target that is a source onto a substrate. Various types of sputtering techniques such as argon beam, DC, RF, hybrid and reactive magnetic sputtering have been employed to deposit CZTSSe thin films [2, 18, 22-27].

In 1988, Iko *et al.* [2] first reported on the deposition of CZTS thin films using the argon beam sputtering from the pressed target composed of Cu-Zn-Sn-S. In this procedure, no post annealing process was required. The optical band gap of the resulting CZTS thin film with a stannite structure was 1.45 eV. The heterojunction device consisted of CZTS and cadmium tin oxide shown photovoltaic effect of 165 mV open circuit voltage. Later on, Tanaka *et al.* [24] tried to deposited CZTS thin films using the hybrid sputtering technology. They first sequentially deposited Sn/Zn/Cu precursor layers and then these precursor layers were annealed under sulfur flux at different temperatures. They found that the formation of CZTS phase started at 350 °C. A direct band gap was found to be 1.5 eV and the absorption coefficient is over 10^4 cm^{-1} , indicating that CZTS is very promising in thin film solar cell application. The loss of Zn was also found in the CZTS sample when annealed at temperature above 450 °C.

Fernandes *et al.* [27] studied the influence of the metallic (Sn-Zn-Cu) stack order on the quality of the final CZTS thin films and found Zn/Sn/Cu (top) stack to give better quality films

compared to Sn/Zn/Cu (top) stack. Recently, Chalapathy *et al.* [28] fabricated CZTS thin films from a two-step sulfurization process with the DC magnetron sputtering of Cu/ZnSn/Cu stack as the first step while annealing of the precursor stack under sulfur atmosphere as the second step. They have investigated the annealing temperature effect on the final products and found that single phase CZTS can be obtained at temperature higher than 560 °C. Solar cells fabricated from the CZTS sample annealed at 560 °C shows the best efficiency of 4.59 %.

In 2007, Katagiri's group [25] reported conversion efficiencies of 5.74 % for CZTS-based solar cells. The CZTS absorbers were prepared by sulfurizing the precursor layers (at 580 °C for 3 h) deposited by a RF magnetron co-sputtering process of SnS, Cu and ZnS targets. In the following year, it was reported that soaking these films in deionized water prior to the deposition of CdS buffer layer helps to improve the solar cell performance to 6.7 % [18]. This improvement is due to the removing of metal oxide from the CZTS surface. Recently, 7.6 % efficiency has been reported by Fukano *et al.* [26], which is the most efficient CZTS-based solar cells from sputtering process. This result was achieved by optimizing the annealing time for the precursor layers. They found that 580 °C for 30 min under 20 % H₂S balanced with N₂ is the optimized annealing condition. In addition, they also found that CZTS thin films obtained from a three-layered (ZnS/Sn/Cu (top)) precursor shows better quality than that from a four-layered (ZnS/Sn/Cu/ ZnS (top)) precursor.

2.3.1.2 Evaporation

Evaporation techniques such as electron beam evaporation and co-evaporation have been widely used for deposition of CZTSSe thin films [5, 16, 29-36].

The first publication on evaporated CZTS thin films was in 1997 by Katagiri *et al.* [16] who sulfurized a stack of Zn/Sn/Cu (top) layers at 500 °C for 1-3 h under N₂ + H₂S (5 %) atmosphere. The precursor layers were deposited by electron beam evaporation with a substrate temperature at 150 °C. The device with a structure of glass/Mo/CZTS/CdS/ZnO/Al from the resulting CZTS thin films shows 0.66 % conversion efficiency. By replacing the layer of Zn with ZnS, varying the substrate temperatures from 200 °C for depositing ZnS and Sn to 400 °C for depositing Cu and changing the the annealing temperature to 550 °C, Katagiri *et al.* improved the conversion efficiencies to 2.62 % [5]. By adopting the similar deposition

approach but changing the stack order to Zn/Cu/Sn (top), Kobayashi *et al.* [37] further improved the solar cells efficiency to 4.53 %.

Instead of a sequential deposition of Zn-Sn-Cu precursors, Wang *et al.* [32] employed a thermal co-evaporation technique where Cu, Zn, Sn and S were deposited simultaneously onto a Mo coated soda lime glass substrate. The substrate was at 110 °C during the deposition process. A sequential annealing process at 540 °C for 5 min in sulfure atmosphere was applied. A 650 nm thick CZTS thin film based solar cells with a configuration of glass/Mo/CZTS/CdS/i-ZnO/ITO/ Ni–Al grids showed 6.8 % efficiency ($V_{OC} = 587$ mV, $J_{SC} = 17.8$ mA/cm², FF = 65 %). The limitation of the device performance was found to be due to the dominated surface recombination. Using the similar deposition techniques, Shin *et al.* [36] have fabricated CZTS-based solar cells showing 8.4 % efficiency ($V_{OC} = 665$ mV, $J_{SC} = 19.5$ mA/cm², FF = 66.8 %) which is the highest efficiency reported so far for pure sulfide CZTS-based photovoltaic devices. After the co-evaporation, a annealing process was also applied to the deposited CZTS thin films. But the annealing temperature was raised to 570 °C from 540 °C used in the process of Wang *et al.* [32].

Shin *et al.* [35] have also attempted to deposited CZTSe thin films by coevaporation techniques. They found that a TiN barrier layer was helpful in preventing the formation of MoSe₂ at the back contact and they demonstrated 8.9 % efficient CZTSe-based solar cells with a 20 nm TiN barrier layer between CZTSe and Mo substrate. Recently, Repins *et al.* reported 9.15 % efficient CZTSe-based devices from co-evaporated CZTSSe absorbers ($V_{OC} = 377$ mV, $J_{SC} = 37.4$ mA/cm², FF = 64.9 %) [31]. This is the best pure selenide CZTSe-based solar cells reported so far. It should be noted that 15 nm NaF was evaporated onto the Mo substrate prior the deposition of CZTSe although there was no solid evidence showing that NaF helped to improve the device performance.

2.3.1.3 Pulsed laser deposition

In 2007, Moriya *et al.* [6] reported on using pulsed laser deposition (PLD) to fabricate CZTS thin film based solar cells. In their preparation process, a KrF pulsed laser with a wavelength of 248 nm was use to ablate a sintered CZTS target. The substrate was kept at room temperature during deposition process. The deposited films were post annealed at 300 – 500 °C in N₂ atmosphere. Solar cells fabricated from the sample annealed at 500 °C showed

efficiencies of 1.74 %. CZTSe thin films has also been fabricated by using a pulsed Nd: YAG laser with a wavelength of 1064 nm to ablate the CZTSe target, as reported by Wibowo *et al.* [38]. In 2012, Moholkar *et al.* [39, 40] prepared CZTS thin films adopting an approach similar to Moriya *et al.*; but the sample was annealed 400 °C under N₂ + H₂S (5 %) atmosphere instead of pure N₂ atmosphere. By optimizing the chemical composition of the resulting CZTS thin films, they achieved efficiencies as high as 4.13 % with a high V_{OC} at 700 mV [40].

2.3.2 Non-vacuum solution-based techniques

Non-vacuum solution-based techniques have attracted great attention due to their potential for low-cost and high throughput deposition of thin films. Various solution-based techniques have been explored in depositing CZTSSe thin films as detailed below.

2.3.2.1 Precursor-ink based approach

Preparation of CZTSSe thin films directly from the precursors is highly attractive because the chemical composition of the resulting CZTSSe thin films can be easily controlled by tailoring the chemical composition of the precursors.

In 2007, Tanaka *et al.* [41] reported on the synthesis of CZTS thin films by a sol-gel approach. They used copper (II) acetate monohydrate, zinc (II) acetate dihydrate, and tin (II) chloride dihydrate as precursors, 2-methoxyethanol as solvent and monoethanolamine as stabilizer. CZTS thin films on glass substrates were formed by spin coating of the precursor ink followed by annealing in an N₂ + H₂S (5%) gas atmosphere for 1 h at 500 °C. The composition of the resulting CZTS thin films was near stoichiometry and the band gap was found to be 1.49 eV. By tuning the chemical composition of the CZTS thin films to Cu/(Zn + Sn) = 0.87 and Zn/Sn = 1.15, solar cells with 1.01 % conversion efficiencies were achieved by the same group [42]. By further optimizing the chemical composition of the CZTS thin films to Cu/(Zn + Sn) = 0.80 and Zn/Sn = 1.15, they fabricated 2.03 efficient solar cells [43]. In a recent publication reported by the same group, the influence of H₂S concentration on the properties of the CZTS thin films has been studied. They found that the CZTS thin films annealed in 3 % H₂S + N₂ showed the best crystal quality compared with those annealed in 5 %, 10 % and 20 %

H₂S + N₂ as demonstrated by the narrowest XRD peaks and largest grain size. Solar cells fabricated from the 3 % H₂S shows the best conversion efficiency at 2.23 %.

Ki *et al.* [44] from University of Washington have fabricated CZTSSe thin films by spin coating the ink precursors composed of Cu(CH₃COO)₂·H₂O, ZnCl₂, SnCl₂·2H₂O, thiourea and dimethyl sulfoxid. The CZTS precursor films were annealed at 580 °C for 2.5 min on a hot plate inside a glove box after each coating process. To reach desired thickness, seven coating processes were carried out. The obtained precursor films with desired thickness were annealed at 500 °C for 20 min in Se-containing atmosphere. The average metal stoichiometries of Cu/(Zn + Sn) and Zn/Sn were 0.80 and 1.13, respectively in the final films. Devices with a configuration of glass/Mo/CZTSSe/CdS/ZnO/ITO/Ni-Al showed efficiencies of 4.1 %.

Pure selenided CZTSe thin films were also fabricated by a similar approach reported by Fella *et al.* [45] In their preparation, copper (II) nitrate hemipentahydrate, zinc (II) nitrate hexahydrate and tin (IV) chloride hydrate were used as precursors which were dissolved in ethanol and 1,2-propanediol. Ethyl cellulose was used to adjust viscosity of the precursor inks. The precursor films were formed on a Mo coated glass substrate by knife coating. The resulting CZTSe thin films after annealing in Se-containing atmosphere at a temperature range of 370 to 660 °C for 26 min showed a double-layered structure with a large grain layer on top and a carbon-rich layer near the back contact. In spite of the double-layered structure, efficiencies of 4.28 % were obtained from such films.

In 2010, Todorov *et al.* [7] from IBM explored a new ink formulation approach using the hydrazine as solvent. In this approach, Cu₂S, SnSe, Se, S and Zn were used as precursors. Readily dispersible ZnSe(N₂H₄) particles were formed in situ when stoichiometric elemental zinc powder was added the SnSe-Se solution, which act as stress-relief and crack-deflection centers during the deposition of CZTSSe thin films. CZTSSe thin films with Cu/(Zn + Sn) = 0.8 and Zn/Sn = 1.2 were deposited on Mo coated soda lime glass substrates by spin coating the precursor inks followed by annealing on a hot plate at 540 °C. Solar cells fabricated from the resulting CZTSSe thin films and having a glass/Mo/CZTSSe/CdS/ ZnO/ITO/Ni-Al grid structure, showd conversion efficiencies as high as 9.66 % (V_{OC} = 516 mV, J_{SC} = 28.6 mA/cm², FF = 65 %). In 2012, 10.1 % efficient CZTSSe-based solar cells were reported by the same group [20, 21]. In these devices, an MgF₂ antireflection coating was used on top of the ITO layer to reduce the loss of the light. Devices analysis showed that the performance of

the devices was limited by the dominant interface recombination, short minority carrier lifetime, and high series resistance. Very recently, they have updated the efficiencies to 11.1 % which is the record efficiencies for CZTSSe-based solar cells based on all kinds of methods [4].

2.3.2.2 Spray pyrolysis

There are some efforts attempt to use to spray pyrolysis techniques to deposit CZTS thin films [46-52]. To our best knowledge, the earliest publication was from Nakayama *et al.* in 1996 [46]. The CZTS thin films were prepared by spraying a solution containing CuCl_2 , ZnCl_2 , SnCl_4 and thiourea dissolved in water and ethanol onto a glass substrate heated to 280-360 °C. Stoichiometric CZTS thin films were obtained by annealing the as-deposited thin films at 550 °C in Ar- H_2S atmosphere. Cu_2S phase was found in Cu-rich films while Cu_2SnS_3 phase was found in Zn-poor films. Kumar *et al.* [49, 50] studied the effect of the PH value of the starting solution and the copper salt and thiourea concentrations on the growth of CZTS thin films. They found that the PH = 3.0 starting solution gave a single phase CZTS [49] and the optimized concentrations for copper salt and thiourea were 0.01 M and 0.04 M, respectively [50].

Rajeshmon *et al.* [51] studied different tin precursors on the properties of CZTS thin films. They found that although both SnCl_4 and SnCl_2 precursors gave the kesterite type CZTS the crystal quality and grain size were better for SnCl_4 based films. They fabricated solar cells with a superstrate configuration (glass/ITO/CZTS/ In_2S_3 /Ag) from the SnCl_4 based CZTS thin films. They found that the efficiencies of the solar cells can be improved from 0.38 % to 1.5 % by doping the In_2S_3 buffer layer with Indium which reduce the series resistance of the solar cells [52].

2.3.2.3 Electrochemccal deposition

The electrodepostion of CZTSSe thin films can be summarized into two categories: sequential electroplating of precurosors, and single step elctrodeposition of precursors, followed by annealing under sulfur or selenium-containing atmosphere.

The first report on CZTS thin films using the sequential deposition approach was from Scragg *et al.* [53] who annealed a metal stack of Cu/Sn/Zn (top) deposited on a Mo coated glass substrate at 550 °C for 2 h in sulfur atmosphere. Secondary phase of SnS₂ was observed by the XRD measurement in the CZTS thin films. Devices fabricated from such films showed 0.8 % efficiencies. By optimizing the sequential stack to Cu/Sn/Cu/Zn (top) and annealing conditions, they improved the efficiencies to 3.2 % [54].

Ahmed *et al.* [55] developed a three-step method: i) sequentially electroplated Cu/Zn/Sn or Cu/Sn/Zn stacks; ii) annealing the stacks at low temperature (210-350 °C) under N₂ to produce homogeneous alloys; iii) annealing of these well-mixed CuZn and CuSn alloys at 550-590 °C in sulfur atmosphere for 5-15 min to allow the formation of CZTS. Secondary phases such as Cu₂S, SnS and Cu₂SnS₃ were found in the annealed samples when the annealing temperature lowers than 580 °C. They proposed that secondary phases of ZnS and Cu₂SnS₃ reacted to form CZTS when the annealing temperature was above 580 °C. Solar cells made from the CZTS samples prepared from sulfurization of CuZnSn precursors at 585 °C for 12 min showed efficiencies ranging from as high as 7.3 %. This is highest efficiencies for the pure CZTS-based solar cells prepared from electrodeposition to date. Recently, Guo *et al.* [8] using a similar deposition process, fabricated 7.0 % efficient CZTS and CZTSe based solar cells. After annealing of the Cu/Zn/Sn metal stacks at 360 °C in N₂ for 30 min, the samples sealed in a closing quartz tube together with sulfur or selenium were annealed at 535-585 °C for 5-20 min. The optimized salinization conditions were found to be at 585 °C for 7 min while the optimized sulfurization conditions were at 585 °C for 12 min. They proposed that the low shunt resistance in CZTSe-based solar cells (0.48 KΩcm²) in contrast to CZTS-based solar cells (11.8 KΩcm²) is due to the existence of a Se-poor and Sn-rich grain boundary region. They also proposed that the oxygen observed in the CZTS/CZTSe thin films may be responsible for the low J_{SC} in the corresponding devices.

Co-electrodeposition of Cu-Zn-Sn precursors for CZTS thin films was introduced for the first time by Ennaoui *et al.* [56]. They deposited Cu-Zn-Sn precursor layers on the Mo coated soda lime glass substrate from alkaline electrolyte bath containing Cu (II), Zn (II), and Sn (IV) metal salts in a single step. The precursor layers annealed 550 °C in Ar-H₂S (5 %) atmosphere for 2h to allow the reaction of the precursors to form CZTS. EDX mapping analysis revealed existence of an area with reduced Zn signal near the back contact, which may

point to Cu_2SnS_3 phase. Solar cells fabricated from CZTS films with $\text{Cu}/(\text{Zn} + \text{Sn}) = 0.97$ and $\text{Zn}/\text{Sn} = 1.08$ showed an efficiency of 3.4 %. Using a similar co-electrodeposition process, Araki *et al.* [57] reported 3.16 % efficient CZTS-based thin films solar cells. The sulfurization of the Cu-Zn-Sn precursor layers was performed at higher temperature (580 or 600 °C) compared to that reported by Ennaoui *et al.* (540 °C) [56] for the same time (2 h). Sample annealed at 600 °C gave the best solar cells.

2.3.2.4 Nanoparticle-based approach

In 2009, Steinhagen *et al.* [58] reported on the synthesis of CZTS nanoparticles by adopting a one-pot technique where all the precursors (Cu, Zn, Sn metal salts and elemental sulfur) and oleylamine were mixed together at room temperature and then heated to 280 °C to allowed the formation of CZTS nanoparticles. CZTS thin films were deposited by spraying of the CZTS nanoparticle dispersed in toluene onto the ITO coated glass substrates. Solar cells with a superstrate structure (ITO/ZnO/CdS/CZTS/Au) fabricated from the as-deposited CZTS sample showed efficiencies of 0.23 %. In the same year, Guo *et al.* [59] also reported on the synthesis of CZTS nanoparticles with a stoichiometry of $\text{Cu}_{2.12}\text{Zn}_{0.84}\text{Sn}_{1.06}\text{S}_4$ using a hot-injection approach where Cu, Zn, Sn metal salts and elemental sulfur were used as precursor while oleylamine was used as both solvent and surfactant. The CZTS thin films were deposited by drop casting of the CZTS nanoparticle dispersed in toluene onto a Mo coated soda lime glass substrate and sequentially annealed between 400 and 500 °C in Se-containing atmosphere for 20 min. The sample annealed at 500 °C gave the best solar cells with conversion efficiencies of 0.8 %. Later on, they optimized the chemical composition of the CZTS nanoparticles with a stoichiometry of $\text{Cu}_{1.31\pm 0.02}\text{Zn}_{0.91\pm 0.03}\text{Sn}_{0.95\pm 0.02}\text{S}_4$, and used doctor blade technique to deposition the CZTS thin films from the ink of CZTS nanoparticle dispersed in hexanethiol. After annealing at 500 °C for 20 min in selenium atmosphere CZTSSe thin films showed a double-layered structure with larger grains on top and a carbon-rich nanoparticle layer near the back Mo substrate. Solar cells using such films showed 7.2 % efficiencies which are the record efficiency for CZTSSe-based solar cells from nanoparticles based approach [9].

Tian *et al.* [60] reported on a synthesis of hydrophilic CZTS nanoparticles by a modified solvothermal method. They deposited CZTS thin films on a flexible Mo coated Al foil

substrate by a roll-to-roll printing technique using the CZTS nanoparticle inks dispersed in ethanol. The CZTS thin films were used for fabrication of solar cells after annealing at 500 °C for 20 min in sulfur atmosphere. It is noted that ZnS was used as buffer layer and an efficiency of 1.94 % was achieved.

Except for the deposition of CZTSSe thin films from the quaternary CZTS nanoparticle precursors, there are also some other nanoparticle precursors for synthesis of CZTSSe thin films. For instance, Woo *et al.* [61] deposited CZTS thin films by spin coating using the inks containing Cu₂S, Zn, Sn and S nanoparticles precursors in ethanol. The Cu₂S, Zn, Sn and S nanoparticles were prepared by ball milling of the commercial Cu₂S, Zn, Sn and S powders, respectively. The CZTS thin films were formed by annealing the precursor films at 400 to 530 °C for 30 min in N₂ + H₂S (5%) atmosphere. They found that single phase CZTS can be obtained when the sample annealed at 530 °C. Solar cells fabricated from this sample showed an efficiency of 5.14 %.

3 Colloidal synthesis of ZnS, SnS and Cu₃SnS₄ nanoparticles

As mentioned in Chapter 2, there are many ways for preparing CZTSSe thin films. One of the promising ways is using nanoparticles, CZTS(Se) or binary and ternary chalcogenides, as precursors followed by annealing under sulfur or selenium-containing conditions. The key step for this approach is to synthesize monodisperse nanoparticles which can be coated by suitable methods such as spin coating. Therefore, in this chapter we will focus on the synthesis of ZnS, SnS and Cu₃SnS₄ (CTS) nanoparticles which will be used as precursors for the preparation of Cu₂ZnSn(S,Se)₄ thin films. A brief introduction of nucleation and crystal growth in colloidal chemistry is firstly introduced followed by the experimental section of synthesis of ZnS, SnS and Cu₃SnS₄ nanoparticles. Then the nanoparticles were further characterized by X-ray diffraction, transmission electron microscopy, energy dispersive X-ray spectroscopy and UV-visible absorption spectroscopy. Finally, the growth kinetics of CTS nanoparticles is studied.

3.1 Basic of nanoparticle growth

A brief introduction to the synthesis of nanoparticles is given in this section. More details of synthetic methods and nucleation and growth theory of nanoparticle can be found in [62, 63].

3.1.1 General synthesis strategies

Generally, there are two main different approaches for preparation of nanoparticles, namely “top-down” approach and “bottom-up” approach. The top-down method involves breaking down of the bulk materials into nanoscale size particles or structures. As a physical method, the top-down approach such as lithographic, ball milling and laser ablation can prepare large quantity of nanoparticles with high purity. However, the synthesis of monodisperse nanoparticles with controllable size and shape is very difficult to achieve by the

top-down approach. The bottom-up approach is based on the chemical reaction in solution to build up the nanoparticles or nanostructures from atoms, ions or clusters, which can be used to synthesize nanoparticles with controlled size and shape by varying the reaction conditions such as reaction temperature, precursors concentration and a mixture of surfactants. Among the various bottom-up methods, hot-injection and heating-up methods are two of the most popular synthetic methods for preparation of monodisperse nanoparticles.

A typical process of the hot-injection method involves rapid injection of a stock solution containing reactive precursors into the hot solution containing surfactants. The hot-injection method was first reported in 1993 by Murray *et al.* who successfully synthesized high quality CdE (E = S, Se, Te) nanoparticles by injection of a cold tri-n-octylphosphine solution containing the organic reagents (dimethyl cadmium) and chalcogenide precursors into hot trioctylphosphine oxide solution [64]. After that, the hot-injection method has been extensively used to synthesize all kinds of semiconductor nanocrystals such as CdSe [64-67], ZnS [68], CuInS(Se)₂ [69, 70], Cu₂ZnSnS(Se)₄ [71, 72] and so on by adopting appropriate combinations of reactive precursors, capping agents and solvents.

Although the hot-injection method has been proven to be an effective approach for synthesis of high quality nanoparticles, these injection-based methods are not very suitable for large-scale industrial preparation due to the difficulty of large mass transfer in the process of the injection. Consequently, the heating-up method, also called “non-injection synthesis” or “one-pot synthesis” method has been developed. In the synthesis, all the reaction precursors, solvents and capping agents are mixed together in one pot at room temperature and heated to the reaction temperature at which the formation of nanoparticles takes place. One of the most noticeable characteristics of this method is that it can yield highly uniform nanoparticles. The effectiveness of this method on synthesis of high quality metal, metal oxide and chalcogenide nanoparticles has been demonstrated by many groups. For example, Yang *et al.* [73] has shown that CdSe and CdTe nanoparticles with a size distribution of less than 5% can be synthesized by heating-up method. Therefore, considering the scalable possibility we choose heat-up approach to synthesize ZnS, SnS and CTS nanoparticles which will be used as the precursors for CZTSSe thin films.

3.1.2 Nucleation and growth

In general, the formation of nanoparticles in colloidal routes involves two important processes, the nucleation from initially homogeneous solution followed by the growth of the nanoparticles. According to LaMer *et al.* [74], the precipitation of monodisperse colloids requires a ‘burst nucleation’ where lots of nuclei are generated at the same time and no additional nucleation occurs during the following growth of the existing nuclei.

The nucleation and growth of monodispersed colloidal nanoparticles can be explained by the LaMer diagram, as shown in Figure 3.1. Three stages are identified. Stage I involves rapid generation of monomer via decomposition or reaction of precursor compounds. No nucleation occurs during this stage even though the concentration exceeds the equilibrium concentration reaching the supersaturation level because the existence of an extremely high energy barrier needed to be overcome for spontaneous homogeneous nucleation. Stage II represents the nucleation stage. Nucleation commences when the degree of the supersaturation is high enough to overcome the energy barrier for nucleation, thus resulting in the formation of stable nuclei. At the beginning of this stage, the monomer concentration continues to rise since monomers are generated more rapidly than they are consumed by nucleation. However, eventually when the consumption rate of the monomers resulting from the nucleation and growth exceeds the generation rate of the monomers, the concentration of the monomers start to decrease until it reaches the level at which the net nucleation rate is zero. When $S < S_c$, the system enters the pure growth stage (stage III), where no further nucleation occurs and the existing particles grow by addition of the monomers remaining in the solution to the existing nuclei as long as the solution is in the supersaturated regime.

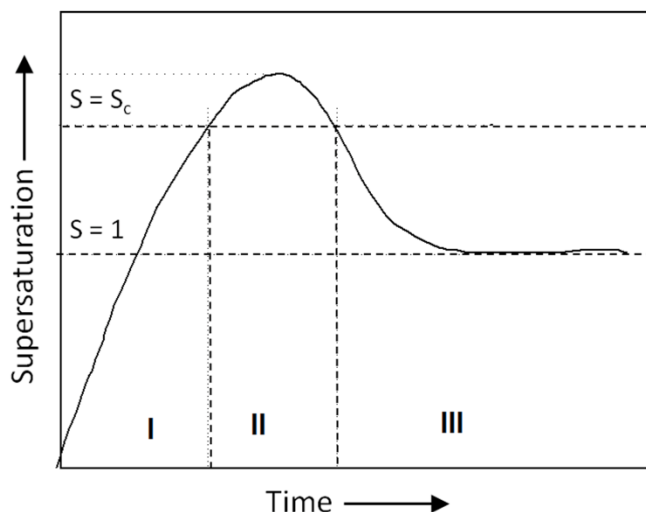


Figure 3.1 LaMer diagram [74] illustrating the stages in the formation of monodispersed colloidal nanoparticles. Stage I, Generation of monomers; Stage II, rapid nucleation occurs and this is followed by particle growth; Stage III, growth of nuclei.

The energy barrier for homogeneous nucleation is explained as follows [62]: the Gibbs free energy of formation of a spherical crystal $\Delta G(r)$ with a radius r from the solution with supersaturation S , is given by the equation:

$$\Delta G(r) = 4\pi r^2 \gamma + \frac{4}{3} \pi r^3 \Delta G_v \quad (3.1)$$

Where γ is the surface free energy per unit area and ΔG_v is the free energy per unit volume of a crystal.

$$\Delta G_v = -\frac{RT \ln S}{V_m} \quad (3.2)$$

Here, V_m is the molar volume of the monomer in crystal. ΔG_v is negative as long as the solution is supersaturated. Setting $\frac{d\Delta G(r)}{dr} = 0$ allows determining the critical radius r_c .

$$r_c = \frac{2\gamma V_m}{RT \ln S} \quad (3.3)$$

Figure 3.2 depicts relationship between the free energy and the radius of the nucleus. Only the nucleus with a radius larger than the r_c can grow spontaneously in the supersaturated solution while those with $r < r_c$ will be dissolved back to the solution as monomers.

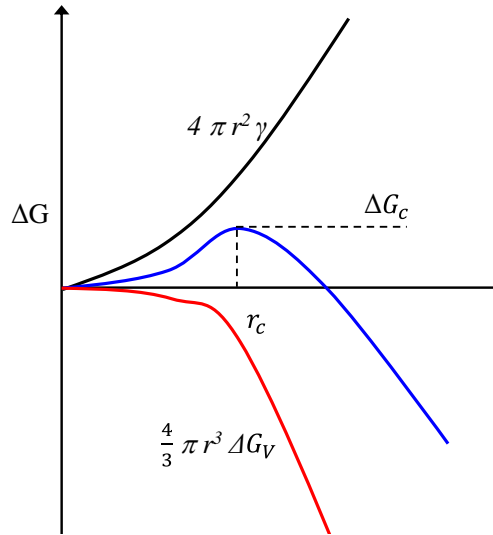


Figure 3.2 Plot of crystallization free energy vs. particles radius.

Growth is defined as the process of addition of monomers left in the solution onto the nucleus, resulting in a size increase and consumption of monomers. Figure 3.3 illustrates growth rates as a function of high (red) and low (blue) monomer concentrations. If the monomer concentration is high, there is a large difference between the chemical potential of the bulk solution and the diffusion sphere so diffusion to the nuclei surface is fast and growth is therefore fast [75]. Moreover, smaller crystallites with radius larger than r_c will grow faster than larger particles due to higher surface energy. As a result, the size focusing occurs, which leads to a narrow distribution [67]. As particles grow, the concentration of monomer decrease, which also alters the growth kinetics of the particles. Due to the low concentration of monomer, the chemical potential gradient between the bulk solution and the diffusion sphere is small, thus slowing down the growth rate of the crystal. When the monomer is depleted, Ostwald ripening process occurs. At this process, larger particles grow at the cost of the smaller particles, resulting in larger size distribution. For the synthesis of monodisperse nanoparticles, it is important to stop the growth before the growth enters the Ostwald ripening stage.

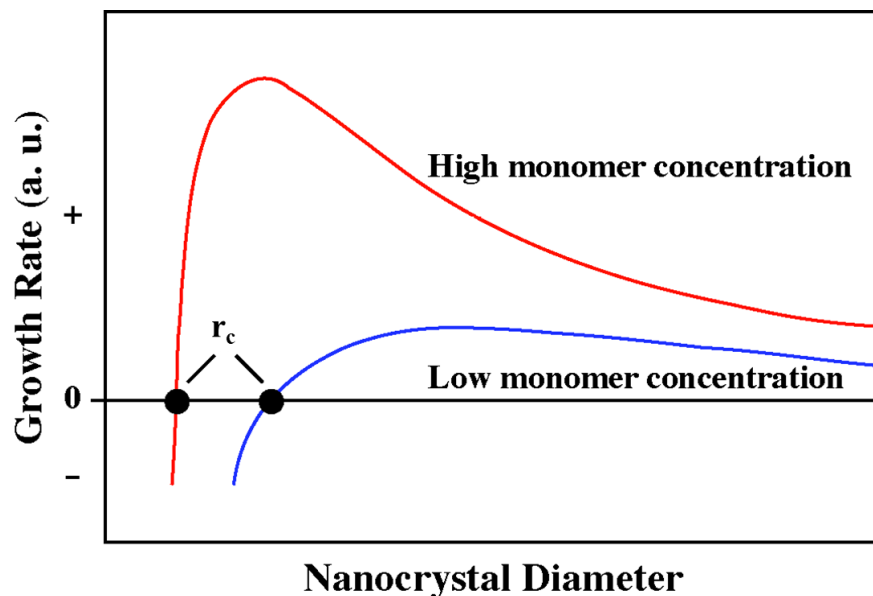


Figure 3.3 Growth rate as a function of crystal size at high (red trace) and low (blue trace) monomer concentrations [75, 76]. At high monomer concentrations, the critical radius is small, and smaller particles grow faster than larger particles, allowing for size focusing. With low monomer concentrations, the critical radius is larger than at high monomer concentrations.

3.2 Synthesis of nanoparticles

All the nanoparticles including ZnS, SnS and Cu₃SnS₄ were synthesized by heating-up process. Depending on the samples, oleylamine (OLA) or both OLA and 1-dodecanethiol (DDT) was used as solvent and capping agents. The precursors, organic solvent and capping agents were mixed in a three-neck round-bottom reaction flask in air. The flask was removed to a glove box which was filled with nitrogen to avoid the oxidation of the nanoparticles. The reaction mixtures were heated to 130 °C with an increasing rate of 10 °C/min and held at this temperature for 30 minutes. After that, the reaction mixtures were further heated to desired temperature depending on the sample prepared. The mixtures were kept at this temperature for certain time to allow the growth of the nanoparticles. The reaction temperature and time can be found in table 3.1. After cooling to room temperature, the nanoparticles were precipitated by addition excessive ethanol (for SnS and Cu₃SnS₄ nanoparticles) or acetone (for ZnS nanoparticles) to the flask and isolated by centrifuged at 6000 rpm for 10 minutes. The supernatant was discarded while the precipitate was dispersed in 4 ml toluene. The precipitation and isolation procedures were repeated one (for SnS and Cu₃SnS₄ nanoparticles)

or two more times (for ZnS nanoparticles) to remove excess organic surfactants. Finally, the nanoparticles were dispersed in toluene or 1-hexanthiol to form a stable ink.

Table 3.1 Detail synthetic conditions for different types of nanoparticles

Sample	Solvent and capping agents	Precursors	Reaction temperature (°C)	Reaction time (min)
ZnS	10 ml OLA	1.45 mmol zinc acetate dihydrate and 10 mmol sulfur	300	30
SnS-200	20 ml OLA and 2 ml DDT	2 mmol SnCl ₂ and 2 mmol sulphur	200	10
SnS-250	20 ml OLA and 2 ml DDT	2 mmol SnCl ₂ and 2 mmol sulphur	250	10
SnS-300	20 ml OLA and 2 ml DDT	2 mmol SnCl ₂ and 2 mmol sulphur	300	10
SnS-300-2	20 ml OLA and 2 ml DDT	2 mmol SnCl ₂ and 4 mmol sulphur	300	10
CTS-A	60 ml OLA	4 mmol copper acetylacetonate, 2 mmol SnCl ₂ and 6 mmol sulphur	250	0 - 400
CTS-B	30 ml OLA	2 mmol copper acetylacetonate, 1 mmol SnCl ₂ and 3 mmol sulphur	250	60
CTS-C	30 ml OLA	3 mmol copper acetylacetonate, 1 mmol SnCl ₂ and 4 mmol sulfur	250	60

X-ray diffraction (XRD) was used to characterize the structural properties of the nanoparticles. The samples were prepared by drop-casting of the nanoparticle inks onto the glass substrate and dry in air. The measurements operated on a Bruker D8-Advance X-ray diffractometer with Cu K α 1 radiation ($\lambda=1.5406 \text{ \AA}$) using a step size of 0.02° and step time of 0.3 second. Transmission electron microscopy (TEM) was used to analysis the morphology of the nanoparticle samples. TEM samples were prepared by dropping diluted nanoparticles solution onto a carbon film coated gold or copper grids and a Philips CM12 transmission electron microscopy with 120 KV acceleration voltage was used to acquire TEM images of the nanoparticles. Energy dispersive X-ray (EDX) spectroscopy measurement was also performed to the chemical composition of the samples during the TEM measurement. Optical properties

of the as-prepared nanoparticles dispersed in toluene were characterized by UV-visible absorption spectroscopy recorded on a Lambda 950 UV-Vis spectrometer.

3.3 Results and discussions

This section is to analyze the structure, morphology properties of the synthesized nanoparticles. The influence of the preparation conditions on the structure and morphology of the resulting nanoparticles will also be discussed.

3.3.1 ZnS nanoparticles

The morphology of the ZnS nanoparticles was studied by TEM measurements, as shown in Figure 3.4. Figure 3.4 (a) shows that the nanoparticles are monodispersed without agglomeration and shaped in sphere. The corresponding size distribution histogram (Figure 3.4 (b)) shows that the nanoparticles have an average size of 4.8 nm with a standard deviation of 1.0 nm. Figure 3.4 (c) is the high resolution TEM image of the nanoparticles, which shows clear lattice fringes throughout the whole nanoparticles, indicating the highly crystal quality of the nanoparticles. The distance between the lattice fringes was measured to be 0.31 nm which is consistent with the interplanar distance of the (111) plane of the zinc blende structure of ZnS. The stoichiometry of the ZnS nanoparticles was analyzed by EDX during the TEM measurements, as shown in Figure 3.4 (d). Both Zn and S elements were detected in the EDX spectrum with a ratio of Zn: S=53.8: 46.2, suggesting that ZnS nanoparticles are sulfur poor.

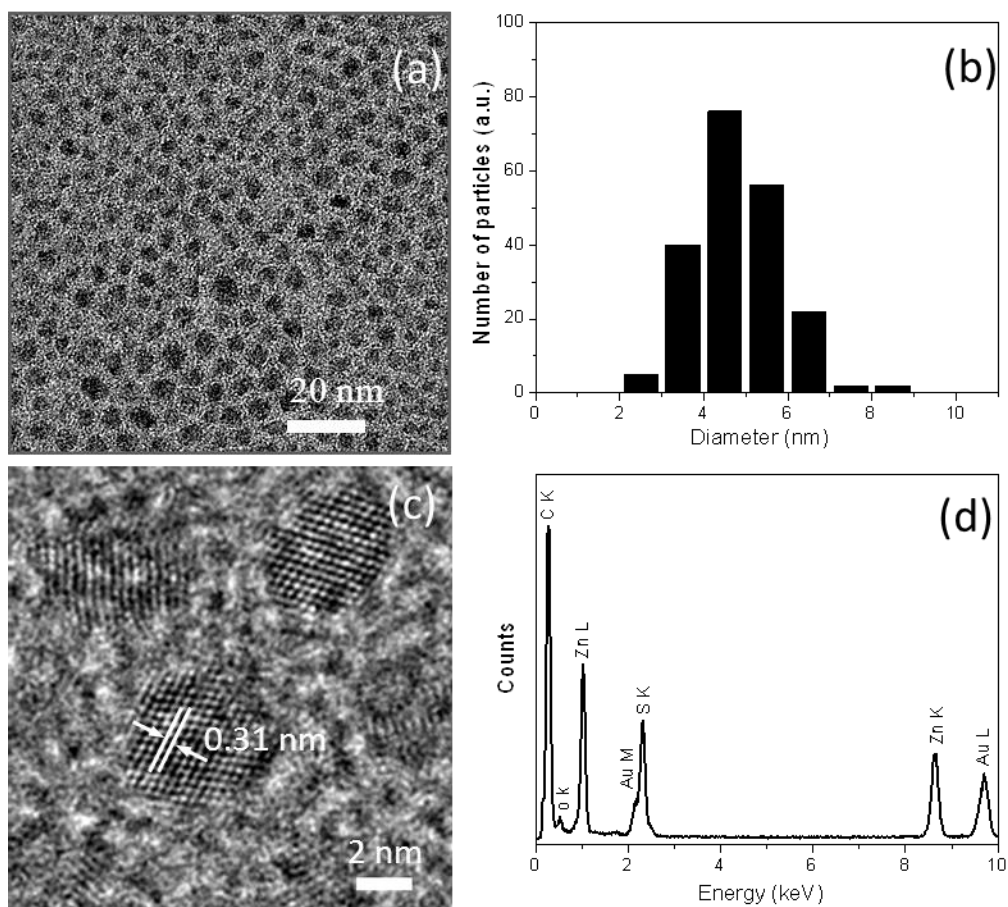


Figure 3.4 (a) TEM images of ZnS Nanoparticles on a carbon film coated Au grids, (b) the corresponding size distribution histogram, (c) HRTEM image of ZnS nanoparticles and (d) EDX spectrum.

To further confirm the structural properties of the Nanoparticles, XRD measurement was performed. Figure 3.5 shows that the all the diffraction peaks can be attributed to cubic ZnS. The broadening of the Bragg peaks is due to the small size of the nanoparticles. The average crystal size of the ZnS nanoparticles was estimated to be 2.6 nm by using Scherrer equation:

$$D = \frac{K\lambda}{\beta \cos\theta} \quad (3.4)$$

where D is the average crystalline size, K is the shape factor, λ is the X-ray wavelength, β is the line broadening at half the maximum intensity (FWHM) in radians, and θ is the Bragg angle. This value is smaller than the particle size of 4.8 ± 1.0 nm determined by TEM measurement.

One of main reasons for this could be due to the over estimation of the FWHM because there are many factors contribute to the broadening of the diffraction peaks such as instrumental factor, crystalline size, strain, and so on. Meanwhile, it should be pointed out that the size estimated by Scherrer equation represents the crystalline size rather than the particle size, thus it is reasonable that the crystalline size is smaller or equal to the particle size. Nevertheless, for more precise estimation, the other factors should be taken into account.

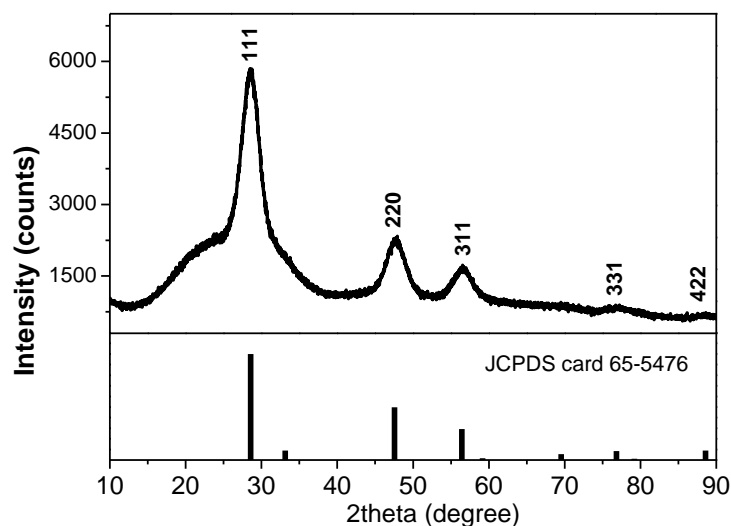


Figure 3.5 XRD patterns of the as-synthesized ZnS nanoparticles. For reference, the XRD pattern of ZnS from the standard international crystal diffraction database is shown below.

Figure 3.6 shows the absorption spectrum of the ZnS nanoparticles dispersed in toluene. The optical band gap energy was estimated to be 3.8 eV by extrapolating the linear region of the plot of $(\alpha h\nu)^2$ versus photon energy ($h\nu$) and taking the intercept on the $h\nu$ -axis. This value is slightly larger than the reported value of 3.6 eV which may be owing to the quantum confinement effect of the ZnS nanoparticles. It is well known that the optical band gap of the nanoparticles can be tuned by controlled the size of the nanoparticles due to the quantum confinement effect. The Bohr radius of ZnS reported is around 5 nm [77]. Thus, the increase of the band gap should be due to the quantum confinement of those particles with size smaller than 5 nm.

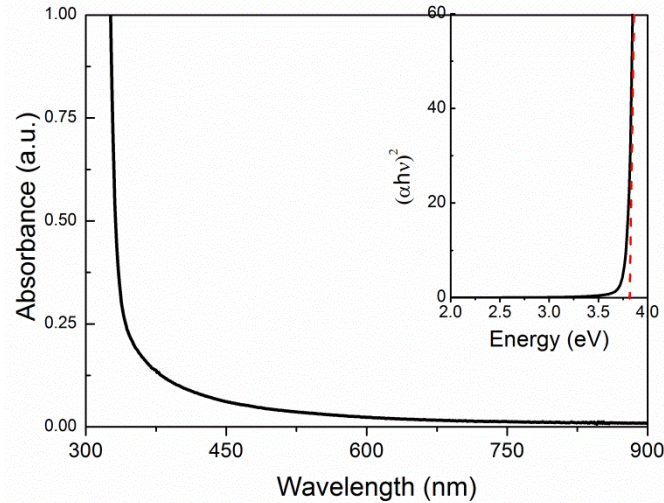


Figure 3.6 UV-Vis absorption spectrum of ZnS nanoparticles dispersed in toluene. Inset is the plot of $(\alpha h\nu)^2$ versus $h\nu$ (eV) for the nanoparticles.

3.3.2 SnS nanoparticles

The XRD pattern of the SnS-250 nanoparticles illustrated in Figure 3.7 clearly shows that nearly all diffraction peaks can be assigned to the orthorhombic structure SnS except the peak located at around $2\theta = 34^\circ$. This peak is corresponding to the (101) reflection of orthorhombic structure SnO (JCPDS 24-1342). The relationship between the spacing distance and lattice parameters is followed equation (3.5). Hence, we calculated the lattice parameters from the XRD pattern by choosing three of the lattice planes using the equation 3.5. The obtained values of $a = 11.192 \text{ \AA}$, $b = 3.985 \text{ \AA}$ and $c = 4.323 \text{ \AA}$ are in good agreement with the standard JPCDS card 73-1859 for orthorhombic structure SnS where $a = 11.18 \text{ \AA}$, $b = 3.982 \text{ \AA}$ and $c = 4.329 \text{ \AA}$.

$$d_{hkl} = \frac{1}{\sqrt{\frac{h^2}{a^2} + \frac{k^2}{b^2} + \frac{l^2}{c^2}}} \quad (3.5)$$

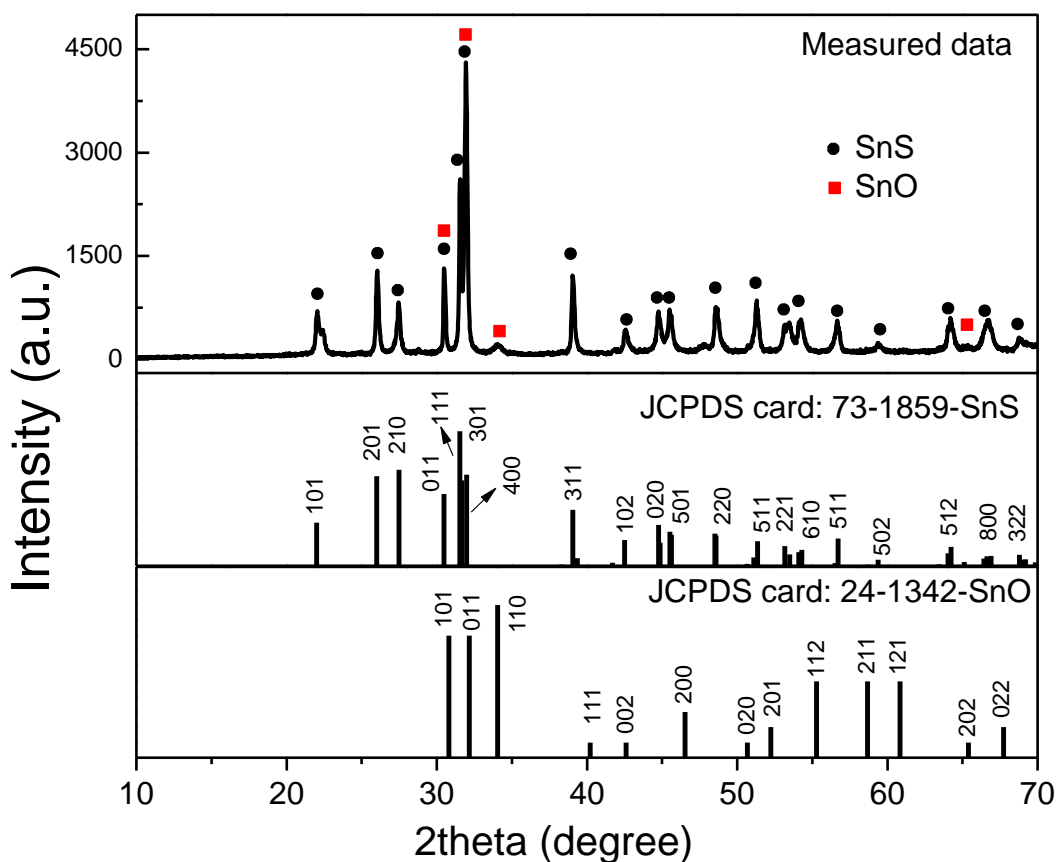


Figure 3.7 XRD patterns of as-synthesized SnS-250 nanoparticles. As references, the XRD patterns of SnS (JCPDS 73-1859) and SnO (JCPDS 24-1342) from the standard international crystal diffraction database are shown below.

Figure 3.8 shows a typical TEM image of the as-prepared sample. The shape of the nanoparticles is irregular varied from nanorods to nanosheets. HRTEM image (Figure 3.8(b)) shows clear lattice fringes revealing high crystal quality of the nanoparticles. The interplanar spacing was measured to be 0.285 nm which is in good accordance with the distance of (111) lattice planes of SnS. We have performed EDX analysis on the nanoparticles during the TEM measurements, which reveal that the nanoparticles are highly sulfur rich with an Sn: S ratio of 34.7: 65.3. The high ratio of sulfur can be attributed to the fact that the nanoparticles are capped by the 1-dodecanthiol surfactant which contains sulfur.

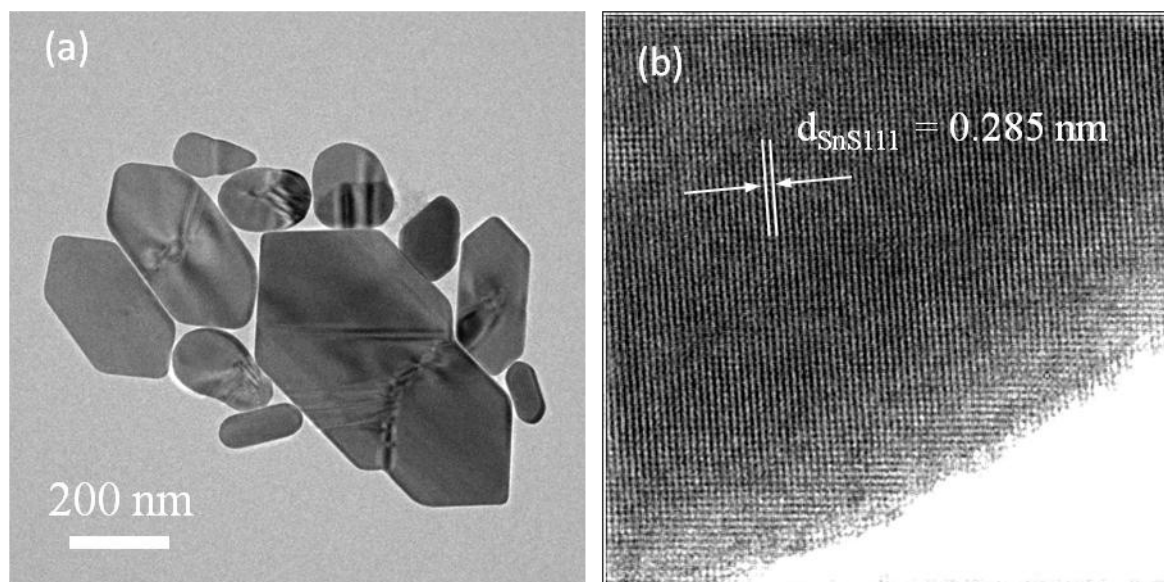


Figure 3.8 (a) TEM images of SnS-250 nanoparticles on a carbon film coated Cu grid, (b) HRTEM image of part of a SnS nanoparticle.

Influence of reaction temperature

To study the influence of the reaction temperature on the structure and morphology of the resulting nanoparticles, we have conducted two contrast experiments (sample SnS-200 and sample SnS-300) by changing the reaction temperature to 200 and 300 °C, respectively but maintaining the other conditions. The XRD pattern of the sample SnS-200 (Figure 3.9 (a)) reveals that the sample contains three different compounds, namely orthorhombic structure SnS and SnO and tetragonal structure SnO₂. When the reaction temperature was increased to 300 °C, the XRD pattern of sample SnS-300 changed as well. The most apparent changes were that a diffraction peak at $2\theta = 15^\circ$ corresponding to (001) planes of hexagonal structure SnS₂ was observed and the diffraction peaks corresponding to SnO₂ phase disappeared. Moreover, the sample SnS-300 shows better crystal quality than the sample SnS-200, as illustrated by difference of the intensity of the diffraction peaks displayed in Figure 3.9. Although there is not quantitative analysis on the phase's composition of these three samples prepared at different reaction temperatures, we can conclude that the sample prepared at 250 °C contains much purer SnS phase than those prepared at 200 °C and 300 °C. This is because the intensity of diffraction peaks arising from SnO phase is very low in SnS-250 compared to those in SnS-200, SnS-300 and SnS-300-2 (Figure 3.7).

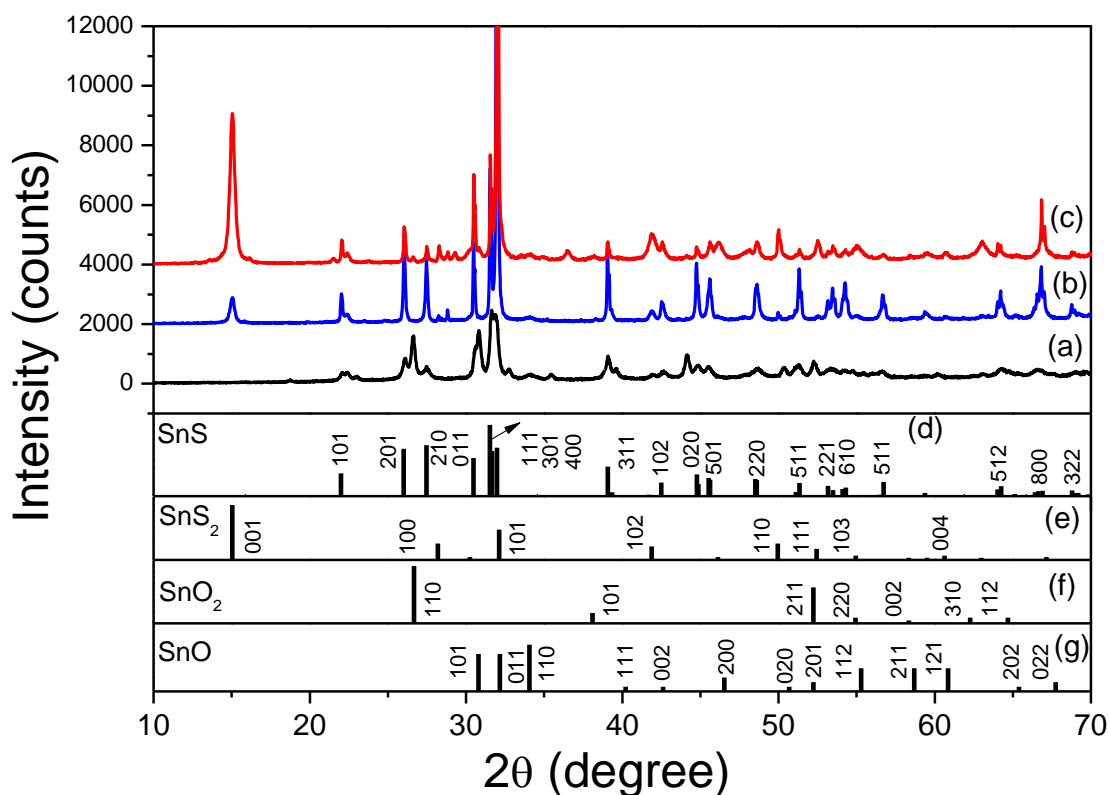


Figure 3.9 XRD patterns of samples from the contrast experiments: (a) SnS-200; (b) SnS-300 °C, (c) SnS-300-2. The difference between sample SnS-300 and SnS-300-2 is that higher sulfur precursor concentration was used. As references, the XRD patterns of SnS (JCPDS 73-1859), SnS₂ (JCPDS 23-0677), SnO₂ (JCPDS 01-0657) and SnO (JCPDS 24-1342) from the standard international crystal diffraction database are shown below.

Figure 3.10 shows the both low and high resolution TEM of samples S-200, SnS-300 and SnS-300-2. Sample SnS-200 is consisted of both smaller nanoparticles with irregular shape and nanosheets as revealed by Figure 3.10 (a). A HRTEM image from part of a nanosheet (Figure 3.10 (b)) shows a clear lattice fringe with interplanar spacing of 0.283 and 0.293 nm corresponding to the (111) and (011) planes of SnS. Sample SnS-300 is shaped in hexagonal plate and rectangular sheet showing a highly polydispersed size distribution (Figure 3.10 (c)). The HRTEM image (Figure 3.10 (d)) of part of nanosheet shows the nanoparticles are well crystallized as revealed by the clear lattice fringes with interplanar distances of about 0.313

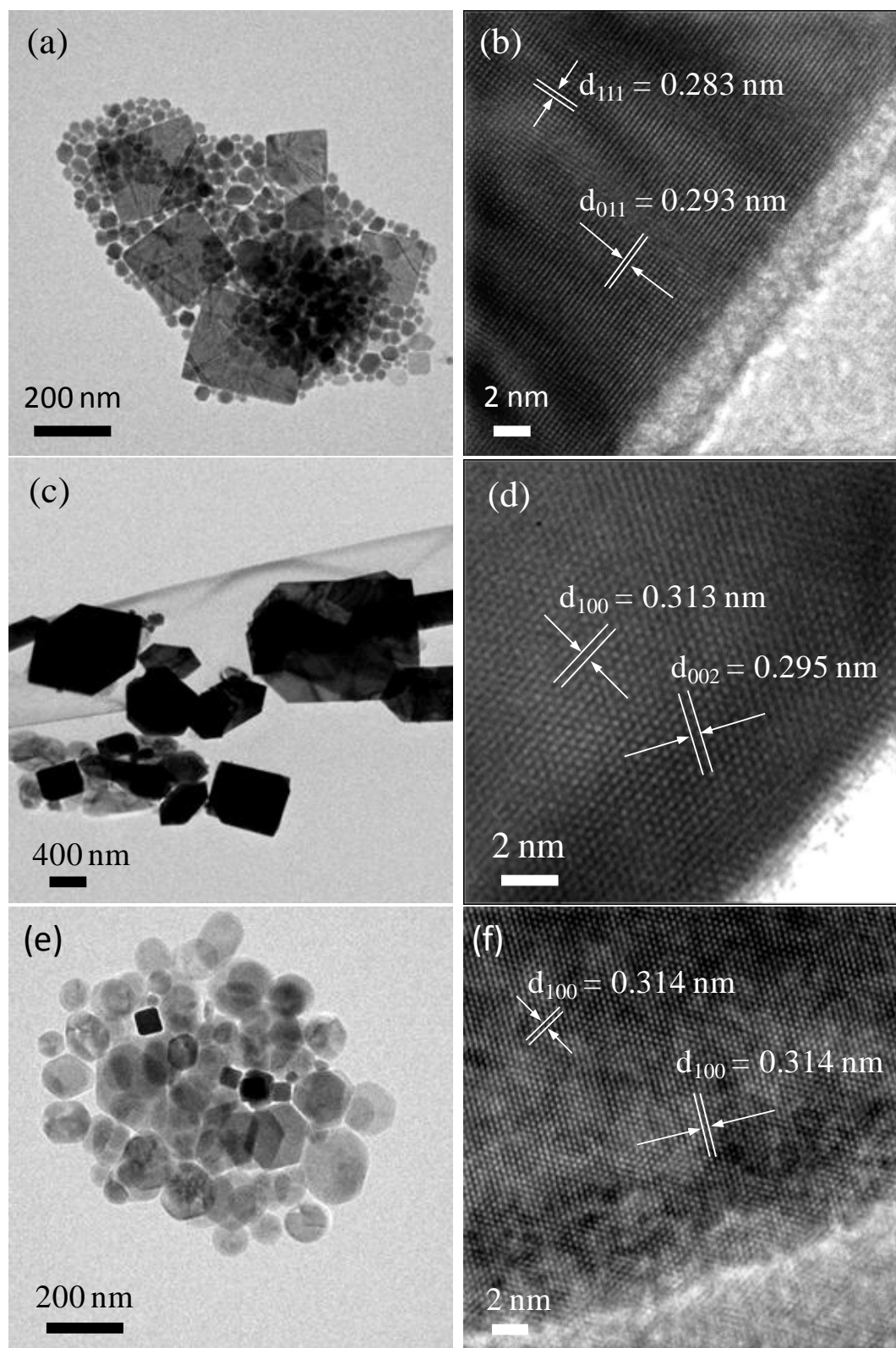


Figure 3.10 TEM and HRTEM images of samples from the contrast experiments: (a) and (b): SnS-200; (c) and (d) SnS-300; (e) and (f) SnS-300-2.

and 0.295 nm which are the characteristic fringe spacing of hexagonal SnS₂ phase in the (100) and (002) planes, respectively.

Hence, here we can draw the conclusion that the reaction temperature has great impact not only on the shape and size of the samples but also the phase content of the final products and 250 °C is a more preferable reaction temperature for the formation of SnS particles in our reaction systems.

Besides the reaction temperature, we have also examined the effect of the precursor's ratio on the final products. We found that when SnCl₂: S = 1: 1 changes to SnCl₂: S = 2: 5, the relative intensity of diffraction peaks corresponding to the SnS₂ phase increased dramatically (Figure 3.9 (c)), suggesting the increase concentration of SnS₂ phase in the obtained sample. The explanation for the increasing concentration of SnS₂ phase is that the larger amount of sulfur in the reaction solution can act as the oxidation reagent for Sn²⁺ to Sn⁴⁺. Furthermore, the sample exhibits more homogeneity in terms of shape (with most of the particles shape in hexagonal) although the size of the particles is still polydisperse.

3.3.3 Cu₃SnS₄ nanoparticles

The characterization and the growth mechanism of CTS nanoparticles will be presented in this section. The results of section 3.3.3.1 have been published in [78].

3.3.3.1 Characterization of Cu₃SnS₄ nanoparticles

X-ray diffraction as a powerful tool for characterization of crystal structures was used to determine the crystal structure of the obtained nanoparticles, as shown in Figure 3.11. When comparing the experimental result with the standard patterns of kuramite CTS (JCPDS card 33-0501), we found that all the diffraction peaks match quite well with kuramite CTS no additional peaks corresponding to Cu_xS or SnS_x, indicating that the as-synthesized nanoparticles are CTS with a tetragonal structure. Note that the most pronounced diffraction peak of the experimental diffraction pattern is (112), which is different from that of the standard JCPDS card 33-0501 where the most intensive peak is (220). This difference may suggests that the as-synthesized CTS nanoparticles exhibit preferential orientation along (112).

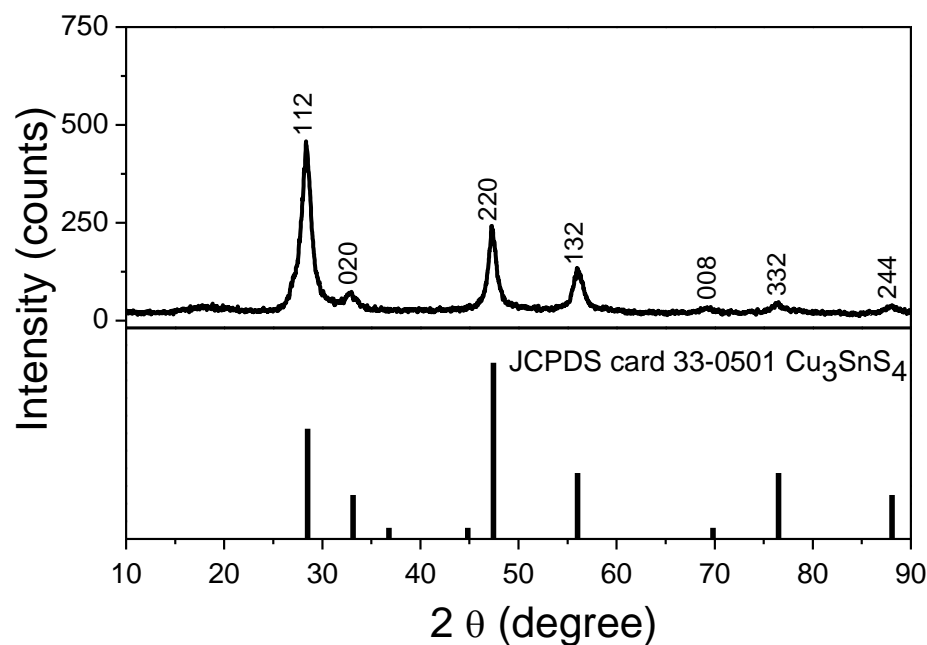


Figure 3.11 XRD pattern of as-synthesized CTS-B nanoparticles. For the reference, the standard XRD patterns of kuramite Cu₃SnS₄ was shown below.

Figure 3.12(a) shows a representative HRTEM image of a single CTS nanoparticles, which displays clear lattice fringes throughout the whole particle indicating the high crystal quality of the nanoparticles. The spacing of the lattice fringes was measured to be 0.312 nm, which matches the (112) plane of CTS. This result implies that the preferred orientation of CTS nanoparticles is (112), which is in accordance with the XRD result. Figure 3.12(d) shows a typical EDX spectrum of the nanoparticle samples. All elements, Cu, Sn, and S, were detected in the nanoparticles. Moreover, quantitative analysis reveals the average ratio of Cu: Sn: S is 42.9: 11.9: 45.2 as determined by analysing five randomly selected areas. This value is close to the stoichiometry of Cu₃SnS₄ with slightly copper rich and sulfur poor.

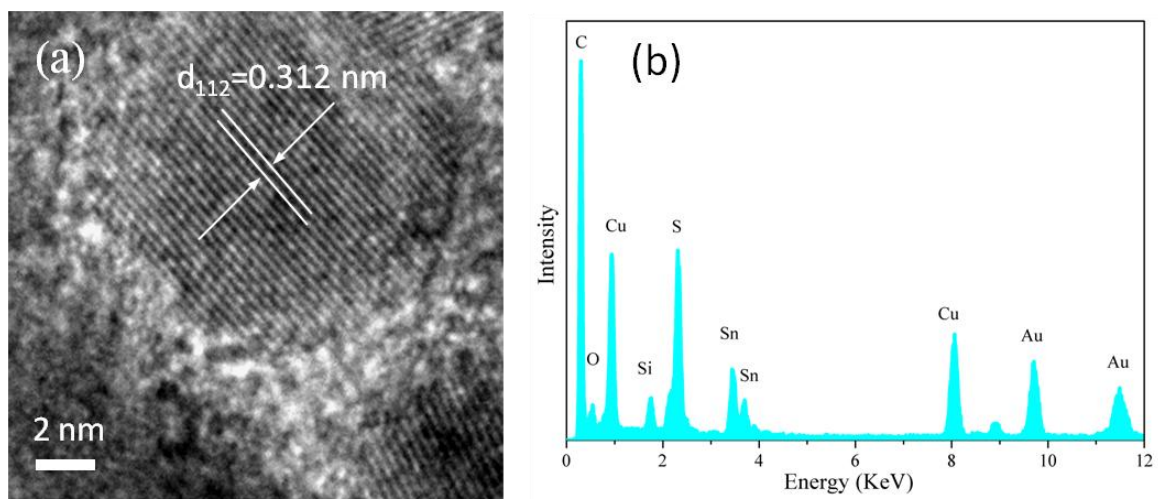


Figure 3.12 (a) High resolution TEM image of a single CTS-B nanoparticle; (b) EDX spectrum of CTS-B nanoparticles.

UV-vis absorption spectroscopy was used to evaluate the optical properties of the nanoparticles. Fig. 14 shows that the nanoparticles exhibit high absorption in the visible region. The optical band gap is 1.43 eV as estimated by extrapolating the linear part of the plot $(\alpha h\nu)^2$, the square of the absorption coefficient (α) multiplied by the photon energy ($h\nu$), versus $h\nu$. This value is consistent with the literature values of 1.2-1.6 eV [79-81].

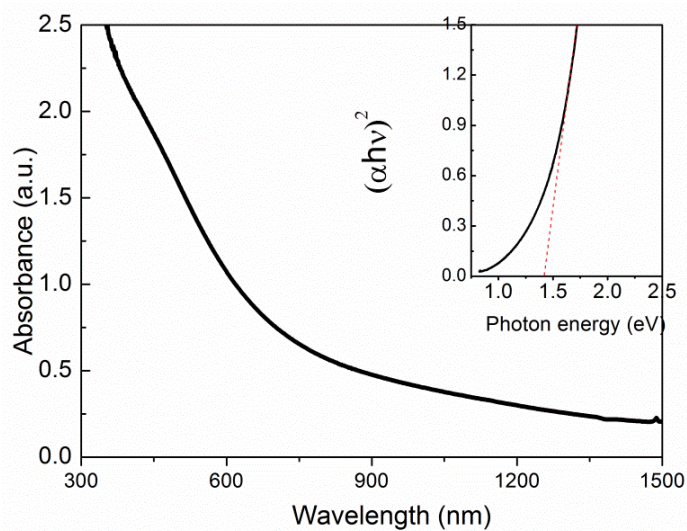


Figure 3.14 UV-vis-NIR absorption spectrum of CTS-B nanoparticles dispersed in toluene. Inset is the plot of $(\alpha h\nu)^2$ versus $h\nu$ (eV) for the nanoparticles.

3.3.3.2 Statistic analysis of Cu_3SnS_4 growth

It is very important to understand the growth kinetic of the nanoparticles growth because it will ensure greater control over the size and shape of nanoparticles. To study the growth kinetics of CTS nanoparticles, aliquots were taken throughout the course of the reaction and the TEM images were statistically analyzed, thus creating a quantitative view of

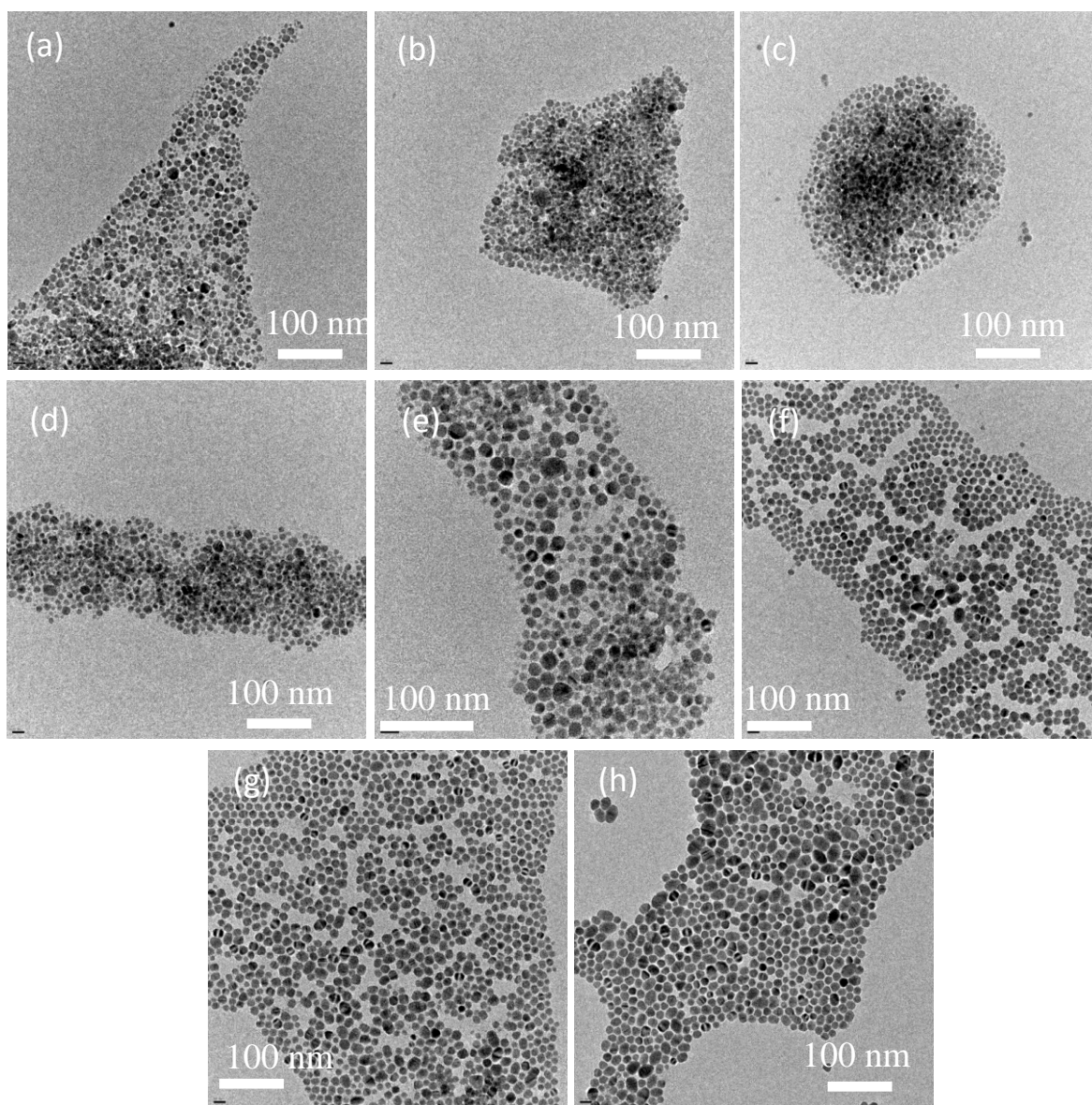


Figure 3.14. Representative TEM micrographs demonstrating the temporal evolution of the size distribution of CTS nanoparticles taken from the reaction mixture. Samples were taken at 250 °C at different reaction time: (a) 0, (b) 1, (c) 2, (d) 3, (e) 4, (f) 120, (g) 240, (h) 400 min.

CTS nanoparticles growth. Representative TEM images of samples extracted at different reaction time are shown in Figure 3.14.

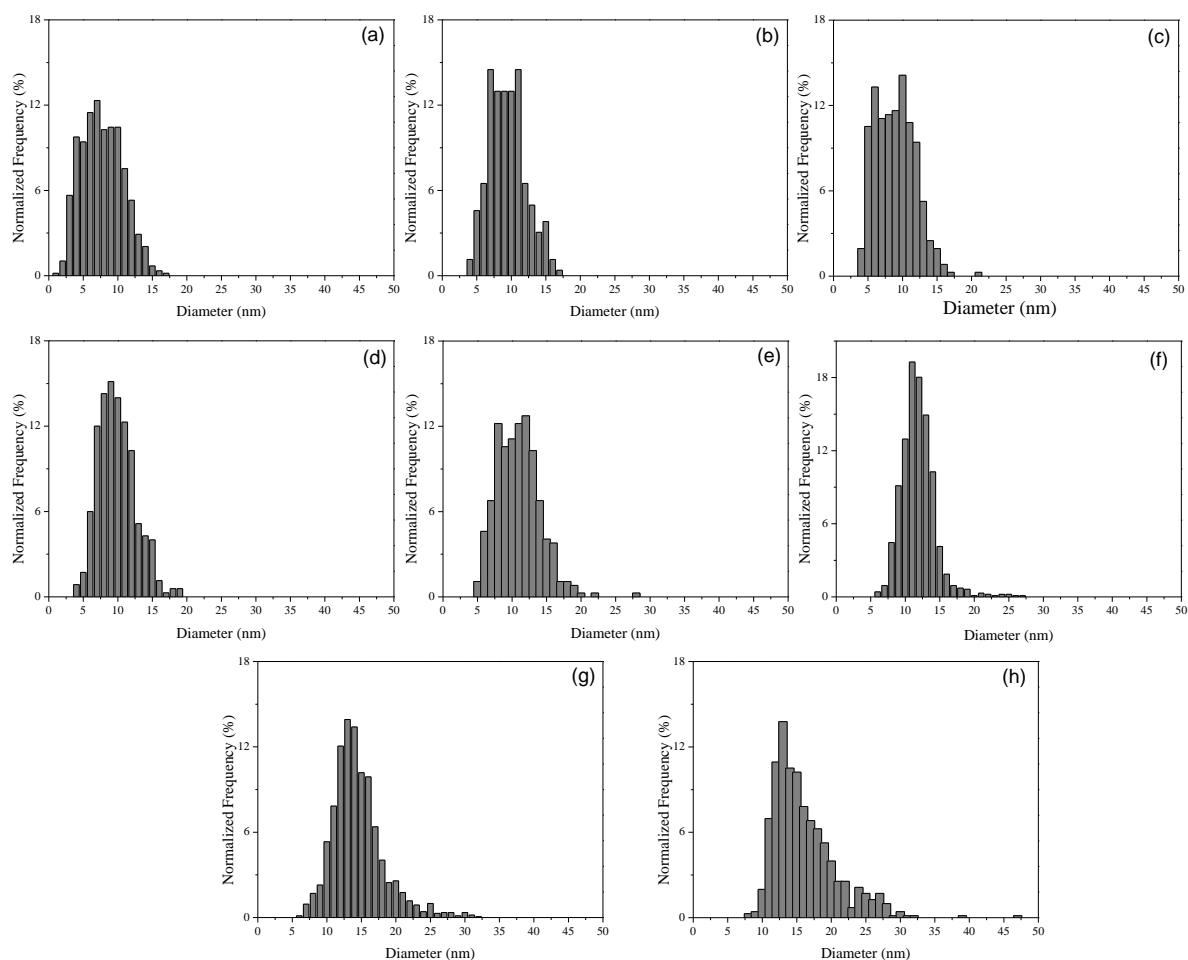


Figure 3.15. Evolution of size distribution histograms of CTS nanoparticles as determined by TEM. Each histogram represents the relative population of nanoparticles at the different reaction time and corresponds to the images shown in Figure 3.10; (a) 0, (b) 1, (c) 2, (d) 3, (e) 4, (f) 120, (g) 240, (h) 400 min.

As can be seen from the Figure 3.15 (a), nanoparticles with small size of 2-3 nm as well as large size of 15-17 nm can be observed when the reaction temperature reached 250 °C, indicating that 250 °C is high enough to provide enough energy to overcome the homogeneous nucleation energy barrier. Growth is sustained during the initial stage, eventually resulting nanoparticles that exhibit uniform size and shape after $t = 120$ min (Figure 3.15 (f)). The narrow, near Gaussian population distribution shown in Figure 3.15 (f) in the size distribution histogram suggests that the nanoparticles obtained at this stage are

monodisperse. After 120 min have passed, the nanoparticles continue to grow in solution, resulting in increasing population of nanoparticles in the larger size area after 400 min (Figure 3.15 (h)).

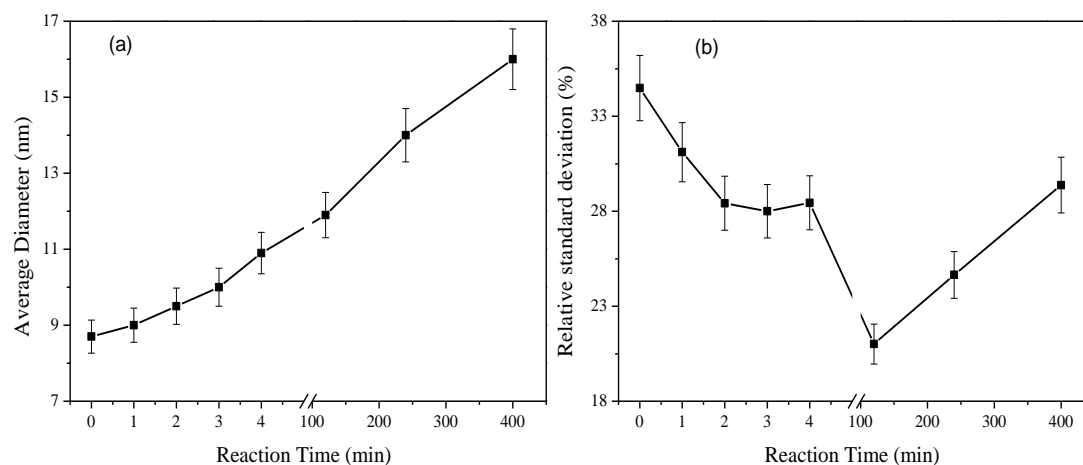


Figure 3.16 Statistical analysis of the evolution of CTS nanoparticles associated with Figure 3.15 and 3.15.(a) average diameter and (b) relative standard deviation. Note: the solid trend lines were added to guide the eyes. The average size of the nanoparticles increases quickly (52.5×10^{-2} nm/min) at the initial 4 minutes followed by slows increasing (1.46×10^{-2} nm/min).

Figure 3.16 shows more statistical analysis of the nanoparticle growth, including the evolution of the average size and the relative size distribution. As shown in Figure 3.12 (a), there are clearly two separate growth regimes. At the initial four minutes, the nanoparticles grow quickly from 8.7 nm to 10.9 nm with an average rate of 52.5×10^{-2} nm/min, and then slow down to 1.46×10^{-2} nm/min after 120 min aging time. This variation is in accordance with the size distribution histograms shown in Figure 3.11 where the histograms narrow down during this time span, but then broaden throughout the course of the reaction. Figure 3.16 (b) illustrates the evolution of the relative standard deviation of the nanoparticle growth. When the temperature first reached 250 °C, the sample shows a largest relative standard deviation of 34.5 % which decreases quickly until it reaches a minimum value of 21 % after 120 min reaction. After experiencing the decrease period, this value starts to increase gradually as the aging time increases.

3.3.3.3 Growth mechanism of Cu_3SnS_4 nanoparticles

Figure 3.17 explains the growth mechanism of CTS nanoparticles. When all the precursors were mixed together with oleylamine which serves as both solvent and capping agent and were heated to 130 °C, the metal-oleylamine complexes formed [82]. As the temperature was further increased, the molecular precursors start to decompose or react and subsequently create monomers. The nucleation did not start until the supersaturation of the monomer concentration reaches certain level where the energy barrier for the homogeneous nucleation can be overcome. According to LaMert diagram (Figure 3.1), when the monomer concentration reaches its maximum value, the nanoparticles start to grow. The nanoparticles are large enough to be observed when the temperature reached 250 °C, indicating that 250 °C is high enough to provide enough energy to overcome the energy barrier for homogeneous nucleation. The nanoparticles experienced a rapid growth during the initial four minutes, which featured by the increase of the average size of the nanoparticles from 8.7 nm to 10.9 nm but the size distribution narrowed down from 34.8 % to 28.4 %. As the increase of aging time, the concentration of monomers decreases while the growth of nanoparticles continues by adding monomers to the nanoparticles. The smaller particles grow faster than the larger ones due to the higher surface energy. As a result, the size distribution of the nanoparticles was narrowed down. In our case, we observed when the aging time was increased to 120 min, the nanoparticles shows the narrowest size distribution. These observations are the hallmark of the size-focusing growth mechanism where rapid growth and narrowing size distribution occurs simultaneously to create a monodisperse population of nanoparticles. This mechanism was first reported by Peng *et al.* [83] who observed that the average size of the CdSe nanodots increased rapidly (from 2.1 to 3.3 nm) and the size distribution was “focused” from 20 % to 7.7 % during the first 22 min aging time.

Following the initial size focusing period, due to the depletion of the monomer concentration, the dynamic critical size became larger than the average size of the nanoparticles. Under such condition, some nanoparticles with size smaller than the critical size dissolved into the solution as monomers and finally disappeared while the larger ones kept growing, leading to broader size distribution, as revealed by Figure 3.16. These variances suggest that the nanocrystals grow by Ostwald ripening mechanism in this stage.

Actually, the Ostwald ripening mechanism is the most common mechanism reported for nanoparticles growth [67, 84-87].

In short, the growth of the nanoparticles firstly followed the focusing of size distribution mechanism and then followed the classical Ostwald ripening mechanism.

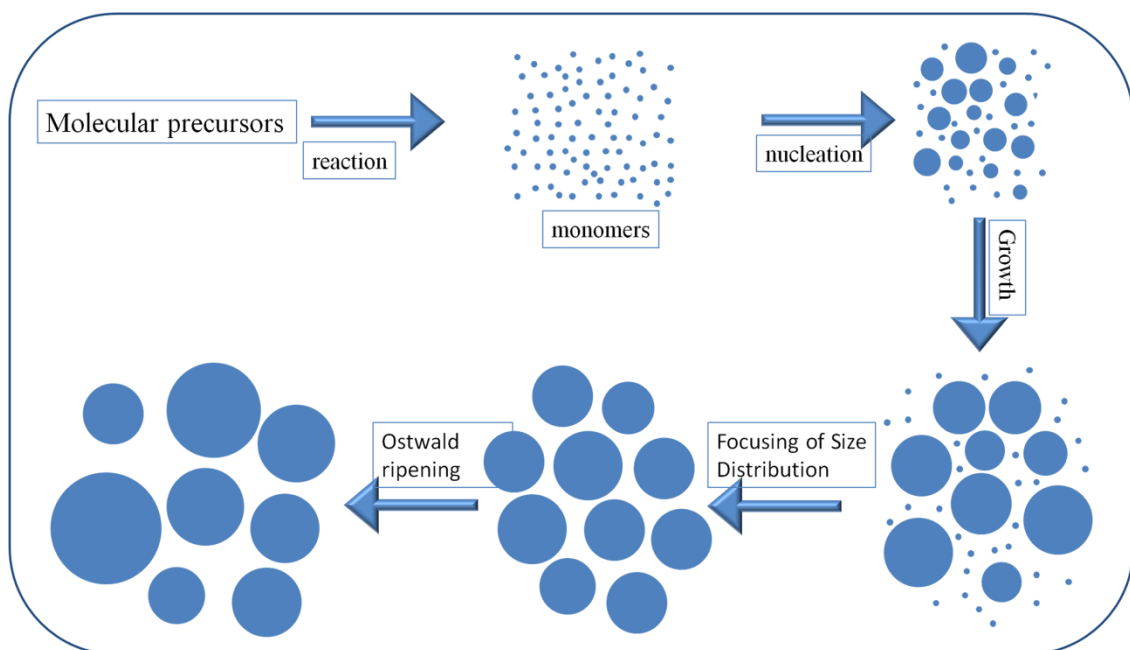


Figure 3.17 Schematic illustration of the formation mechanism of CTS nanoparticles.

3.3.3.4 Influence of reaction condition on the resulting nanoparticles

We have carried out several contrast experiments to study the influence of reaction conditions on formation of CTS nanoparticles. For example, when the precursor ratio of Cu:Sn:S was changed from 2: 1: 3 to 3: 1: 4 but maintaining the other conditions we found the final products showd uniform size and shape with an average size of 13.8 ± 1.8 nm, as shown in Figure 19 (a) and (b). The stoichiometry of the nanoparticles was determined to be 42.2: 17.2: 40.6 by measuring five randomly selected areas using EDX. XRD pattern reveals that the nanoparticles contain not only CTS phase, but also $\text{Cu}_{1.97}\text{S}$ and Sn_3S_4 phases. The reason for this is not clear, but one possible reason is that the ratio of 2: 1: 3 is more

favourable to form CTS in thermodynamic aspect. Therefore, we can conclude that the ratios of the precursor play an important role in the formation of phase pure CTS nanoparticles.

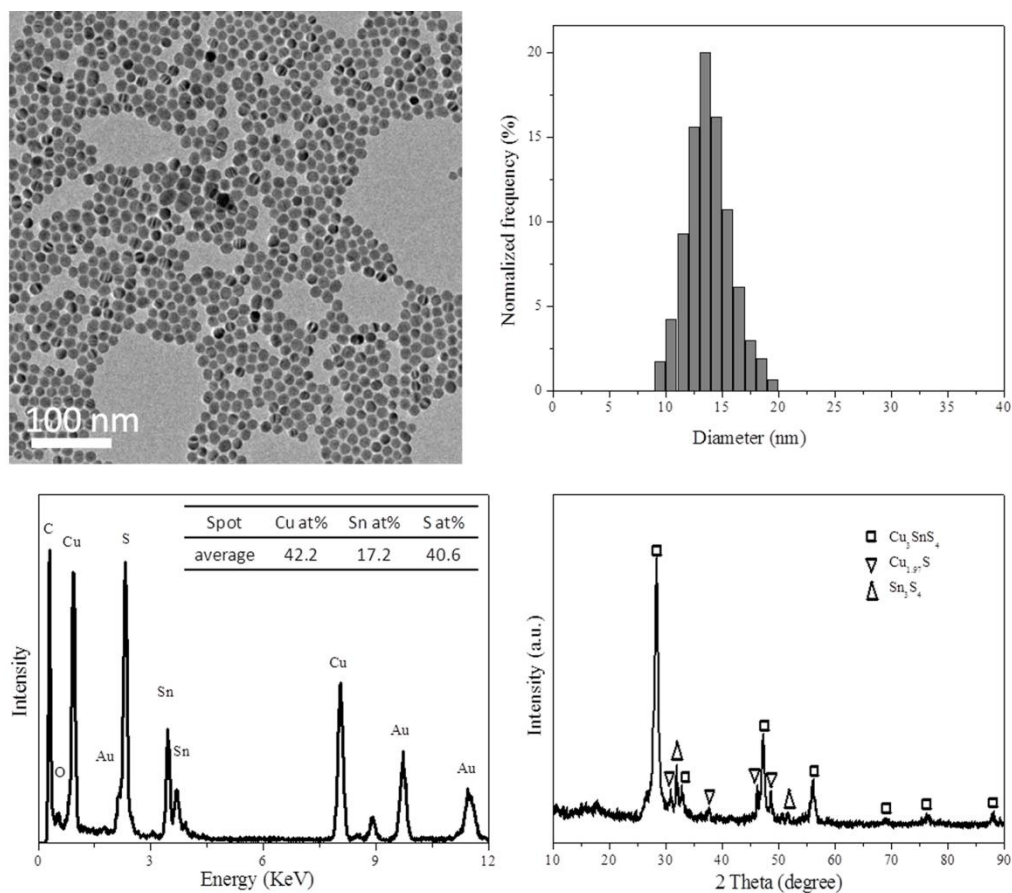


Figure 3.18 (a) low magnification TEM image of as-synthesized nanoparticles; (b) corresponding size distribution histogram; (c) EDX spectrum of the obtained nanoparticles; inset shows the average composition of five randomly selected areas, and (d) XRD pattern of the obtained sample.

3.4 Summary

In this chapter, the synthesis of ZnS, SnS, and CTS nanoparticles by heating up approach has been presented. The structural properties of the nanoparticles were studied by XRD and HRTEM.

ZnS nanoparticels with an average diameter of 4.8 ± 1.0 nm synthesized at $300\text{ }^{\circ}\text{C}$ show cubic zinblende structure. Due to quantum confinement effect, the as-synthesized ZnS nanoparticles exhibit larger band gap of 3.8 eV.

For the synthesis of SnS nanoparticels, the reaction temperature has great impact on both the morphology and structural properties. At $200\text{ }^{\circ}\text{C}$, the sample is consisted of both smaller nanoparticles with irregular shape and nanosheets. Structural analysis shows that the sample contains three phases, orthorhombic structure SnS and SnO and tetragonal structure SnO_2 . When the reaction temperature was raised to $250\text{ }^{\circ}\text{C}$, the sample contains much purer SnS phase with additional minor phase of SnO. Both of these phases have the orthorhombic structure. However, when the reaction temperature was further increased to $300\text{ }^{\circ}\text{C}$, hexagonal structure SnS_2 appears besides those orthorhombic structure SnS and SnO phases. In addition, higher ratio of sulfur precursors results in increasing concentration of SnS_2 phase in the final products.

Kuramite CTS nanoparticles with tetragonal structure have been synthesized at $250\text{ }^{\circ}\text{C}$. We have studied the growth kinetics of the CTS nanoparticle by analysis of the samples extracted at different reaction stages using TEM. Based on the statistical analysis of the reaction, it was found that the nanoparticles growth followed the focusing of size distribution mechanism at the initial stage whereby the average particle size increased but the relative standard deviation decreased. The relative standard deviation reached its lowest value at the reaction time of 120 min. After that, the nanoparticles continued to grow via the Ostwald ripening process, resulting in increasing average particle size and broadening of size distribution.

4 Preparation, morphology and structure of $\text{Cu}_2\text{ZnSn}(\text{S}_x\text{Se}_{1-x})_4$ thin films

As it is known that the optoelectronic properties of semiconductor materials are closely related to materials properties such as crystal quality, chemical composition and phase purity, it is essential to understand the detailed morphological and structural properties before their further application in devices. This chapter will investigate the preparation conditions on the morphological and structural properties of CZTSSe thin films. This chapter starts with the experimental details on the deposition of CZTSSe thin films by spin coating of the mixed precursor inks consisting of ZnS, SnS and Cu_3SnS_4 nanoparticles dispersed in hexanethiol. Two series of thin films deposited by both non-ligand-exchange and ligand-exchange processes have been prepared. In section 4.2, the influence of the annealing temperature on the morphological and structural properties of CZTSSe thin films was examined by SEM, XRD and Raman spectroscopy. In the following we examined the effect of ligand-exchange processes on the morphological properties of the resulting thin films.

4.1 Preparation of $\text{Cu}_2\text{ZnSn}(\text{S}_x\text{Se}_{1-x})_4$ thin films

The preparation process of CZTSSe thin films includes four main steps, which can be summarised as a schematic diagram as shown in Figure 4.1. The first step is to formulate the inks by mixing the chalcogenide (CTS, ZnS and SnS) nanoparticles as synthesized in Chapter 3. The composition can be controlled by changing the ratio of the nanoparticle precursors. The second step is to deposit Cu-Zn-Sn-S precursor films by spin coating nanoparticle precursor inks at a certain rotating speed. After that, Cu-Zn-Sn-S precursor films were subjected to a heat treatment step at 170-200 and 350 °C for 2 min respectively. The aim of this step is to remove the organic solvent as well as part of the surfactants surrounded the nanoparticle precursors. In addition, the heat treatment process also helps to dense the film on the substrates otherwise the deposited layers may be dissolved back into the solvent again when the second spin coating processes. To obtain desired thickness (less than 5 μm), the steps II and III should be repeated before going to the final annealing step.

To examine the effect of ligand-exchange with ammonium sulphide $(\text{NH}_4)_2\text{S}$ of the precursor thin films on the morphology of the resulting CZTSSe thin films, the precursor thin

films were treated with 0.04 M $(\text{NH}_4)_2\text{S}$ methanol solution for 30 s after heat treatment at 170 °C for 2 min to allow the ligand exchange between organic surfactants and ammonium sulphide. The thickness of the thin films can be achieved by repeating step II and III. Finally, the resulting precursor films were subjected to annealing process at 400 to 580 °C under different sulphur and/or selenium containing atmosphere, which allows the formation of CZTSSe absorbers by reaction of the nanoparticle precursors.

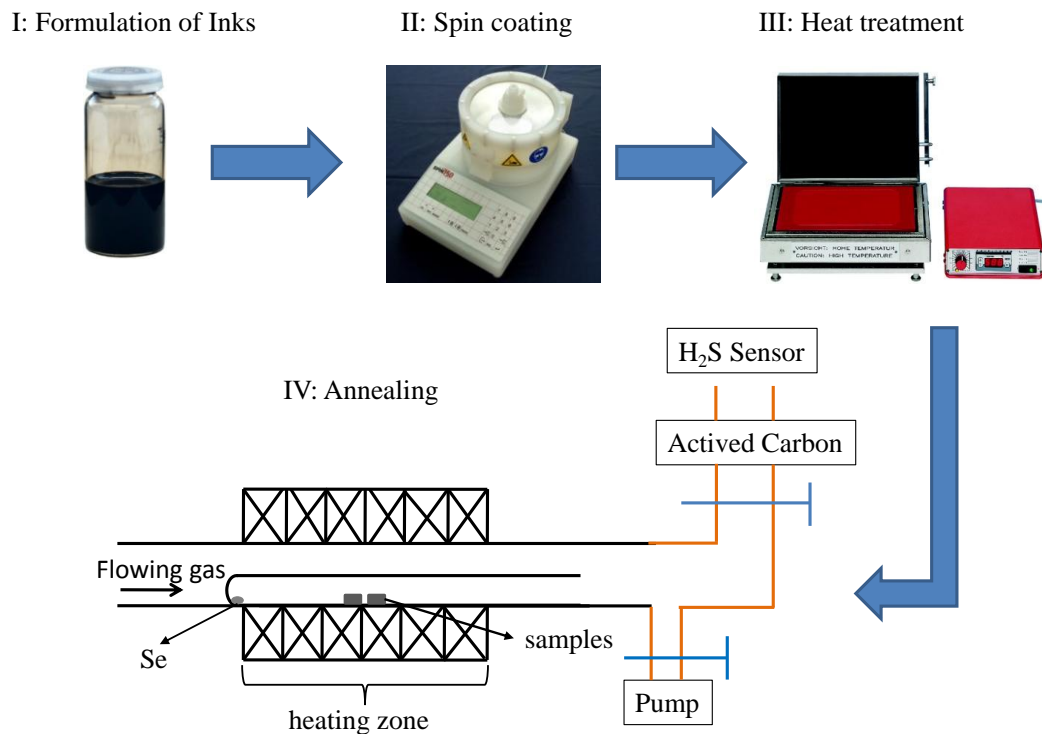


Figure 4.1 schematic diagrams showing the preparation process of CZTSSe thin films. In the annealing step, the gas waste was passed through activated carbon before going into the air. In addition, for the safety reason a H_2S sensor is installed on top of the gas outlet to check the H_2S .

The annealing was done in a Gero split-tube furnace with one heating zone. The annealing temperature was controlled by a controlling device which allows programming the annealing profile as designed. The samples were placed at the centre of the heating zone inside a quartz tube in the case of annealing under Ar- H_2S (5 %) atmosphere. When annealed under Ar-Se or Ar-Se- H_2S atmosphere, the samples were loaded in a one end closed quartz tube which was

Table 4.1 Detail preparation parameters of CZTSSe samples at different temperatures and atmosphere. All samples were prepared using the same nanoparticle precursors containing 1 mmol CTS-C, 1.75 mmol ZnS and 0.75 mmol SnS-300 in 1-hexanethiol. The samples were deposited on glass substrates.

Name of sample	Number of layers	Heat treatment		Annealing conditions										
		T. (°C)	time (min)	T (°C)	time (min)	atmosphere								
133-as-dep.	4	170 °C, 2 min 350 °C, 2 min		/	/	/								
133-400H ₂ S			400	25	Ar-H ₂ S(5%)									
133-450H ₂ S			450			Ar-H ₂ S(5%)								
133-500H ₂ S			500				Ar-H ₂ S(5%)							
133-540H ₂ S			540					Ar-H ₂ S(5%)						
133-580H ₂ S			580						Ar-H ₂ S(5%)					
133-400Se			400							Ar-Se				
133-450Se			450								Ar-Se			
133-500Se			500									Ar-Se		
133-540Se			540										Ar-Se	
133-580Se			580											Ar-Se

Table 4.2 CZTSSe Samples prepared from different using ligand-exchange procedures. After each spin coating process, the precursor film was heat treated at both 170 °C and 350 °C for 2 min. The ligand-exchange step was performed after 170 °C heat treatment. The substrates used in this series of samples were Mo coated soda lime glass substrates.

	precursors	No. of layers	annealing conditions			Ligand-exchange with 0.04 M (NH ₄) ₂ S Me-OH solution for around 30 s
			T (°C)	Time (min)	atmosphere	
137-1-CZTSSe	0.67 mmol CTS-B, 1.37 mmol ZnS and 0.45 mmol SnS-300	4	580	25	Ar-Se	All four layers
137-2-CZTSSe		5				First four spin coated layers
137-3-CZTSSe		4				Only for the first spin coated layer
145-CZTSSe		3				5
	0.67 mmol CTS-B, 1.45 mmol ZnS and 0.65 mmol SnS-300	2		25		Only for the last spin coated layer

placed inside a larger quartz tube, as shown in Figure 4.1. Selenium powder was placed at the closed end of the smaller quartz tube (see Figure 4.1). Both ends of the quartz tube in contact with the heating furnace were connected to gas-inlet and outlet, which allows the flowing of gas during annealing process. Before starting heating, the quartz tube was evacuated and filled with argon three times. The annealing was done under atmosphere pressure. The detail preparation parameters of different samples are shown in Table 4.1.

4.2 Results and discussions

Results and discussions of the influence of annealing temperature and atmosphere on the morphological and structural properties of the resulting $\text{Cu}_2\text{ZnSn}(\text{S}_x\text{Se}_{1-x})_4$ thin films will be presented in this section. In addition, the effect of ligand-exchange processes of the precursor layers on the morphology of CZTSSe thin films will also be discussed.

4.2.1 Influence of the annealing temperature and atmosphere

In this section, the influence of the annealing temperature and atmosphere on the morphological and the structural properties will be investigated. The aim of this study is to determine the suitable temperature and atmosphere for preparation of the CZTSSe thin film absorbers. The morphology was studied by scanning electron microscopy while the structural properties were characterized by XRD as well as Raman spectroscopy. The use of Raman spectroscopy as a supplementary tool for analysis of the structural properties is essential because the overlapping of the main diffraction peak among CZTS(Se), ZnS(Se), CTS(Se) and $\text{Cu}_2\text{SnS}(\text{Se})_3$.

4.2.1.1 Morphology analyzed by SEM

As-deposited sample (133-as-dep.)

Figure 4.1 shows the surface and cross section SEM images of the as-deposited sample after heat treatment process. When taking a close look at the surface of the sample, one can find that there are some nanoplates on top or embedded in the nanoparticle layers as marked by circles. As shown in Chapter 3, the size of the ZnS and CTS nanoparticles is rather small (less than 50 nm) and the shape of these two kinds of nanoparticles are spherical; but the shape of

the SnS nanoparticles are composed of sphere and nanoplates. Therefore, it is clear that the nanoplates observed from the surface view of SEM image should be SnS precursor. In addition, pinholes can also be observed in the sample, however, it is not clear whether these pinholes last until the substrates or not. The films were prepared using layer by layer deposition process. This process allows the further coverage of the pinholes or cracks existed in the pre-deposited layers. Hence, the pinholes are more probably present only on the surface layers. Figure 4.1 (b) illustrates that the film is densely packed. The thickness of the sample is around 0.9 μm .

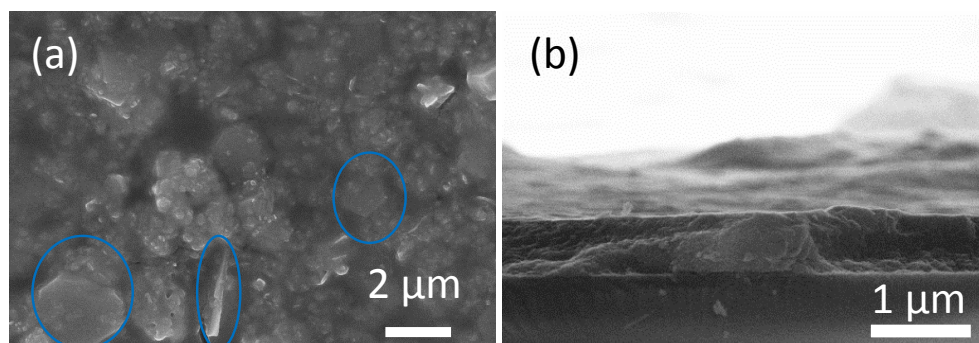


Figure 4.2 SEM images of 133-as-dep. CZTSSe precursor films: (a) top view and (b) cross section.

Samples annealed in Ar-H₂S (5 %) atmosphere

To study the annealing temperature effect on the morphologies of the samples annealed in H₂S atmosphere, SEM measurements were performed on both surface and cross-sectional view, as shown in Figure 4.3. The morphologies of the samples annealed at 400, 450 and 500 °C show no obvious difference, which is also true in terms of the size of the particles. However, when the annealing temperature was further increased to 540 °C, some of the smaller nanoparticles started to grow into larger particles with a size around 250 nm. The growth only occurred at some part of the samples (marked as circle in Figure 4.3 (g)), leaving a large area composed of only nanoparticles. Larger grains up to 1 μm were found in the samples annealed at 580 °C, Figure 4.3 (i). But the growth of the grains did not extend to the whole surface, which is similar with that in sample annealed at 540 °C. The cross section of layers with larger grains was shown in Figure 4.3 (j) which reveals a double-layered

structures with a thickness of $0.71 \pm 0.32 \mu\text{m}$ upper larger grain layer and a thickness of $0.7 \pm 0.1 \mu\text{m}$ bottom fine grain layer.

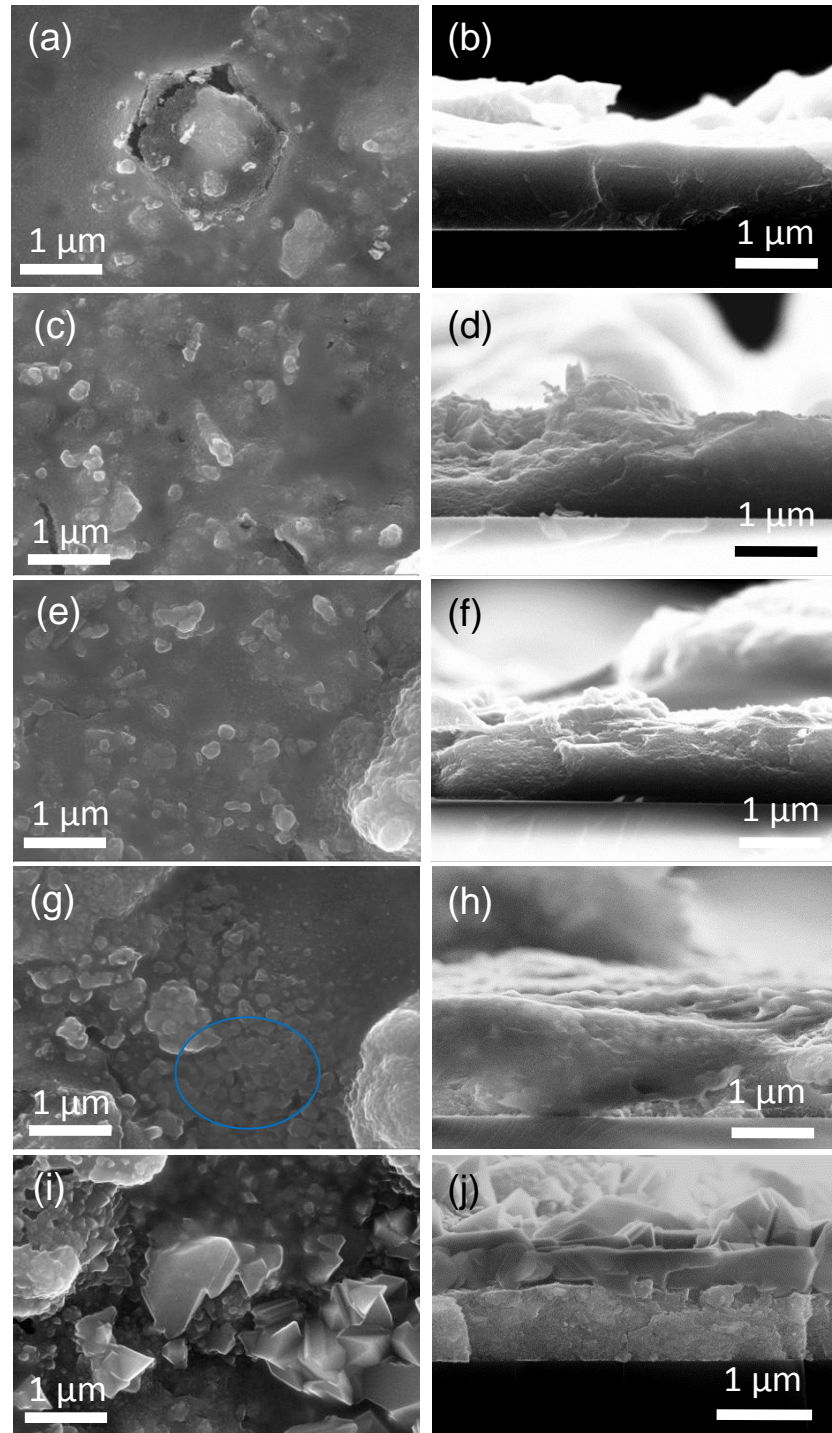


Figure 4.3 Top view and cross sectional SEM images of samples annealed at different temperatures under Ar-H₂S (5 %) atmosphere: (a) and (b) 133-400H₂S, (c) and (d) 133-450H₂S, (e) and (f) 133-500H₂S, (g) and (h) 133-540H₂S, (i) and (j) 133-580H₂S.

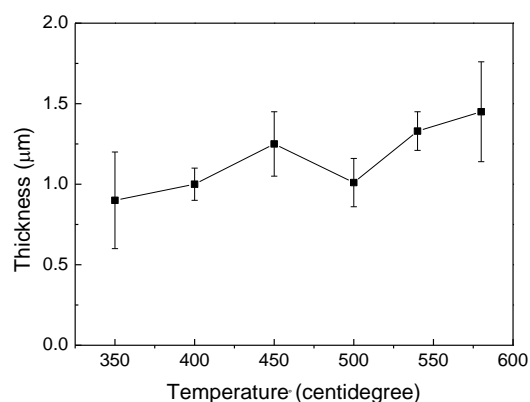


Figure 4.4 Evolution of the layer thickness with annealing temperatures. The thickness is determined from the cross sectional SEM images.

The thickness, as determined from the cross sectional images, of all these five annealing samples including the as-deposited sample are summarized in Figure 4.4. The average thickness of the samples increased gradually with increasing annealing temperatures except for the 133-500H₂S sample which shows a thickness of $1.01 \pm 0.15 \mu\text{m}$. This value is smaller than the value of $1.25 \pm 0.20 \mu\text{m}$ for the 133-450H₂S sample. The explanation for the increasing thickness is that as the annealing temperature increase the reaction between CTS, ZnS, SnS and H₂S become stronger and more sulfur was incorporated into the the layers.

Samples annealed in Ar-Se atmosphere

Figure 4.5 illustrates the evolution of the morphology of samples annealed in Ar-Se atmosphere at different temperatures for 25 min. The evolution of the morphology in this series of samples is different with that in the series of sample annealed in H₂S atmosphere. The reaction among the nanoparticle precursors seems to be much stronger in Ar-Se atmosphere than in Ar-H₂S (5 %) atmosphere because large particles up to 1 µm have already been formed at the lower temperature of 400 °C. As can be seen from Figure 4.5 (a), there are some larger grains scattering round the surface while underneath are dense nanoparticle layers. Cracks were also observed from the surface view. The cross sectional image (Figure 4.5 (b)) confirms the observation, showing densely packed nanoparticle bottom layers with a thickness of $1.2 \pm 0.2 \mu\text{m}$ and a inhomogeneous top large grain layer.

The morphology of sample 133-450Se annealed at 450 °C are different from that of the previous one. Particles with an approximate size of 400-600 nm can be seen from the surface of this sample (Figure 4.5 (c)). Most of these particles connect to each other, exhibiting the trend to grow together into larger particles when annealed at higher temperature. Besides these connected particles, some larger particles with a size of 2 μm are also found on the surface. Instead of large particles, only nanoparticles can be found from in some area of the sample, indicating that the sample is not uniform. The cross sectional image shown in Figure 4.5 (d) reveals a similar larger grain and fine grain double-layered structure with the 133-400Se sample. Unlike the 133-400Se sample, the upper layer in this sample exhibits better coverage of the larger grains over the bottom fine grain layer. The thickness of the upper layer was determined to be 0.51 μm in average.

Upon annealing at 500 °C (sample 133-500Se), the crystal continues to grow. The surface SEM image (Figure 4.5 (e)) shows that most of the area is cover by large grains with a size around 1 μm . A representative cross sectional SEM image is shown in Figure 4.5 (f). This image illustrates that the thin films are composed of a double-layered structure, which is similar to samples 133-400Se and 133-450Se. However, the larger grain layer is much uniform in this sample compared with the other two samples.

When the annealing temperature is further raised to 540 °C (sample 133-540Se), the surface morphology as well as the cross sectional morphology shows no much difference with the 133-500Se sample. The dominated size of the particles is over 1 μm . The thickness of the sample is around $1.8 \pm 0.2 \mu\text{m}$ as revealed by the cross sectional SEM image (Figure 4.5 (f)).

In the series of samples annealed under H_2S ambiance, we found that only when the annealing temperature was raised to 580 °C large grains can be formed. Hence here we also examined this temperature under Ar-Se atmosphere. More uniform grain size as well as smoother surface was obtained (Figure 4.5 (f)). However, even at this temperature, the nanoparticle bottom fine grain layer remains.

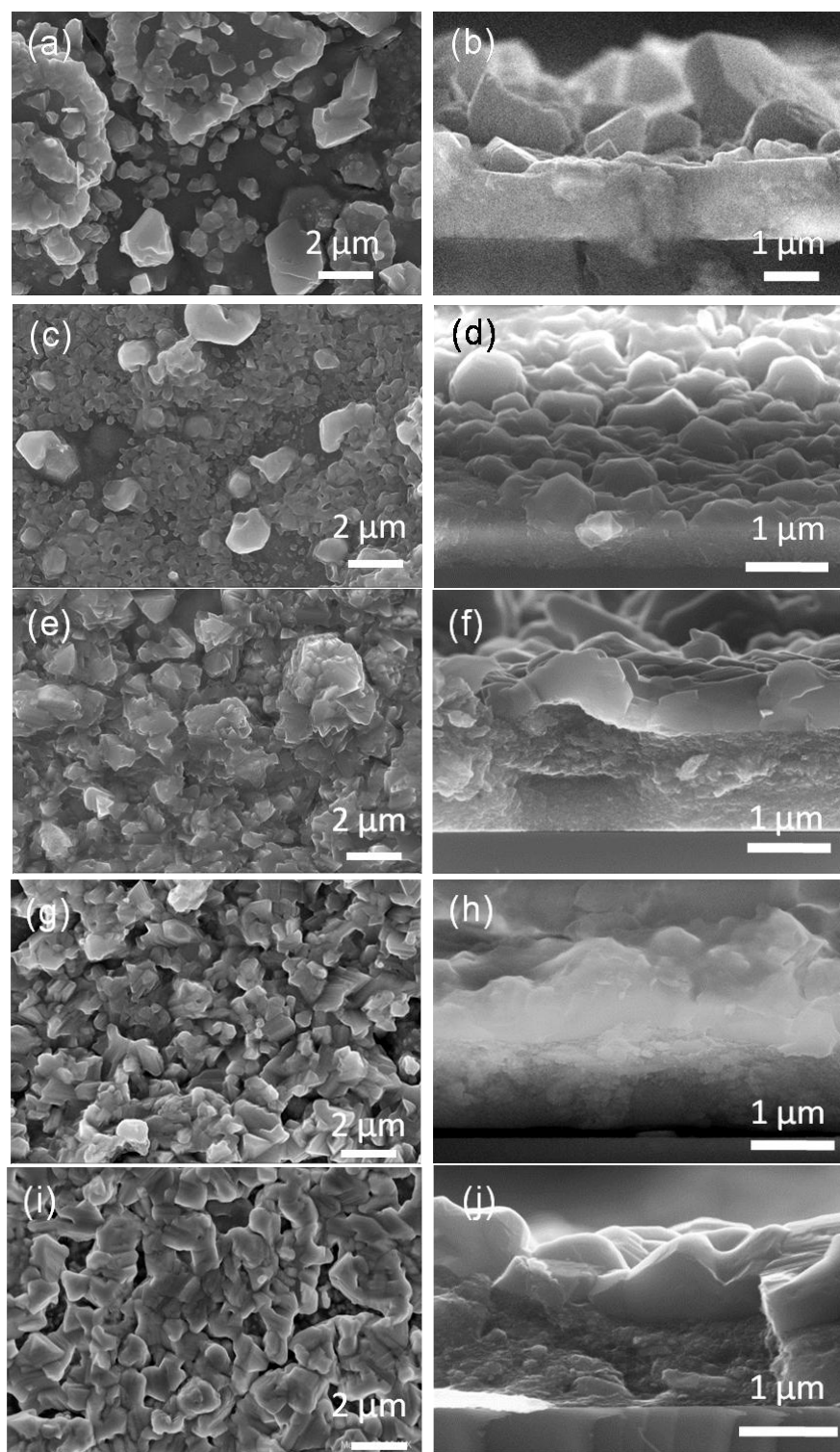


Figure 4.5 Evolution of morphology of samples annealed at different temperature in Ar-Se atmosphere as illustrated by top view and cross sectional SEM images: (a) and (b) 133-400Se, (c) and (d) 133-450Se, (e) and (f) 133-500Se, (g) and (h) 133-540Se, (i) and (j) 133-580Se. All the samples are on glass substrates.

One of the similar phenomenon for all these samples is that the existence of a double-layered structure which is unlikely to be observe in the vacuum deposition process where the sample normally is composed of a single compacted layer. The main reason for this double-layerd structure is that the nanoparticle precursors are capped by the oleylamine surfactant. To remove this organic surfactant by annealing is difficult especially when the upper larger grain compact layer has been formed because this layer blocks the evaporation of this surfactant. This organic surfactant remained in the samples may change to carbon as the annealing temperature increases, which acts as a barrier for the crystal growth. Actually, this kind of structure has been observed in several groups who work on the solution processing preparation of thin films using either organic surfactant capped nanoparticles or metal salts dissolved in organic solvent as precursors [45, 88, 89]. For example, Guo *et al.*[88] observed a double-layered structure when they prepared $\text{Cu}_2\text{Zn}(\text{Ge},\text{Sn})(\text{S},\text{Se})_4$ thin film absorbers by annealing the oleylamine capped $\text{Cu}_2\text{Zn}(\text{Ge},\text{Sn})\text{S}_4$ nanoparticle films.

Table 4.3 Thickness of samples annealed at different temperatures under Ar-Se atmosphere together with the thickness of the upper large grain layer. The values are determined from cross sectional SEM images. For comparison, thickness of the as deposited sample is also listed.

	133-as-dep.	133-400Se	133-450Se	133-500Se	133-540Se	133-580Se
Layer thickness (μm)	0.9 ± 0.3	1.8 ± 0.6	1.3 ± 0.3	1.7 ± 0.1	1.8 ± 0.2	1.8 ± 0.2
Thickness of large grains (μm)		0.6 ± 0.2	0.5 ± 0.2	0.7 ± 0.1	0.7 ± 0.1	0.8 ± 0.1

Table 4.3 summarizes the thickness of these five samples together with the thickness of the upper large grain layer. The average thickness of all the samples was increased compared with the as-deposited sample which should be due to incorporation of selenium into the samples by the reaction of CTS, ZnS and SnS precursors. A slightly increase of the thickness of the upper large grain layer was observed. For example, the thickness of the upper layer increased from $0.63 \pm 0.15\mu\text{m}$ for the 133-400Se sample to $0.8 \pm 0.1\mu\text{m}$ for 133-580Se sample.

Chemical composition determined by XRF

The chemical composition of the samples are analysed by XRF, as shown in table 4.4. Since the calibration was based on the Mo substrate samples, sulphur was not calibrated due to the overlapping of S and Mo peak. All the samples are Sn-rich except for 133-580Se sample. According to the phase diagram reported by Piskach *et al.* [90, 91], Sn-containing secondary phases like SnS(Se), and SnS(Se)₂ may exist in the samples. The detail analysis of structural properties is shown in next section. The Sn content of the samples decreased dramatically when annealing temperature reached 580 °C, this could be due to the loss of Sn by evaporation of SnS_xSe_{1-x} during annealing process. Several publications have discussed about the Sn loss during the annealing process when preparing the CZTSSe absorbers [92-94]. The loss of Sn was found to be as the form of SnS gas due to the high vapour pressure of SnS. Additionally, upon annealing under Ar-Se atmosphere, increasing ratio of Se was detected with annealing temperature. It should be noted that the ratio of Se as shown in the table is not correct in terms of the complete composition of the absorber layers because the calculation did not take Sulfur into account.

Table 4.4 Relative chemical composition of as-deposited and annealed samples as determined by XRF measurements. It should be noted that the calibration was only carried out on Cu, Zn, Sn and Se elements.

	Cu/(Zn+Sn)	Zn/Sn	Se	Sn	Zn	Cu
133-as-dep.	0.98	0.66		30.3	20.2	49.5
133-400H ₂ S	0.97	0.73		29.3	21.5	49.2
133-450H ₂ S	0.98	0.66		30.3	20.1	49.6
133-500H ₂ S	0.99	0.71		29.4	20.8	49.8
133-540H ₂ S	1.02	0.62		30.5	19.0	50.5
133-580H ₂ S	1.01	0.69		29.4	20.3	50.3
133-400Se	1.11	0.71	24.94	20.8	14.8	39.4
133-450Se	1.05	0.76	33.8	18.3	14.0	33.9
133-500Se	1.06	0.68	36.7	18.3	12.4	32.6
133-540Se	1.05	0.67	37.01	18.4	12.3	32.3
133-580Se	0.98	1.13	39.45	14.3	16.2	30.0

4.2.1.2 Structural characterization by XRD and Raman spectroscopy

Since the XRD patterns of CZTS(CZTSe) are overlapping with that of CTS(CTSe) and ZnS(ZnSe), Raman spectroscopy are used as supplemental tool for characterization of the structural properties of the CZTSSe samples.

4.2.1.2.1 XRD studies

Sample 133-as-dep. (Precursor films)

Figure 4.6 (d) shows the XRD pattern of a four deposited layers sample on glass substrate with heat treatment at 350 °C for 2 min in air for each layer. Nearly all of the peaks can be attributed to the CTS, ZnS, SnS and SnS₂ nanoparticles precursors except the peak marked with circle arising from CuS phase. The appearance of this peak suggests due to the reaction between ZnS and CTS resulting in the formation of CZTS and generation of CuS secondary phase. The peaks corresponding to CZTS are overlapping with those of CTS and ZnS. The reaction can be described by the following equation.



According to Schorr *et al.*[95] who investigated the formation of CZTS from the solid state reaction of CuS, SnS and ZnS powder precursors using in-situ high temperature synchrotron X-ray diffraction, the formation of CZTS was found to start just below 300 °C. In addition, recently Hsu *et al.*[96] studied the reaction pathway of CZTSSe absorbers prepared from the binary chalcogenides by hydrazine-based solution process, they found that the CZTSSe was formed at 350 °C by the reaction of Cu₂SnS(Se)₃ and ZnS. Therefore, it is reasonable that, in our system, the formation of CZTS started at 350 °C.

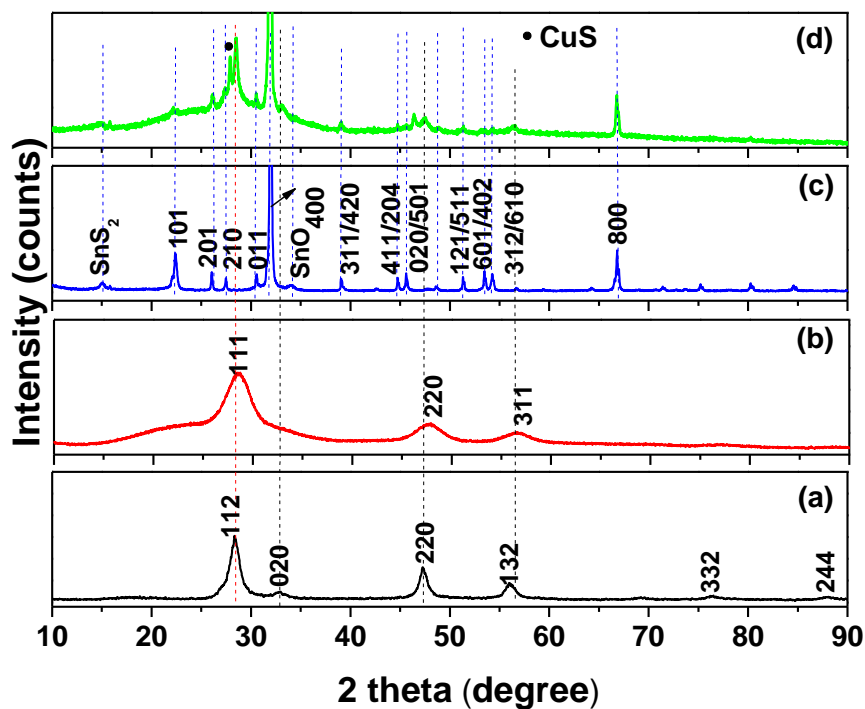
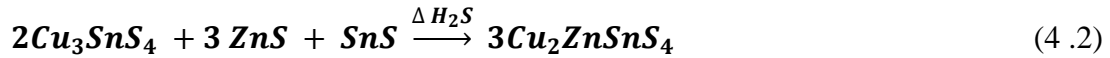


Figure 4.6 (d) XRD patterns of precursor films on glass substrate. As references, XRD patterns of (a) CTS, (b) ZnS and (c) SnS nanoparticles precursors were also shown below.

Samples annealed in Ar-H₂S (5 %) atmosphere

Figure 4.7 illustrates the XRD patterns of samples deposited by the same conditions on glass substrates but annealed at different temperatures in Ar-H₂S (5 %) atmospheres. Most of the peaks can be indexed to CZTS while those peaks located at $2\theta = 31.9$ and 66.6° can be assigned to SnS precursors. The existence of the SnS phase is expected because XRF analysis shows that these samples are Sn-rich. The intensity of the peaks corresponding to CZTS increased with increasing annealing temperatures, which implies better crystal quality with increasing annealing temperatures. Note that due to the overlapping of the main diffraction peaks of CZTS phase with that of ZnS and CTS phases, the coexistence of the secondary phases like ZnS and CTS cannot be excluded in all the samples annealed at temperatures. On the other hand, the intensity of the SnS peaks decreased gradually with increasing annealing temperatures; especially when the annealing temperature reached 580°C these two peaks disappeared. The decrease of the SnS signal is due to the reduced amount of SnS in the samples

because of the reaction among SnS, ZnS and CTS precursors to form CZTS. The reaction can be described by Equation (4.2).



Another possible reason for the decrease of SnS signal is the conversion of this phase into SnS₂ phase at higher annealing temperature (> 540 °C) because a peak at $2\theta = 15.4^\circ$ related to the SnS₂ phase shows higher signal in the samples annealed at 540 and 580 °C compared with the other three samples. Since the loss of Sn as the form of SnS is known during the annealing process, it is also possible that the decrease of the SnS signal is due to the higher evaporation rate of SnS at increasing temperature. However, the chemical composition analysis shows no too much difference for the tin content. Hence, the loss of tin is not the case for the decrease of XRD signal of SnS phase.

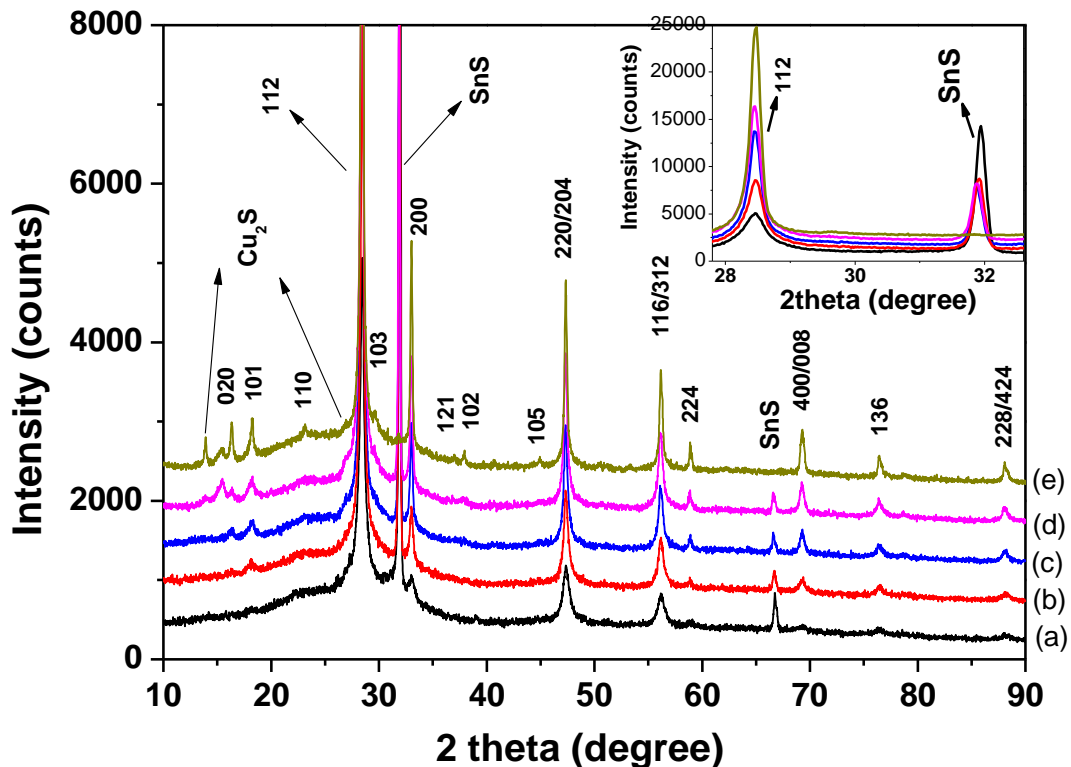


Figure 4.7 XRD patterns of samples annealed under Ar-H₂S (5 %) atmosphere at different temperatures: (a) 133-400H₂S, (b) 133-450H₂S, (c) 133-500H₂S, (d) 133-540H₂S, and (e) 133-580H₂S. The inset is the enlarged part of 2θ between 27.5° and 33.5° .

Samples annealed in Ar-Se atmosphere

For the annealing under selenium containing atmosphere, the selenium was placed at the one end of the quartz tube which was situated inside another quartz tube, as shown in Figure 4.1. For this series of sample the formation of CZTSSe can be generally described by equation (4.3).



Figure 4.8 shows the XRD patterns of samples annealed under Ar-Se vapour atmosphere at different temperatures. Similar phenomenon compared with the samples annealed in Ar-H₂S (5 %) atmosphere where the signal from CZTS was enhanced but SnS signal decreased with increasing annealing temperatures was observed. However, the diffraction patterns also exhibit some different behaviors. For example, when annealed under Ar-Se atmosphere, the peak at 31.9° from SnS decreased dramatically in the 133-450Se sample indicating that there was a strong reaction among the precursors to form the CZTSSe. Particularly, the intensity of the peaks corresponding to the CZTSSe increased gradually with increasing annealing temperature before 540 °C and a significant increase can be observed for sample annealed at 580 °C. Besides the increase of intensity with temperature, the shift of the XRD patterns to lower angle with increasing annealing temperatures were also observed. This is due to the increasing amount of sulfur was replaced with selenium which gives rise to the expansion of the lattice distances because the ionic radius of selenium (1.98 Å) is larger than that of sulfur (1.84 Å). For instance, the (112) peak position shifts from $2\theta = 27.63^\circ$ to $2\theta = 27.35^\circ$ when the annealing temperature increases from 400 to 580 °C.

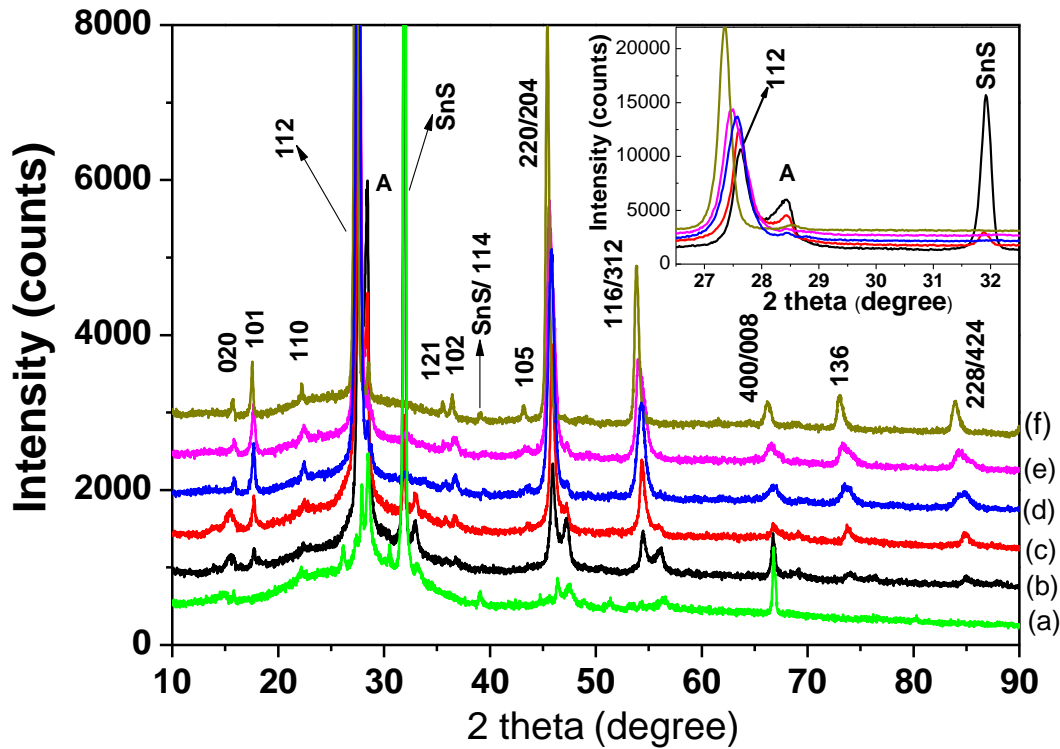


Figure 4.8 XRD patterns of samples annealed under Ar-Se atmosphere at different temperatures at: (b) 133-400Se, (c) 133-450Se, (d) 133-500Se, (e) 133-540Se, and (f) 133-580Se. The inset is the enlarged part of 2θ between 26.5° and 32.5° . For comparison, the XRD pattern of the precursors' films 133-as-dep. (a) is shown.

Except for those peaks assigned to CZTSSe and SnS, there is another peak located in between 28° and 29° for all the samples, which is named as peak A. This peak can be attributed to ZnS and CTS precursors. This peak is located at 28.44° - 28.45° for samples 133-400Se, 133-450Se, 133-500Se and 133-540Se, which is slightly smaller than the main diffraction peaks of ZnS and CTS precursors. We attributed this peak to Zn(S,Se) and CTSSe which formed by the reaction of the ZnS and CTS with selenium during the annealing. When annealing temperature was raised to 580°C , peak A shifted to 28.52° for sample 133-580Se. The interplanar distance of this peak was calculated to be 3.127 \AA , which is close to that of (103) planes at 3.129 \AA for the CZTSSe sample 133-580Se (see Table 4.5). Therefore, this peak can be indexed to (103) of CZTSSe.

The intensity of the peak A decreased with increasing annealed temperature before 500 °C. The explanation for this behavior is that more and more ZnS and CTS precursors reacted with SnS under the Se-containing atmosphere leading to the formation of CZTSSe as the increase of annealing temperature. However, for the annealing temperature above 500 °C, nearly no change in term of the intensity for this peak can be observed, indicating that most of the ZnS and CTS reacted with SnS. This result is in agreement with the variation of SnS signal in the XRD patterns as mentioned above where the main peak of SnS at 31.9° disappeared at and above 500 °C.

The lattice constants of samples with tetragonal structure were also estimated by the following equation:

$$\frac{1}{d^2} = \frac{h^2}{a^2} + \frac{k^2}{b^2} + \frac{l^2}{c^2} \quad (4.4)$$

where d is the d-spacing (interplanar distance), a, b and c represent the lengths of the unit cell edges; h, k, and l are called crystallographic or Miller indices. It should be pointed out that $a = b \neq c$ in the case of tetragonal structure. The value of d can be calculated by using the Bragg's law:

$$d = \frac{n\lambda}{2\sin\theta} \quad (4.5)$$

The lattice constants were determined by using the Bragg peak of (101) and (112), which was summarized in table 4.3. The value of $c/2a$ is related to the tetragonal distortion which may influence the electronic structure of the materials. The deviation of 1: $(c/2a) \neq 1$ leads to a crystal field and a non-degenerate valence band maximum [97]. All the samples show a similar $c/2a$ value which is slightly less than 1. This is in good agreement with the literature reports for the thin film samples [94]. For example, Siebentritt *et al.* [97] have observed that the $c/2a < 1$ in thin film samples while $c/2a > 1$ in single crystal samples. The volume of the unit cell increased with increasing annealing temperature due to the increasing replacement of S with Se in CZTSSe samples.

Table 4.5 Diffraction angles and interplanar spacing distance of (101) and (112) reflections and lattice constants calculated from these two lattice planes. The interplanar spacing distance d_{103} of (103) plane from CZTSSe was also calculated using equation (4.4) while the d value of reflection A was calculated from the Bragg's Law (Equation (4.5)).

	$2\theta_{(101)}$	d_{101} (Å)	$2\theta_{(112)}$	d_{112} (Å)	a (Å)	c (Å)	V of unit cell (Å ³)	c/2a	d_{103} (Å)	$2\theta_A$ (°)	d_A (Å)
133-400Se	27.63	5.008	27.63	3.230	5.597	11.136	350.042	0.9929	3.093	28.44	3.137
133-450Se	27.61	5.011	27.61	3.233	5.602	11.140	350.800	0.9939	3.095	28.44	3.137
133-500Se	27.57	5.018	27.57	3.238	5.613	11.147	352.875	0.9981	3.098	28.45	3.136
133-540Se	27.48	5.036	27.48	3.248	5.622	11.216	356.096	0.9943	3.113	28.45	3.136
133-580Se	27.35	5.056	27.35	3.262	5.648	11.265	360.594	0.9950	3.127	28.52	3.129

According to Momose *et al.* [98], the relationship between $[S]/([S] + [Se])$ and the diffraction angle follows the Vegard's law [99]:

$$2\theta_{CZTSSe} = x \cdot 2\theta_{CZTS} + (1 - x) \cdot 2\theta_{CZTSe} \quad (4.6)$$

where 2θ represents the diffraction angle of the Bragg peak. Regarding to equation (4.2) and by using the Bragg peak of (112), the value of x was determined to be 0.37, 0.36, 0.31, 0.25 and 0.16 for samples 133-400Se, 133-450Se, 133-500Se, 133-540Se, and 133-580Se, respectively.

4.2.1.2.2 Raman spectroscopy analysis

Although XRD has been considered as a powerful tool for analysis of the structural properties and phase purity of materials, it is difficult to distinguish secondary phases, i.e. ZnS and Cu_3SnS_4 , from Cu_2ZnSnS_4 due to the overlapping of the main XRD patterns of ZnS, CTS, and CZTS. Therefore, it is significant to use another method together with XRD to characterize the phase purity of the obtained samples. Raman spectroscopy detects the optical phonon vibrational modes at the zone center and has been proved to be an useful tool for detecting the secondary phases presented in CZTSSe thin films [100-103]. Raman spectroscopy analysis of CZTS was firstly reported by by Himmrich *et al.* in 1991 [104]. In their analysis, they assumed that the CZTS crystallized in stannite type structure. However, since both theoretical calculations and experimental results have demonstrated that kesterite is the most stable structure for both CZTS and CZTSe [14, 15], here we assume that our CZTSSe compound adopts the kesterite type structure. A group theory analysis performed by Sarswat *et al.* [105] using the Bilbao Crystallographic server resulted in 3A, 6B, 6E Raman active modes. It should be noted that for modes of B and E, a LO-TO splitting is observed. For better

comparison of our Raman results with the referecces data, Raman mode for kesterite type CZTS is summarized in Table 4.6.

Table 4.6 Literature survey: Raman modes attributed to CZTS. Data in Ref. [106] is from theoretical calculation and the others are experimental data.

Predicted mode	Raman shift (cm-1)					
	Gürel <i>et al.</i> [106]		Fontané <i>et al.</i> [107]	Fontané <i>et al.</i> [108]	Fernandes <i>et al.</i> [100]	Yoo <i>et al.</i> [109]
E(TO LO)	79.2	79.2	66	/	/	/
B(TO LO)	92.3	92.3	83	/	/	/
E(TO LO)/ B(TO LO)	101.4 104.2	101.4/ 104.2	97	96	/	/
E(TO LO)/ B(TO LO)	166.1 179.6	166.2/ 179.9	143, 166	166	/	/
B(TO LO)	269.1	285.5	252	/	256-257	251-252
E(TO LO)	278.2	289.8	272	/	/	/
A		302.1	287	286	288	288-289
A		309.0	/	/	/	/
E(TO LO)	309.7	314.1	/	/	/	/
A		335.2	337	337	338-389	337-338
B(TO LO)	332.7	336.1	/	/	/	
E(TO)		341.4	347	/	/	352-354
E(LO)/B(TO)		353.2/354.8	353	352	/	/
B(LO)		366.4	/	370	/	/

In a Raman spectrum the A-modes describe entirely symmetric vibrational modes and usually show the highest scattering intensity. In the CZTS or CZTSe crystal lattice, the A vibrational modes originate from the vibrations of S or Se atom surrounded by the other metal atoms and the vibrational frequency is given by equation (4.7) [110, 111].

$$\nu = \sqrt{\frac{2\alpha_{Cu-VI} + \alpha_{Zn-VI} + \alpha_{Sn-VI}}{M_{VI}}} \quad (4.7)$$

where α_{X-VI} (i.e. X= Cu, Zn, Sn and VI = S, Se) are the bond-stretching force constants related to the interaction between the nearest neighbors, and M_{VI} is the mass of S or Se ($M_S = 32.07$, $M_{Se} = 78.96$). Hence the frequency corresponding to A mode of CZTS should shift

towards lower frequency with the when S is partiallyly replaced by Se in CZTSSe solid solution [3, 111].

In this thesis, the Raman spectroscopy measurements were performed at room temperature using a Ti: Sapphire-ring-laser was used as an excitation. The wavelength of the laser is fully tenable from 690 nm to 1050 nm. To avoid laser heating the beam power was kept below 3.5 mW. Raman spectra were recorded with a Horiba T64000 triple monochromator system in backscattering configuration with a microscope and a motorized XY stage. The micro-Raman spectroscopy with a 100x objective was performed at room temperature with a wavelength of 747 nm.

Raman spectroscopy analysis of samples annealed in Ar-H₂S (5 %) atmosphere

Figure 4.9 shows the Raman spectra for samples annealed at different temperatures under Ar-H₂S atmosphere, together with the fitting of the peaks with lorentzian curves. The Raman spectrum of the 133-as-dep. sample exhibites six peaks located at 217, 288, 315, 331, 344 and 366 cm⁻¹. The most intensive peak is situated at 331 cm⁻¹, which is close to the theoretical calculated A mode for kesterite type CZTS repored at 335 cm⁻¹ by Gürel *et al.* [106] (see Table 4.6). This value is also in good aggreement with the reported experimental value at 332 cm⁻¹ for CZTS nanocrystals [112] and 331- 334 cm⁻¹ CZTS thin films [113]. The peak at 288 cm⁻¹ corresponds to the A mode of kesterite type CZTS whiel the peak at 366 cm⁻¹ is related to the B(LO) mode of kesterite type CZTS [106-108]. The appearance of these peaks further confirms the formation of CZTS in the sample of 133-as-dep. The second strongest peak at 217 cm⁻¹ can be assigned to A_g mode of SnS that is one of the precursors in the layers [114, 115]. The weaker peaks at 315 cm⁻¹ and 344 cm⁻¹ are close to the main vibrational modes of Cu₃SnS₄ reported at 318 cm⁻¹ and 348 cm⁻¹ [116]. Thus the results of the Raman spectrum reveal the formation of CZTS and the presence of SnS and CTS precursors.

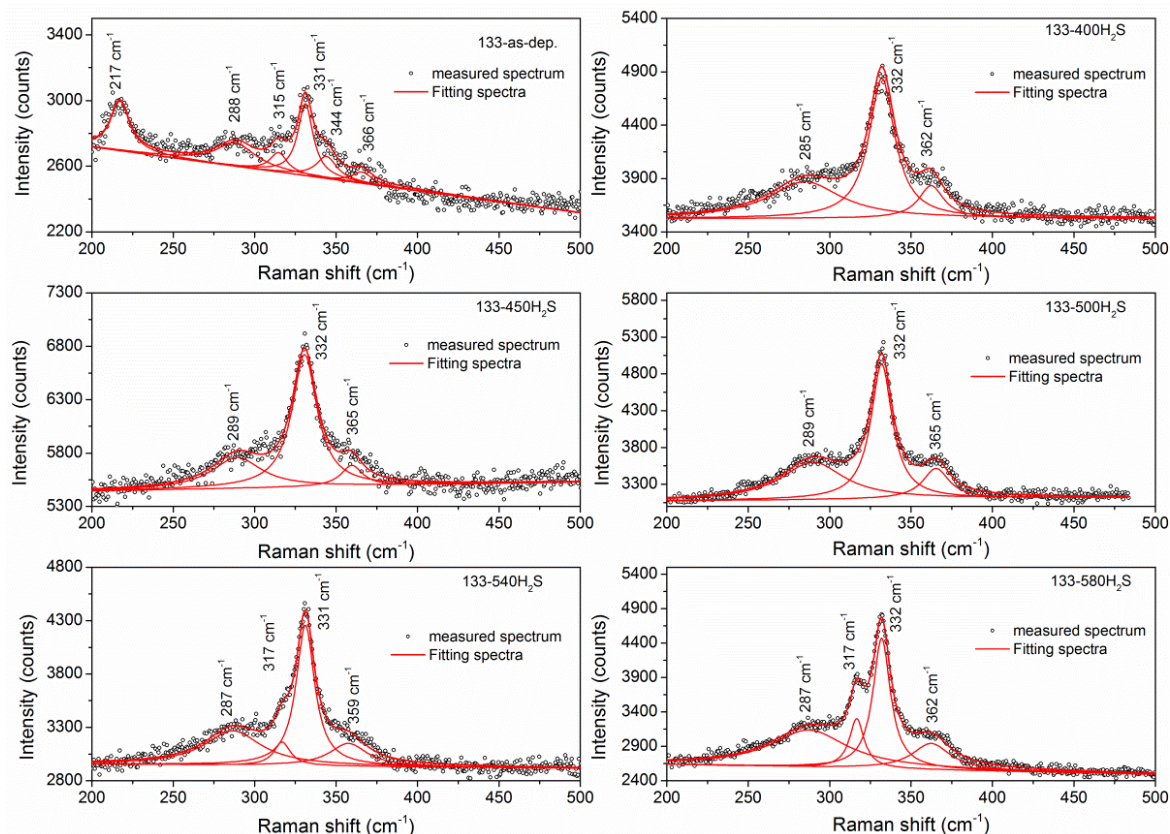


Figure 4.9 Raman spectra of as-deposited sample and samples annealed in Ar-H₂S (5 %) atmosphere at different temperatures as illustrated in the inset of the figures.

The Raman spectra of the samples annealed at between 400 °C and 580 °C (Figure 4.9) display a strong vibrational mode centered at 331 - 332 cm⁻¹. As discussed, this vibrational mode is related to the A mode for kesterite type CZTS. Two weak peaks situated at 285-289 cm⁻¹ and 359-365 cm⁻¹ corresponding to A mode and B(LO) mode of kesterite type CZTS phase are also identified by fitting the spectra with Lorentzian curves. An additional peak located at 317 cm⁻¹ was detected as a shoulder of the main vibrational mode in sample 133-540H₂S and 133-580H₂S. This peak is close to the reported mode both for CTS (318 cm⁻¹) [116] and SnS₂ (A_{1g} mode at 315 cm⁻¹) [117]. XRD results reveal that SnS₂ is present as a secondary phase in both of these samples. Therefore, this peak can be assigned to SnS₂ phase. However, the XRD patterns of CTS and CZTS are overlapping, we cannot exclude the coexistence of CTS phase. This peak becomes more visible in sample 133-580H₂S than in sample 133-540H₂S. The explanation for this could be that some of the SnS phase was

converted to SnS₂ phase with increasing annealing temperature under H₂S atmosphere. The assignments of all the peaks are summarized in Table 4.7.

Table 4.7 Frequency and proposed mode assignment of Raman peaks from samples annealed at different temperatures and atmospheres.

	mode	Raman scattering peak frequency (cm ⁻¹)									
		133-40	133-45	133-50	133-54	133-58	133-4	133-4	133-5	133-5	133-5
		0H ₂ S	0H ₂ S	0H ₂ S	0H ₂ S	0H ₂ S	00Se	50Se	00Se	40Se	80Se
CZTS/ CZTSSe	A	288	285	289	287	287	196	192	175	177	173
							211	206	201	201	196
	B/E	331	332	332	331	332	329	329	328	329	327
ZnS	LO	/	/	/	/	/	353	/	/	/	/
SnS	A _g	/	/	/	/	/	220	220	220	220	220
SnS ₂	A _{1g}	/	/	/	317	317	/	/	/	/	/
SnSe ₂	A _{1g}	/	/	/	/	/	400	400	400	400	400

Figure 4.10 shows the evolution of the FWHM of the peak at 331-322 cm⁻¹ for samples 133-400H₂S, 133-450H₂S, 133-500H₂S, 133-540H₂S, and 133-580H₂S. As it is known that the FWHM of the Raman peak is related to the crystalline quality of the samples. The increasing sharpness of the peak with increasing temperature indicates better crystal quality with increasing annealing temperature, which is in agreement with XRD results.

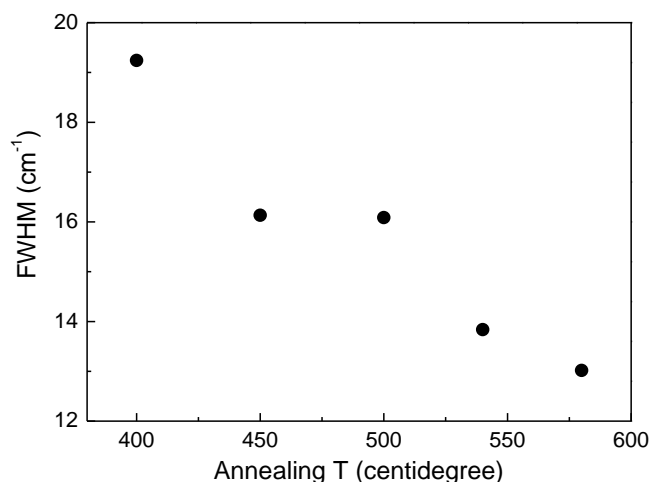


Figure 4.10 Evolution of the FWHM of the peak at $331\text{-}332\text{ cm}^{-1}$ for samples 133-400H₂S, 133-450H₂S, 133-500H₂S, 133-540H₂S, and 133-580H₂S.

Raman spectroscopy analysis of samples annealed in Ar-Se atmosphere

Figure 4.11 shows the Raman spectra of the samples annealed at different temperatures in Ar-Se ambience. Two common peaks at 220 and 400 cm^{-1} can be observed in all the spectra, which indicates that the phases corresponding to these two peaks are present in all the samples. The mode at 220 cm^{-1} can be assigned to the A_g mode of SnS phase [114]. The other mode at 400 cm^{-1} can be attributed to the A_{1g} mode of SnSe₂ phase which shows a vibration at 399 cm^{-1} as reported by Agnihotri *et al.* [118]. Although these two phases exist in all the samples, the content of these two phases is different. As shown in the figure, the signal of both phases decreases with increasing annealing temperature. Especially, significant decrease can be observed when the annealing temperature changed from 450 to $500\text{ }^\circ\text{C}$, which consists with the XRD results where the peak at $2\theta = 31.93^\circ$ corresponding to SnS phase disappeared for the sample annealed above $500\text{ }^\circ\text{C}$.

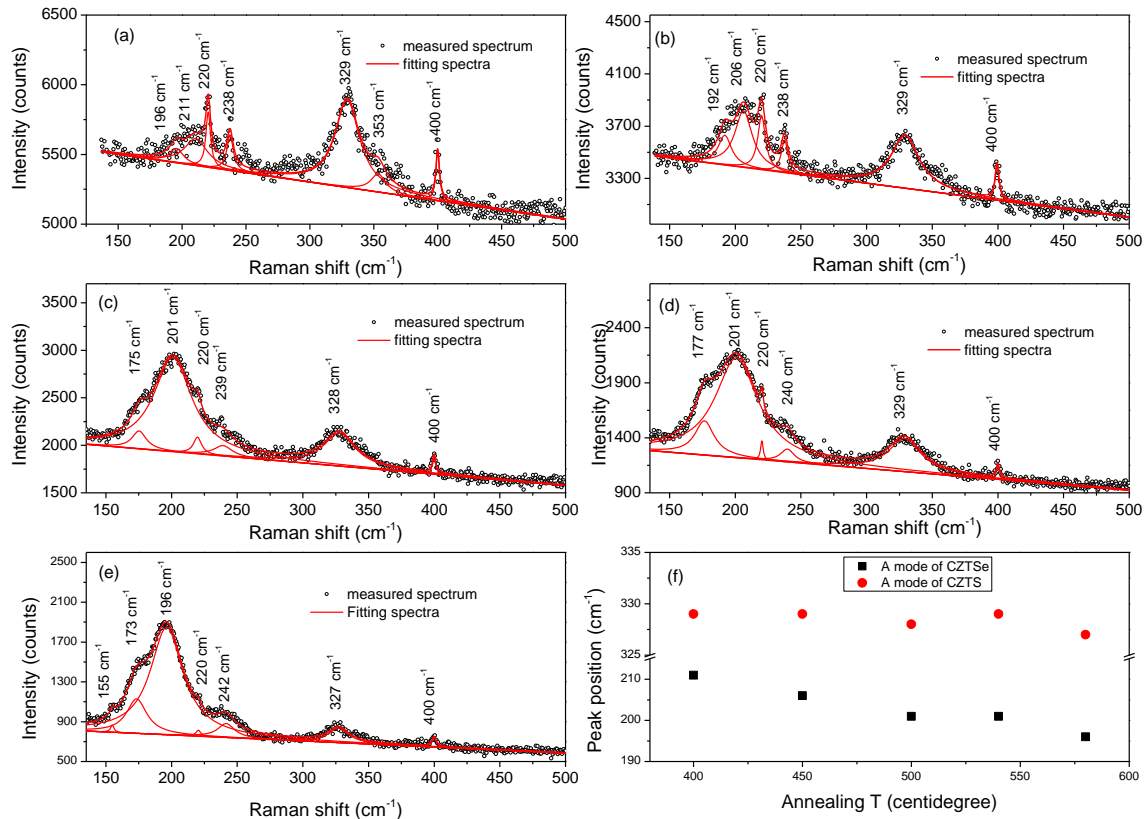


Figure 4.11 Raman spectra of samples annealed in Ar-Se atmosphere at different temperatures: (a) 133-400Se, (b) 133-450Se, (c) 133-500Se, (d) 133-540Se, and (e) 133-580Se; and (f) evolution of the A mode corresponding to CZTS and CZTSe with annealing temperature. The fitting curves fitted by using Lorentzian curve are also shown.

Another common feature for all the spectra is that, modes at 327-329 cm⁻¹ can be observed which can be identified as the main vibrational mode (A mode) of CZTS. The shift of the peak position from the 332 cm⁻¹ for the samples annealed at H₂S (see Table 4.7) atmosphere can be explained by the replacement of S with Se in CZTS. Raman peaks corresponding to the A mode of CZTSe were also detected for all the samples. Furthermore, the peak positions shifted to lower frequency with increasing annealing temperature (see figure 4.11 (f)), which is due to the increasing replacement of S with Se in the CZTSSe samples. According to equation (4.7), the value of M_{VI} contributed to this CZTSe mode decreased with increasing temperature, resulting in a shift of frequencies ν of the A mode for CZTSe towards lower frequencies. An additional peak at 353 cm⁻¹ was also detected in sample 133-400Se,

which can be ascribed to the LO mode of ZnS phase. The assignment of the Raman peaks from all the samples are summarized in Table 4.7.

4.2.2 Influence of ligand exchange on the morphology

The as-synthesized nanoparticles were capped by oleylamine which is a long chain surfactant ligand containing 18 carbon atoms. This ligand is difficult to be completely removed from the deposited thin films even after annealing at high temperature which is much higher than the boiling point of the ligand. As a result carbon may be left behind in between of the particles after annealing, which may act as a barrier for the grain growth. Nag *et al.*[119] reported that the long chain organic ligand can be replaced by the inorganic ligands such as S^{2-} , HS^- , Se^{2-} , HSe^- , Te^{2-} , HTe^- , TeS_3^{2-} , OH^- and NH_2^- . Zhang *et al.* [120] have also reported that the long chain organic ligand can be completely removed from nanoparticle films using ligand exchange strategy by dipping the thin films into $(NH_4)_2S$ methanol solution. To examine the effectiveness of this strategy in C-Z-T-S nanoparticle films, we applied this strategy to our samples.

Figure 4.12 shows the schematic of the ligand exchange process of a single nanoparticle capped by long chain organic ligand oleylamine with $(NH_4)_2S$.

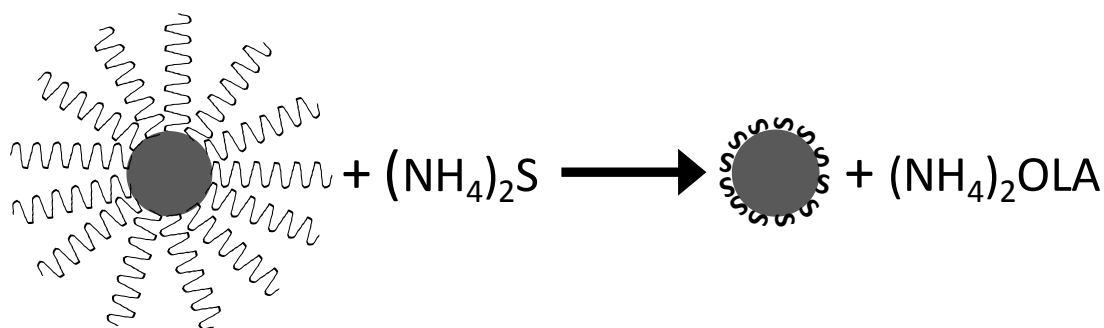


Figure 4.12 Schematic of the ligand exchange process of a single nanoparticle using $(NH_4)_2S$.

4.2.2.1 Surface morphology

Figure 4.13 (a) shows the surface SEM image of the 137-1-CZTSSe sample prepared using a sequential deposition of four layers with each layer ligand-exchange with $(NH_4)_2S$.

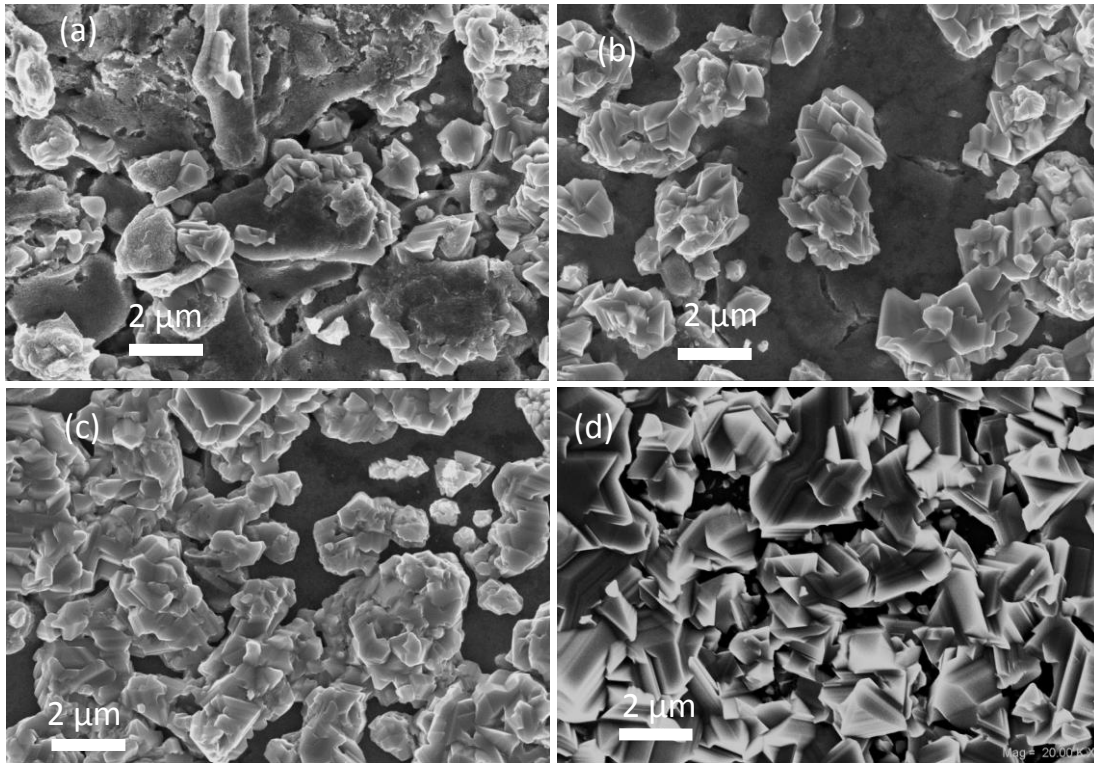


Figure 4.13 surface SEM images of CZTSSe samples prepared with different ligand exchange processes: (a) 137-1-CZTSSe deposited with ligand change for all four layers; (b) 137-2-CZTSSe deposited with ligand change for first four layers covered with one without ligand exchange; (c) 137-3-CZTSSe with ligand exchange for only the first layer; and (d) 145-CZTSSe deposited using two step annealing process.

Lots of cracks in around $1\ \mu\text{m}$ can be observed in CZTSSe thin films, which is due to reduction of interparticle spacing resulting from the replacement of the long chain organic ligand with $(\text{NH}_4)_2\text{S}$. Wang *et al.* [120] have also observed cracks in the PbS thin films after replacing the oleate ligand with $(\text{NH}_4)_2\text{S}$. To minimize the cracks, we changed the deposition procedure by combining the ligand exchange and non-ligand-exchange procedures. Figure 4.13 (b) shows surface morphology SEM image of sample 137-2-CZTSSe deposited by covering four ligand-exchanged layers with one non-ligand exchanged layer. There are still some Cracks on the surface of the samples, but the size of around $150\ \text{nm}$ is much smaller than that observed in sample 137-1-CZTSSe. Although large grain can be detected on the surface, the coverage of the grain on the surface is not complete. Figure 4.13 (c) shows better coverage of the grains on the surface for sample 137-3-CZTSSe which was prepared by covering one ligand-exchanged

layer with three non-ligand-exchanged layers. Sample 145-CZTSSe deposited using a two-step deposition and annealing processes shows the best grain coverage in all the four samples, see Figure 4.13 (d). This is because the grain island resulting from the first annealing can be coverage with new coming precursors from the second deposition and can grow again during the second annealing.

4.2.2.2 Cross sectional morphology and EDX analysis

Figure 4.14 shows the cross sectional SEM images of samples 137-3-CZTSSe and 145-CZTSSe. The CZTSSe absorbers have a thickness of $2.0 \sim 2.5 \mu\text{m}$ and $4.4 \sim 4.9 \mu\text{m}$ for sample 137-3-CZTSSe and 145-CZTSSe, respectively. The most reported thickness for CZTSSe absorbers is between 1.0 to $2.5 \mu\text{m}$ [4, 7-9, 21, 55]. The thickness of sample 137-3-CZTSSe is comparable with the most reported values while the thickness of sample 145-CZTSSe is near twice of the value reported by Mitzi *et al.*[4, 7, 21]. Sample 137-3-CZTSSe (Figure 4.14(a)) shows a double-layered structure with a large grain layer on top and a fine grain layer near the Mo substrate. Sample 145-CZTSSe (Figure 4.14 (b)) shows more complicated four-layered-structure with a large grain layer on top and another large grain layer located in between two fine grain layers.

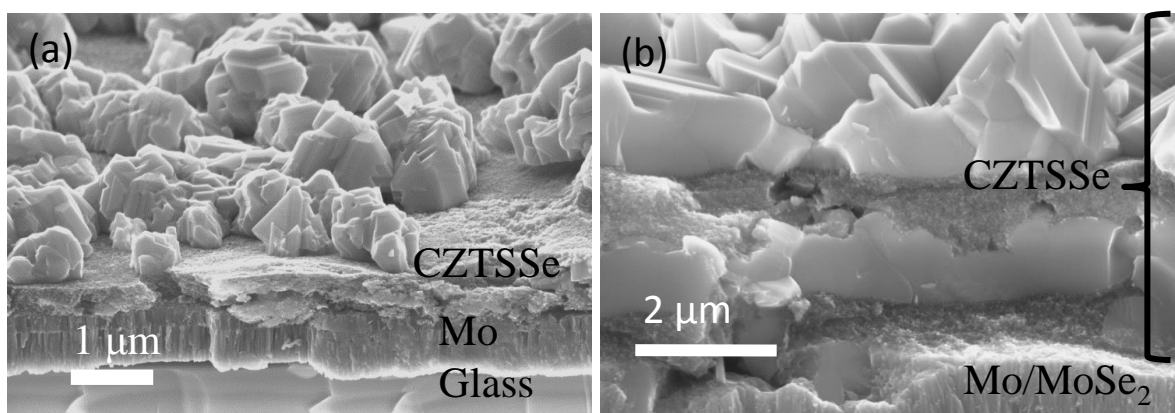


Figure 4.14 Cross sectional SEM images of samples of (a) 137-3-CZTSSe and (b) 145-CZTSSe.

To check the homogeneity of the elemental distribution through the cross section the films in terms of chemical composition, we performed EDX line scanning across the cross section of sample 137-3-CZTSSe and 145-CZTSSe. Figure 4.15 (a) shows the EDX line scanning through the cross section for sample 137-3-CZTSSe. Four regions are marked over the EDX line scanning: regions of I, II, III and IV correspond to the surface of the sample, large grain layer, fine grain layer and Mo substrate. The surface (region I) and the large grain layer (region II) show a homogeneous distribution of all the elements. However, unlike region I and II, the nanoparticle layer shows inhomogeneous distribution for all the elements. The content of C and O increased dramatically from less than 10 at.% and 5 at.% in the large grain layer (region II) to nearly 20 at.% and 15 at.% in the fine grain layer (region III), respectively. Interestingly, the content of Sn increased from around 10 at.% in the large grain layer (region II) to around 15 at.% in the fine grain layer (region III). Meanwhile the content of Cu and Zn decreased gradually through the whole fine grain layer and the concentration of Se decreased to around 20 at.% in the fine grain layer (region III) from 25 at.% in the large grain layer (region II). These results may suggest the existence of tin selenide or tin oxide compounds in the fine grain layers.

Figure 4.15 (b) shows the EDX line scanning through the cross section for sample 145-CZTSSe. Similarly, in region I (surface) and region II (large grain layer), the distribution for all the elements are homogeneous. However, in region III (fine nanoparticle layer) the ratio of C increased by around 5 at.% and the concentration of Sn increased gradually, which is accompanied by a gradual decrease of Cu. When it goes into region IV (fine grain layer near Mo), the ratio of Cu and Zn decreased significantly but both of C and O increased rapidly to around 20 at.%. The concentration of Sn firstly increased at the interface of region IV and V and then decreased rapidly. The surface of the Mo substrate became MoSe_2 as evidenced by around 60 at.% of Se and 30 at.% Mo at the surface of the substrate.

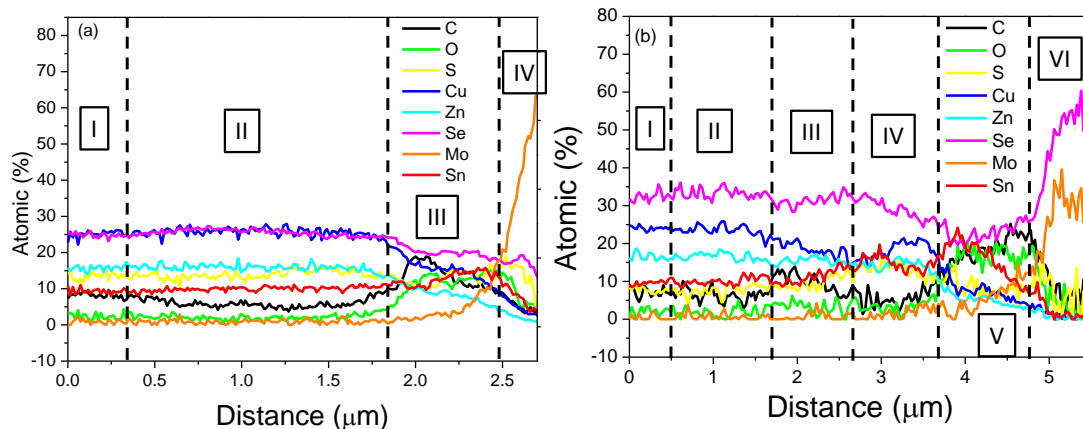


Figure 4.15 EDX line scanning profile across the cross section of the samples (a) 137-3-CZTSSe and (b) 145-CZTSSe. In sample 137-3-CZTSSe, four regions were marked: region I, II, III and IV correspond to the surface of the sample, large grain layer, fine grain layer and Mo substrate. In sample 145-CZTSSe, six regions were marked across the sample: region I is the surface of the samples, regions II and IV correspond to the large grain layers, and regions III and VI are the fine grain layers.

EDX analysis shows that carbon exists on both 137-3-CZTSSe and 145-CZTSSe samples, especially in the fine grain layer where higher concentration of C was found, indicating that the exchange of organic ligand with the inorganic ligand is not complete. The O observed in the nanoparticle layer could be from SnS precursor which contains SnO as a secondary phase or from the heat treatment processes which were carried out in air during the deposition of the precursor films. Since the elemental distribution of the precursor layers was homogeneous (see Figure A.2), the increased content of Sn in the fine grain layer near the Mo substrate should be due to the out diffusion of Cu and Zn towards the surface of the absorbers and Sn was left behind.

From the EDX analysis we can speculate that there may be three reasons responsible for formation of the layered structures in our CZTSSe absorbers. Firstly, the existence of high concentration of C in CZTSSe thin films, which acted as barriers for the growth of the particles. Secondly, the deviation of the stoichiometry from CZTSSe at the bottom layer resulting from the out diffusion of Cu and Zn towards the surface of the sample restricted the reaction of the nanoparticles to grow into large grain. The third one could be the existence of high content of oxygen in the fine grain layer.

4.3 Summary

In this chapter, $\text{Cu}_2\text{ZnSn}(\text{S}_x\text{Se}_{(1-x)})_4$ thin films have been successfully prepared by solution deposition processes using binary and ternary chalcogenide nanoparticle dispersed in hexanthiol as ink precursors. The formation temperature of CZTS by the reaction of the nanoparticle precursors was found to be as low as 350 °C. Two main deposition processes, namely non-ligand-exchange process and ligand-exchange process have been discussed.

Large grains can be observed on the surface only for sample 133-580H₂S when the precursor films were annealed in Ar-H₂S atmosphere. Grain growth started at 400 °C when the precursor films were annealed in Ar-Se atmosphere. These samples show a double-layered structure with large grain on the surface and a fine grain layer near the substrate, which is similar to most literature reports on preparation of CZTSSe or CIGS thin films from nanoparticle precursors [9, 121].

XRD and Raman spectroscopy confirmed the formation of CZTS phase for all the samples annealed at different temperatures (400, 450, 500, 540, and 580 °C) in Ar-H₂S atmosphere. In addition, secondary phases of SnS and Cu₂S existed in all the samples as confirmed by XRD. SnS₂ secondary phase was detected by both XRD and Raman spectroscopy in samples of 133-540H₂S and 133-580H₂S. On the other hand, for the samples annealed under Ar-Se atmosphere, CZTSSe phase was the dominated phase as demonstrated by both XRD and Raman spectroscopy. Secondary phases of SnS and SnSe₂ were also found in all the samples 133-400Se, 133-450Se, 133-500Se, 133-540Se, and 133-580Se. An additional secondary phase ZnS was found in sample 133-400Se, which is due to the incomplete reaction of the ZnS precursor. The values of x in $\text{Cu}_2\text{ZnSn}(\text{S}_x\text{Se}_{(1-x)})_4$ were estimated to be 0.37, 0.36, 0.31, 0.25 and 0.16 for samples 133-400Se, 133-450Se, 133-500Se, 133-540Se, and 133-580Se, respectively.

The influence of ligand-exchange with $(\text{NH}_4)_2\text{S}$ of the precursor layers on the morphology of the resulting thin films was investigated. Lots of cracks were found for thin films of 137-1-CZTSSe with ligand-exchange for all four sequential precursor layers. Cracks can be reduced by covering the ligand-exchanged precursor layer(s) with non-ligand-exchange precursor layer(s) (sample 137-2-CZTSSe and 137-3-CZTSSe). Increasing the number non-ligand-exchanged layers resulted in better coverage of large grain over the fine grain layer. A two-step annealing process led to four-layered structure CZTSSe thin films with alternation

of large grain/fine grain layer and gave a near homogeneous coverage of large grain layer over the fine grain layer. Similar to the non-ligand-exchanged thin films, layered structure were observed in the ligand-exchange CZTSSe thin films. One of the main reasons for this layered structure are the existence of high content of oxygen and carbon which serves as barrier for the growth of the nanoparticles in the fine grain layer. Another reason was found to be the out diffusion of Cu and Zn from the bottom fine grain layer resulting in a highly Sn-rich layer which deviates from the stoichiometry of CZTSSe. Therefore, optimizing of the ligand-exchanged processes, i.e. increasing the concentration of the $(\text{NH}_4)_2\text{S}$ solution, and the annealing processes are required for avoiding the layered structure.

5 Photoluminescence spectroscopy studies of $\text{Cu}_2\text{ZnSn}(\text{S}_x\text{Se}_{1-x})_4$ thin film

As a nondestructive method, photoluminescence spectroscopy has been widely used for characterization of defect properties of semiconductors. This chapter is to investigate the defect properties of the CZTSSe thin film absorbers by excitation power dependent and temperature dependent photoluminescence spectroscopy. After a brief introduction of the radiative recombination mechanisms, the dominant emissions related to defects are analyzed in the samples prepared under different conditions such as at various annealing temperature and chemical composition.

5.1 Basics of photoluminescence

Photoluminescence (PL) is the spontaneous emission of photons from a material under optical excitation with a wavelength higher than the band gap of the materials [122]. PL involves three main processes: absorption of the photons, excitation of electrons from low energy states (valence band or defect states near the valence band) to higher energy states (conduction band or defect states near conduction band) and the excited electrons relaxed back to the lower energy states called recombination by releasing photons which can be detected by a photon detector. There are many different paths involving in the optical recombination process depending on the material properties. Generally, different recombination paths can be distinguished by their transition energy and the change of the transition energy with varying measurement conditions like excitation power and temperature. Additional to the radiative recombination, nonradiative recombination may also occur through the transition of the excited electrons to the deeper defect states by releasing phonons. Figure 5.1 illustrates some possible recombination paths of the excited electrons, including band-to-band, free-to-bound, donor-acceptor pair (DAP) and nonradiative recombination processes.

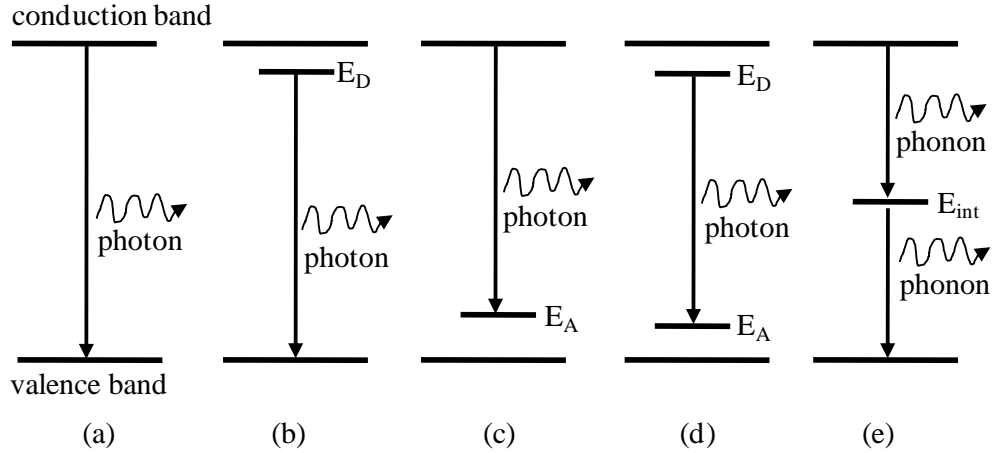


Figure 5.1 Schematic illustrations of radiative recombination paths: (a) band-to-band; (b) donor-to-valence band; (c) conduction band to acceptor; (d) donor-to-acceptor pair; and (e) nonradiative recombination via an intermediate state [122].

Band-to-band transitions (Figure 5.1 (a)) involve the recombination of free electrons and free holes [122]. The emission should have a low energy threshold where photon energy $h\nu$ (here the h is the plank constant and ν is the frequency of the light) equals to the band gap E_g . The high energy tail moves at higher energies under increasing excitation rate and increasing temperature because emission at higher energies are possible as the states deeper in the band become filled [122].

The free-to-bound recombination (Figure 5.1 (b) and (c)) involves transitions of carriers from energy bands to the defect levels (donor or acceptor impurities) in the band gap. [122] the transition line shape can be described by the following equation:

$$I = \sqrt{(\hbar\nu - E_g + E_i)/k_B T} \exp\left(-\frac{\hbar\nu - E_g + E_i}{k_B T}\right) \quad (5.1)$$

where E_i is the ionization energy of the donor (E_D) or acceptor (E_A), E_g is the band gap of the material, k_B is the Boltzmann constant and T is the sample temperature. The PL maximum $h\nu_{max}$ is given by equation 5.2.

$$h\nu_{max} = E_g - E_i \quad (5.2)$$

When both donors and acceptors exist in significant concentrations and the measuring temperature is low enough, it is possible to detect the donor-acceptor pair (DAP) recombination process (Figure 5.1 (d)). The DAP recombination can be express using the following equation:

$$h\nu_{max} = E_g - (E_A + E_D) + \frac{e^2}{4\pi\epsilon_0\epsilon r} \quad (5.3)$$

where E_D and E_A are the donor and acceptor ionization energies, respectively, r is the distance between the donor and acceptor involved in the emission, e is the electron charge, ϵ denotes the static dielectric constant, and ϵ_0 is the permittivity of vacuum. The last term of Equation (5.3) describes the coulomb interaction between the ionized donor and acceptor. With increasing excitation power, the number of photogenerated electrons and holes increases, and the average distance of the ionized donor-acceptor decreases. As a consequence, the emission line will shift towards higher energy due to the strength of the coulomb interaction, which is one of the main features for the DAP recombination.

To determine the recombination process, excitation power dependent PL measurement is essential. In general, the excitation power dependent of the PL intensity $I(h\nu)$ is proportional to P^k ,

$$I(h\nu) \sim P^k \quad (5.4)$$

where P is the excitation power of the incident light and k is a coefficient. It has been found that $k < 1$ stands for defect related transitions while $1 < k < 2$ represents for exciton transition [122, 123].

Overview of photoluminescence of $\text{Cu}_2\text{ZnSn}(\text{S}_x\text{Se}_{1-x})_4$

There are several groups using photoluminescence spectroscopy to study the defect properties of $\text{Cu}_2\text{ZnSn}(\text{S}_x\text{Se}_{1-x})_4$ samples. Different defect levels involving different recombination processes have been observed, which are summarized as followed.

Donor-acceptor pair recombination: Tanaka *et al.* [124] have determined the DAP recombination process both in sulfur-poor and stoichiometric CZTS single crystal samples. The ionization energy for the related defects in the sulfur-poor CZTS sample was estimated to be 48 meV. Two activation energies at 39 meV and 59 meV for the DAP recombination processes were also determined by the same group [125] for the stoichiometric and Cu-poor samples, respectively, prepared from the sol-gel and sulfurization processes. DAP recombination with ionization energies at 7 meV and 27 meV for donor and acceptor, respectively, has also been detected in $\text{Cu}_2\text{ZnSnSe}_4$ thin films by Luckert *et al.* [123] Additionally, Hönes *et al.* [126] have observed the narrow PL peak with a half-width of about 20 meV. They have observed DAP recombination in the CZTS sample prepared by

iodine vapour phase transport method. They found the shallow donor to be 5 ± 3 meV below the conduction band and the shallow acceptors to be 10 ± 5 meV or 30 ± 5 meV above the valence band.

Grossberg *et al.* [127] studied the photoluminescence of CZTSe monograin powders and they found the PL peak was located at 0.946 eV at 10 K which results from band-to-impurity recombination in CZTSe. They determined the ionization energy to be 69 ± 4 meV. In addition, Grossberg *et al.* [128] have found that the PL lines shift towards higher energies and they become more asymmetric with increasing sulfur content in $\text{Cu}_2\text{ZnSn}(\text{S}_x\text{Se}_{1-x})_4$ monograin samples. By analyzing the excitation power and temperature dependent PL spectra they proposed that the recombination was dominated by the band-to-impurity process (conduction-band-to-acceptor). In the CZTS polycrystalline sample, Grossberg *et al.* [129] have observed two PL peaks centered at 1.27 and 1.35 eV. The explanation for the existence of two PL peaks is the existence of both kesterite and disorder kesterite structures in the CZTS sample and the PL peak at 1.35 eV is from the kesterite type CZTS while the PL peak at 1.27 eV is arising from the disorder kesterite type CZTS. They proposed the recombination process related to these two peaks is band-to-impurity recombination with ionization energies of the acceptor level at 289 ± 7 meV and 277 ± 6 meV. They attributed these defect states to Cu_{Sn} .

Recently Levchenko *et al.* [130] have observed a similar recombination process (free-to-bound) in CZTS single crystal sample which shows one broad asymmetric peak at 1.29 eV measured at 30 K. The PL peak position does not exhibit noticeable shift with increasing excitation intensity from 10 to 740 mW/cm². The activation energy for the involving acceptor level was determined to be 140 meV and they attributed this acceptor to be Cu_{Zn} defect.

5.2 Photoluminescence measurements

Figure 5.2 shows the schematic diagram of the experimental setup for the photoluminescence measurements. The excitation source is a diode laser with a wavelength of 660 nm and a power of 60 mW. A set of neutral density filters was used for different excitation intensities measurements. The samples are mounted on the cold finger of a closed-cycle helium cryostat which allows the measurement at temperature down to 20 K.

The emission spectra were analysed by a monochromator and the signals are detected with a liquid nitrogen cooled CCD or InGaAs detector.

According to the calculation of Persson [13], the absorption coefficients of the pure sulfide CZTS at this excitation wavelength is around $5 \times 10^4 \text{ cm}^{-1}$ while absorption coefficient of CZTSSe containing selenium is larger than $5 \times 10^4 \text{ cm}^{-1}$ at room temperature. Using this coefficient, the absorption lengths of CZTS can be calculated to be 200 nm. Therefore, the PL signal in this measurement should come from the surface layer (around 200 nm deep) of the samples.

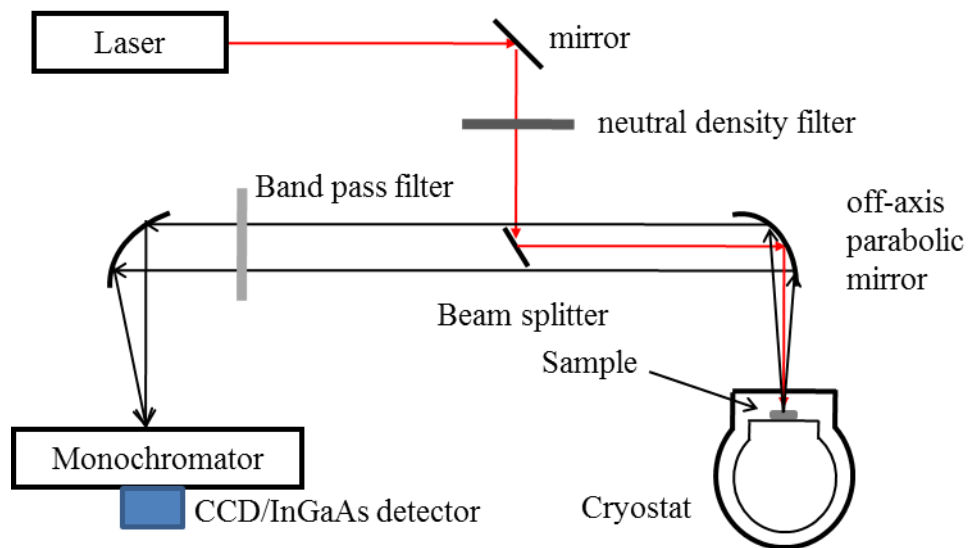


Figure 5.2 Schematic diagram of the experimental setup for photoluminescence measurements

5.3 Results and discussions

Results of the excitation intensity and temperature dependent PL spectra will be presented and discussed in this section.

5.3.1 Excitation power dependent photoluminescence analysis

Figure 5.3 shows the PL spectra of all three CZTSSe thin films measured at 20 K with 10 % of the maximum power of the diode laser. Similar to the literature reports, only broad peak was detected while the narrow excitonic line was not detected on these samples [124, 127, 131].

The peaks are located at 0.998, 1.044, and 1.180 eV for samples 145-CZTSSe, 137-3-CZTSSe, and 125-CZTSSe, respectively. These values are smaller than the band gaps of the corresponding samples, 1.15 eV for sample 145-CZTSSe, 1.28 eV for sample 137-3-CZTSSe, and 1.55 eV for sample 125-CZTSSe. The band gaps of samples 145-CZTSSe and 137-3-CZTSSe were estimated by quantum efficiency measurements (see Figure 7.4), and the band gap of sample 125-CZTSSe was determined by optical measurement [132]. According to the studies reported by the other groups [7, 111, 128, 133, 134], the band gap of CZTSSe increases with increasing sulphur content in the samples. Hence, the shift of the PL peak position is related to the chemical composition of the samples, especially the $[S] / ([S] + [Se])$ ratio which are 1.0, 0.36, and 0.28 for sample 125-CZTSSe, 137-3-CZTSSe, and 145-CZTSSe, respectively. These values were estimated from the XRD data (see Figure A.1) using the Vegard's Law (Equation (4.6)). Additionally, among these samples, sample 137-3-CZTSSe and 145-CZTSSe show similar PL intensity while sample 125-CZTSSe displays the weakest PL signal. These results indicate that the radiative recombination is more prevalent in samples 137-3-CZTSSe and 145-CZTSSe than in sample 125-CZTSSe.

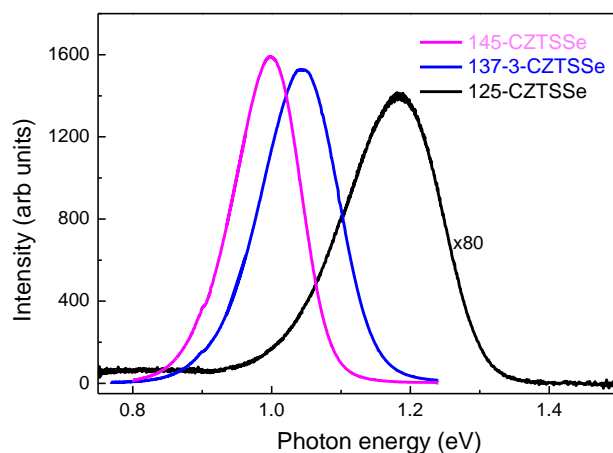


Figure 5.3 PL spectra of different samples measured at 20 K with an excitation power of 6 mW (10 % of the maximum excitation power). To get a better view on the shift of the peaks, the spectrum of sample 125-CZTSSe has been multiplied by 80.

To investigate the recombination mechanisms of these samples prepared under different conditions (see Table A.1), excitation power and temperature dependent PL measurements

were performed using the experimental setup shown in Figure 5.2. Figure 5.4 shows the PL spectra of sample 137-3-CZTSSe measured with different excitation power at 20 K. The PL intensity increases with increasing excitation intensity. However, when the excitation power exceeded 30 % of the maximum laser power of 60 mW, the PL intensity decreased with increasing excitation power. This is due to the heating effect of the laser on the sample. Similar phenomenon was also observed on samples 145-CZTSSe.

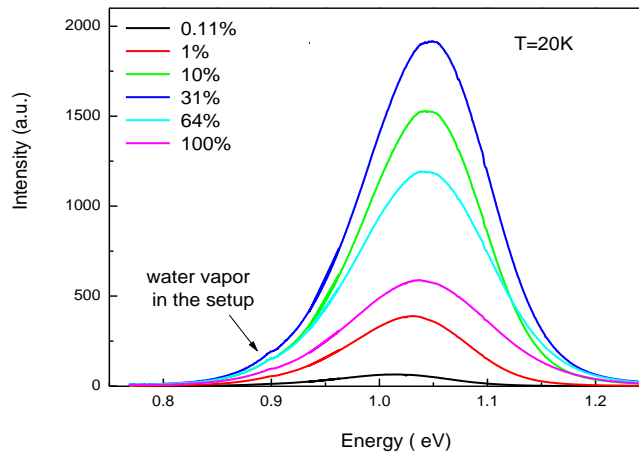


Figure 5.4 Typical evolutions of the PL spectra with increasing excitation power P for sample 137-3-CZTSSe measured at 20 K. The excitation power changed from 0.11 % to 100 % of the maximum power of the diode laser (from 0.066 mW to 60 mW).

Figure 5.5 summarizes the evolution of the PL peak positions and integrated PL intensity with increasing excitation power for all three samples. As can be seen from Figure 5.5 (a) the integrated PL intensity increased linearly with increasing excitation power before the observation of heating effect on the samples. As discussed in section 5.1, the integrated PL intensity is followed the power law, (formula (5.2)), hence we fitted the linear part of the curves using a linear fit function. The slopes are determined to be 0.86, 0.71, and 0.65 for samples 125-CZTSSe, 137-3-CZTSSe, and 145-CZTSSe, respectively. All these values are smaller than 1, indicating that the recombination mechanisms involved for all the samples are defect related [123, 131]. Figure 5.5 (b) illustrates the evolution of the PL peak positions with increasing excitation power. Sample 145-CZTSSe, which contains most content of Se, shows the lowest PL peak energies in the corresponding temperature among the three samples while

sample 125-CZTSSe containing no Se shows the largest PL peak energies. The shift of the PL peak energies with increasing excitation power are 5, 14, and 11 meV/decade for samples 125-CZTSSe, 137-3-CZTSSe, and 145-CZTSSe, respectively. These energy shifts of the PL peaks are a feature of DAP recombination process [135, 136]. Peak energies of DAP recombination can be expressed by equation (5.3). However, the shift of the PL peak energies for both sample 137-3-CZTSSe and 145-CZTSSe are larger than 10 meV / decade which might suggest that the recombination processes involved are related to the spatial potential fluctuation in the samples. Leitão *et al.* have observed that the PL peak suffers a blue shift at a rate of 23.5 meV/decade as the excitation power increases. Combining with the temperature dependent PL measurements and electronic characteriyation they suggested that this behavior can be explained by the potential fluctuation model.

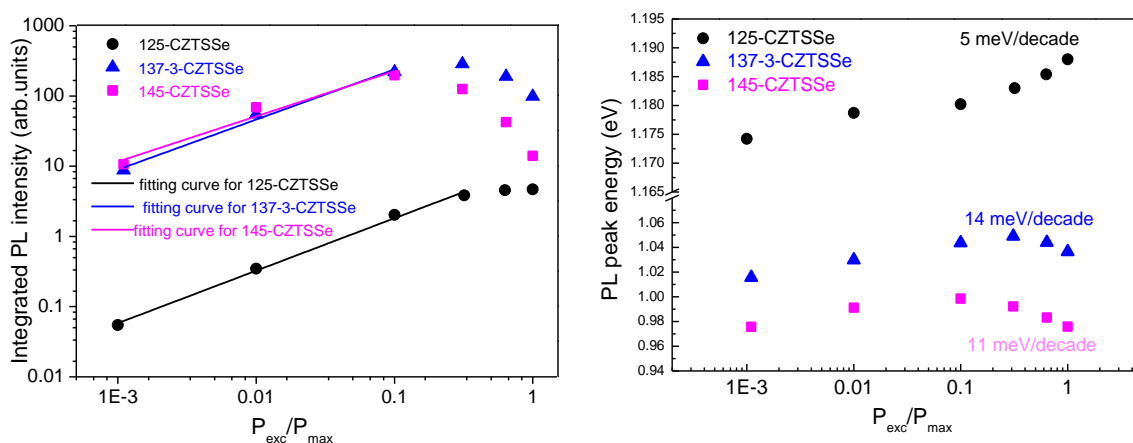


Figure 5.5 Evolutions of (a) integrated PL intensities and (b) PL peak positions with increasing excitation power P for all three samples.

5.3.2 Temperature dependent photoluminescence analysis

To further understand the recombination process, temperature dependent PL measurements were carried out down to 20 K using a laser power of 6 mW. Figure 5.6 (a) illustrates the PL spectra as a function of the temperature. As the measured temperature increases, the PL signal decreases rapidly because of the increase of the active nonradiative channels which act as the dominate recombination process at higher temperature. Particularly the PL signal is too small to be detected above 250 K for this sample. The same behavior is also observed for sample 145-CZTSSe. Contartly, the decline of the PL signal for sample

125-CZTSSe is not as fast as the other two samples. The PL signal can even be detected at room temperature. These results indicate that the dominated recombination process for samples 137-3-CZTSSe and 145-CZTSSe at the temperature above 250 K is nonradiative recombination.

Additional to the decrease of the PL signal, the PL peak energies shift as well with increasing temperatures. Detail evolution of the PL peak energies versus temperatures for all three samples can be found in Figure 5.6 (b).

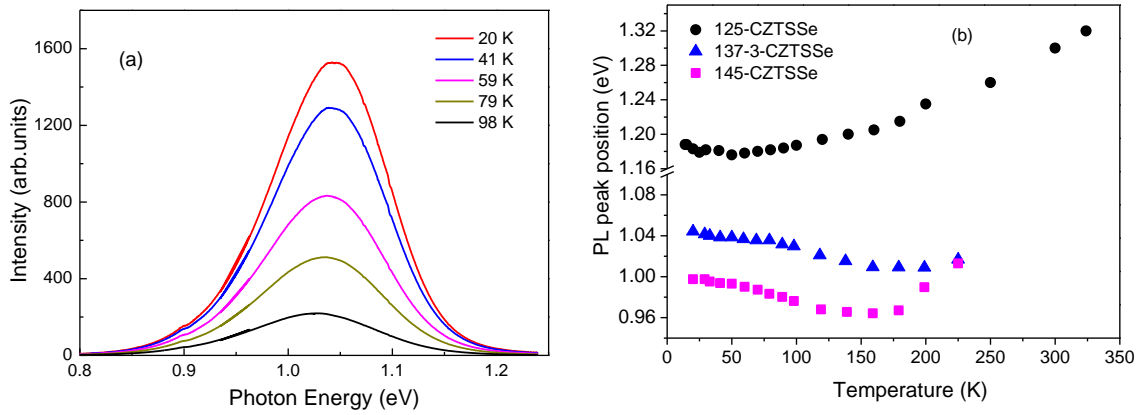


Figure 5.6 (a) Typical evolutions of the PL spectra with varied temperatures for sample 137-3-CZTSSe measured with an excitation power of 6 mW; (b) the PL peak position as a function of samples temperatures for all three samples.

Figure 5.7 shows the logarithm integrated PL intensity versus the inverse temperature. The integrated PL intensities for samples 137-3-CZTSSe and 145-CZTSSe suffer around 4 orders of magnitude quenching above 50 K while sample 125-CZTSSe shows slower quenching compared with samples 137-3-CZTSSe and 145-CZTSSe. These results may suggest that deeper defect levels may be involved in the recombination process in samples 137-3-CZTSSe and 145-CZTSSe. To find out the activation energies involved in the recombination process, two models were used for different samples. An one-activation-energy model, equation (5.5), is used for sample 125-CZTSSe and a two activation energies model, equation (5.6), is used for samples 137-3-CZTSSe and 145-CZTSSe to fit the Arrhenius plot [131, 137].

$$I(T) = \frac{I_0}{1 + C_1 T^3 + C_2 T^3 \exp\left(-\frac{E_{a1}}{kT}\right)} \quad (5.5)$$

$$I(T) = \frac{I_0}{1 + C_1 \exp\left(-\frac{E_{a1}}{kT}\right) + C_2 \exp\left(-\frac{E_{a2}}{kT}\right)} \quad (5.6)$$

where I_0 is the intensity extrapolated to $T = 0$ K, k is the Boltzmann constant, C_1 and C_2 are the process rate parameters, E_{a1} and E_{a2} are the thermal activation energies for the involving defect states. All the fitting parameters are listed in table 5.1.

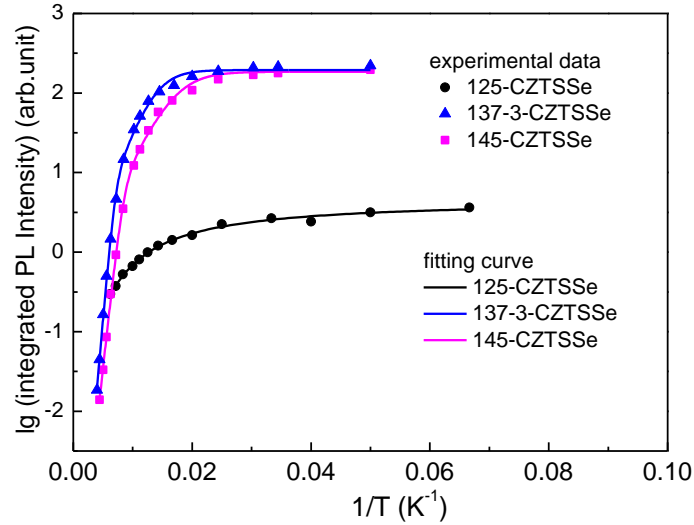


Figure 5.7 Dependence of the integrated PL intensity on temperature using 10 % of the maximum excitation power.

Table 5.1 Fitting parameters of equation (5.3) and (5.4) to the dependence on temperature of the integrated PL intensity for samples of 125-CZTSSe, 137-3-CZTSSe, and 145-CZTSSe.

	I_0	C_1	C_2	E_{a1} (meV)	E_{a2} (meV)
125-CZTSSe	4.3 ± 0.4	$4.1 \times 10^{-3} \pm 9.0 \times 10^{-4}$	$1.1 \times 10^{-2} \pm 7.3 \times 10^{-3}$	20 ± 10	/
137-3-CZTSSe	194.4 ± 11.5	433.2 ± 203.3	$2.7 \times 10^7 \pm 1.1 \times 10^7$	38 ± 4	171 ± 10
145-CZTSSe	185.0 ± 12.7	371.1 ± 68.9	$1.4 \times 10^7 \pm 4.9 \times 10^6$	30 ± 3	136 ± 10

The activation energy for the DAP recombination process in the pure sulfide sample 125-CZTSSe is found to be 20 ± 10 meV, which is close to the value of 39 meV for the DAP recombination in stoichiometry CZTS reported by Miyamoto *et al.*[125]. According to the theoretical calculation reported by Chen *et al.* [133, 138], the acceptor defect level of V_{Cu} is

20 meV above the valence band and the formation energy of this defect is quite low, particularly in the Cu-poor sample. Therefore, the defect level with activation energy at 20 ± 10 meV in sample 125-CZTSSe could be related to the V_{Cu} .

Fitting the Arrhenius plot using one activation energy model (Equation (5.5)) for samples 137-3-CZTSSe and 145-CZTSSe cannot give the best fit at the lower temperature part. Therefore, we used a two activation energy model (Equation (5.6)) to fit the curves. As shown in Figure 5.7, the two activation energy model fits quite well to the Arrhenius plots for samples 137-3-CZTSSe and 145-CZTSSe, yielding two activation energies of 38 ± 4 meV and 171 ± 10 meV for sample 137-3-CZTSSe and 30 ± 3 meV and 136 ± 10 meV for sample 145-CZTSSe. There are a lot of possible donor defects such as $(Zn_{Cu})^+$, $V_{S/Se}^{2+}$, Cu_i^+ , Zn_i^+ and Sn_{Cu}^{3+} and acceptor defects such as Cu_{Zn}^- , V_{Cu}^- , V_{Zn}^- and V_{Sn}^- in the CZTSSe compounds. According to the theoretical calculation by Chen *et al.* [133, 138], the donor levels below 200 meV in pure sulfide CZTS include $(Zn_{Cu})^+$ (150 meV), Cu_i^+ (110 meV), and Sn_{Cu} (30 meV) while the acceptor levels below 200 meV include Cu_{Zn}^- (150 meV), and V_{Cu}^- (20 meV). All these defects show lower levels in pure selenide CZTSe sample due to the weaker hybridization effect [133, 138]. Hence, the activation energies at 38 ± 4 for sample 137-3-CZTSSe and 30 ± 3 meV for sample 145-CZTSSe can be attributed to either the donor of Sn_{Cu}^{3+} or the acceptor of V_{Cu}^- while the high activation energies of 171 ± 10 meV for 137-3-CZTSSe and 136 ± 10 meV for 145-CZTSSe can be associated to donor levels of $(Zn_{Cu})^+$, or Cu_i^+ or acceptor level of Cu_{Zn}^- . However, the EDX analysis (Figure 4.15) shows that both of the samples are Cu poor and Zn rich. Therefore, we propose that the donor and acceptor pairs should be $(Zn_{Cu})^+/V_{Cu}^-$ in both of 137-3-CZTSSe and 145-CZTSSe, which is also in accordance with theoretical calculations [133, 138].

5.4 Summary

In this chapter, photoluminescence properties of $Cu_2ZnSn(S_xSe_{1-x})_4$ thin films prepared from different processing conditions have been investigated by temperature and excitation power dependent measurements. The PL peaks moved toward lower energy with increasing selenium content in CZTSSe. The PL spectra first moved toward lower energy and then move to higher energy with increasing temperature. With increasing excitation power, the PL spectra shifted to higher energy before suffering heating effect from the incident laser. The features of

the PL spectra could be attributed to DAP recombination which seems to dominate radioactive recombination process. The activation energy for the DAP recombination process was estimated to be 20 ± 10 meV for sample 125-CZTSSe, which could be related to V_{Cu} . A model with two activation energies gave the best fit for samples 137-3-CZTSSe and 145-CZTSSe, yielding activation energies of 38 ± 4 meV and 171 ± 10 meV for sample 137-3-CZTSSe and 30 ± 3 and 136 ± 10 meV for sample 145-CZTSSe. The defect levels for samples 125-CZTSSe is not clear yet while the defect levels for samples 137-3-CZTSSe and 145-CZTSSe can be associated to $(Zn_{Cu})^+ / V_{Cu}^-$ donor and acceptor pair. It should be pointed out that potential fluctuation may exist in the samples of 137-3-CZTSSe and 145-CZTSSe due to the high decreasing rate of over 10 meV/decade with increasing excitation power. For detail analysis of these behaviors, further electronic characterization is necessary.

6 Surface photovoltage analysis of $\text{Cu}_2\text{ZnSn}(\text{S}_x\text{Se}_{1-x})_4$ thin films

In order to fabricate high performance CZTSSe-based solar cells, it is crucial to prepare thin film absorbers with pure phase, controlled compositions and good crystal quality. For this purpose technological windows have to be known for each deposition technique. This demands fast characterization methods giving reliable information about photo-active phases without the need for manufacturing complete solar cells which include charge-selective and ohmic contacts.

In this chapter, modulated surface photovoltage (SPV) measurements are applied to characterize the CZTSSe thin film absorbers prepared by a solution process using ZnS, SnS and Cu_3SnS_4 as precursors. This chapter starts with a brief introduction on SPV followed by the SPV analysis of CZTSSe samples. This chapter has already been published [139].

6.1 Basics of surface photovoltage

As a contactless and nondestructive method, the SPV method has been widely used to characterize the electronic properties of semiconductors since early 1970s [140]. SPV measurements can provide information about the band structure, parameters of photo-generated charge carriers and about defects below the band gap.

In this subchapter, a brief introduction on the SPV will be presented. A more comprehensive introduction on SPV can be found in [10, 11].

In a semiconductor material, there are surface localized electronic states within the semiconductor band gap and/or a double layer of charge, known as surface dipole [10]. The appearance of these states induces charge transfer between bulk and surface in order to establish thermal equilibrium between the two. Hence, the free charge carrier density near the surface deviates from its equilibrium value in the bulk, which results in a space charge region (SCR) in the surface. Even under equilibrium condition the surface potential is different from the electric potential far away in the bulk.

SPV is based on the light-induced change of the work function at the surface of a semiconductor layer. Separation of charge carriers (electrons or holes) towards the surface of a

layer causes a change in the surface dipole and therefore a change in the work function. Figure 6.1 shows an example of the evolution of the band diagram of a p-type semiconductor under dark and illumination. Under illumination, charge separation occurs through the photo-generated electrons moving toward the surface while the hole moving to the bulk due to the built-in potential in the SCR. The redistribution of the charge carriers results in the change of the work function of the semiconductor in the surface. The difference of the work function before and after illumination represents the SPV, as shown in Figure 6.1.

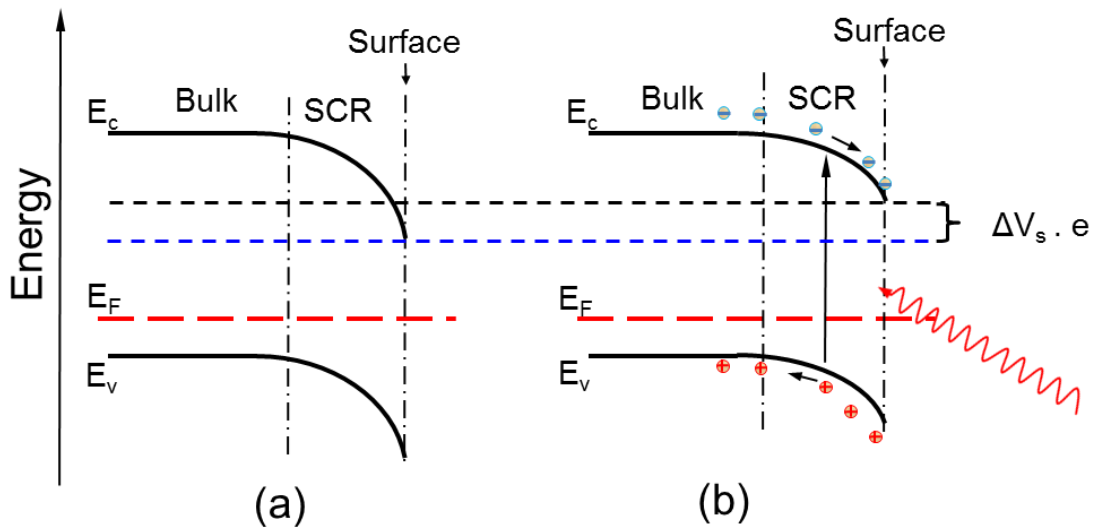


Figure 6.1 Schematic band diagrams of the surface space charge region of a depleted p-type semiconductor structure (a) under dark, and (b) under illumination. The SPV is the change of the work function resulting from the band bending under illumination.

The SPV signal depends on the amount of charge (Q) separated in the sample, on the charge separation length defined as the distance between the centers of the negative and positive charge carriers, and on the dielectric constant $\epsilon\epsilon_0$ where ϵ is the relative dielectric constant of the sample and ϵ_0 is the dielectric constant of the vacuum with a value of 8.85×10^{-14} F/cm [141]. The relationship among these parameters and SPV signal can be expressed by equation 6.1.

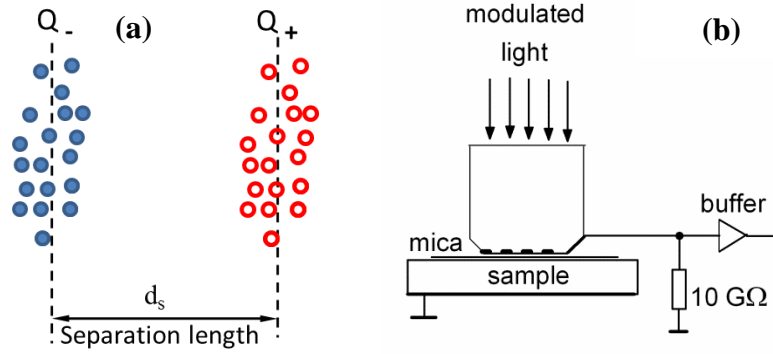


Figure 6.2 (a) Schematic representation of the charge separation in the picture of the parallel plate of capacitor; (b) schematic diagram of SPV measurement in the capacitor arrangement [141].

$$SPV = Q \frac{1}{\epsilon \epsilon_0} d_s \quad (6.1)$$

where Q is obtained by integration of the photo generated charge carriers of the same sign over the thickness of the investigated layers; d_s is the charge carrier separation length; ϵ is the relative dielectric constant and $\epsilon_0 = 8.85 \times 10^{-14} \text{ F/cm}^{-1}$.

In general, there are two main operational modes for the measurement of SPV, namely Kelvin probe and metal-insulator-semiconductor (MIS) structure.[10] In Kelvin probe arrangement, the contact potential measured between the sample and a vibrating metal electrode in dark and under steady light illumination. The difference of the contact potential under dark and under illumination represents the SPV. Figure 6.2 (b) shows the schematic diagram of the MIS structure where the sample and the fixed semitransparent electrode are separated with an insulator forming a capacitor. The sample is illuminated with modulated light which passes through the semitransparent electrode and illuminates on the sample. In our case, the measurements were performed in the MIS structure.

Determination of minority charge carriers' diffusion length

According to the Goodman [142], the diffusion length of minority charge carriers can be determined using modulated SPV measurements. The measurement is based on the following theory. The SPV signal is a function the excess minority charge carrier density Δn injected into the space charge region (SCR). The density of Δn in turn depends on the light intensity $I(\lambda)$, the optical absorption coefficient α , and the diffusion length of minority charge carriers, which can be expressed by:

$$\Delta V_s = f(\Delta n) = f\left(\frac{QE(\lambda) \cdot I(\lambda) \cdot (1-R(\lambda))}{\frac{D}{L} + s} \cdot \frac{\alpha(\lambda) \cdot L}{1 + \alpha(\lambda) \cdot L}\right) \quad (6.2)$$

where QE represents quantum efficiency for electron-hole pair creation, R is the optical reflection coefficient at the illuminated surface, D is the diffusion coefficient, s is the surface recombination velocity, and λ is the wavelength of the incident light. This equation is based on the following assumption:

$$L, \alpha^{-1} \gg W \quad (6.3)$$

$$L, \alpha^{-1} \ll H \quad (6.4)$$

$$\Delta n \ll p_0 \quad (6.5)$$

where α^{-1} , W , H , and p_0 are the optical absorption length, width of SCR, thickness of the sample, and majority charge carrier density, respectively.

If quantum efficiency QE and reflectivity R are constant over the α^{-1} region of interest, Equations (6.2) can be rewritten as

$$\Delta V_s = f\left(c_1 \cdot \frac{I(\lambda) \cdot \alpha(\lambda)}{1 + \alpha(\lambda) \cdot L}\right) \quad (6.6)$$

where c_1 is a constant. Although the specific form of this relationship may not be known, it is a monotonic function and may be inverted to provide

$$\frac{I(\lambda) \cdot \alpha(\lambda)}{1 + \alpha(\lambda) \cdot L} = F(\Delta V_s) \quad (6.7)$$

By keeping SPV signal constant, one can get

$$I(\lambda) = c_2(\alpha(\lambda)^{-1} + L) \quad (6.8)$$

Therefore, if we know the optical absorption coefficient α of the material then we can get the diffusion length L by keeping the SPV signal ΔV_s constant while recording the light intensity.

6.2 Surface photovoltage measurements

Modulated SPV measurements were performed in the fixed capacitor arrangement at a modulation frequency of 8 Hz, as shown in Figure 6.2. A halogen lamp with a quartz prism monochromator served as light source. The samples were illuminated through the FTO (SnO₂:F) electrode deposited on a quartz cylinder and a mica spacer. The SPV signals were detected with a double phase lock-in amplifier. The phase was calibrated with a silicon photodiode.

Figure 6.3 illustrates the experimental setup for determination of the diffusion length of minority charge carriers. The measurements were fulfilled by keeping the SPV signal constant while changing the light intensity. The setup contains two lock-in systems: one is for SPV signal while the other one is for recording the light intensity. The diffusion length of the minority charge carriers was measured by keeping the SPV signal constant while changing the light intensity. The light intensity was measured with a pyro-electric detector connected with a preamplifier.

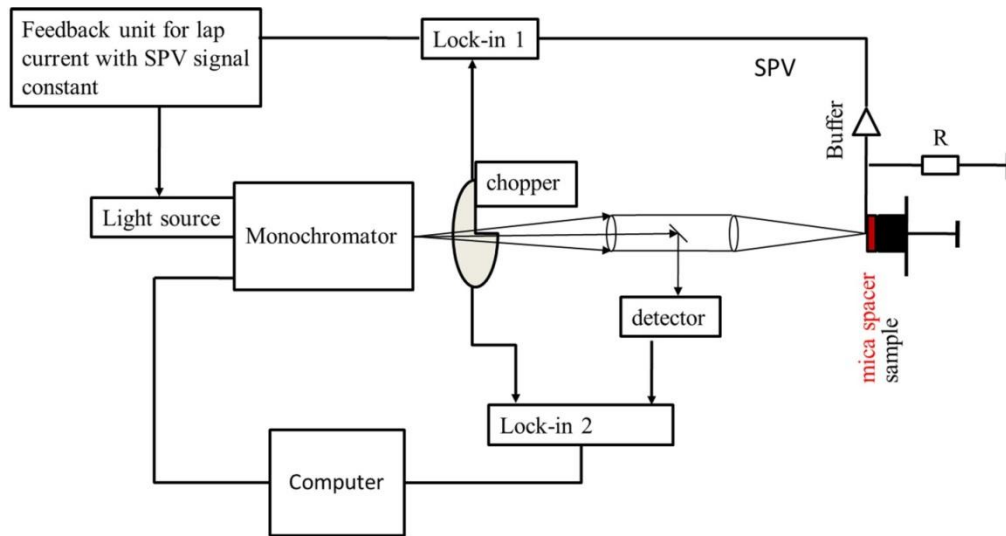


Figure 6.3 Experimental setup of SPV measurements for the determination of minority charge carrier's diffusion length. The buffer is high impedance (around $10^{12} \Omega$). The $\text{Cu}_2\text{ZnSn}(\text{S}_x\text{Se}_{1-x})_4$ with $0 \leq x \leq 1$ thin films are on Mo coated soda lime glass substrates.

6.3 Results and discussions

The detailed preparation information of this series of CZTSSe thin films can be found in Table A.1. The value of x in $\text{Cu}_2\text{ZnSn}(\text{S}_x\text{Se}_{1-x})_4$ thin films were determined to be 1, 0.79, 0.67, 0.36 and 0.28 for samples 125-CZTSSe, 137-4-CZTSSe, 137-5-CZTSSe, 137-3-CZTSSe, and 145-CZTSSe, respectively, from the XRD data (see Figure A. 1) according to the Vegard's Law (Equation 4.6).

The SPV signals were very low for the bare sample 125-CZTSSe ($x=1$) and it was practically impossible to increase the SPV signals during numerous annealing experiments in H_2S containing atmosphere. SPV signals of sample 125-CZTSSe ($x=1$) increased after

depositing a CdS surface layer which served as a passivation layer for the CZTS absorbers to reduce the surface recombination. Therefore sample 125-CZTSSe ($x=1$) was tested with a CdS surface layer which was deposited in a chemical bath [143] (Figure 6.4). The in-phase SPV signals were positive at photon energies below 1.5 eV. The strong decrease of the in-phase SPV signal towards negative values at 1.44 eV corresponds to the onset of strong absorption in $\text{Cu}_2\text{ZnSnS}_4$, i.e. to the band gap of $\text{Cu}_2\text{ZnSnS}_4$. The strong increase of the in-phase SPV signal towards positive values at 2.4 eV corresponds to the band gap of CdS.

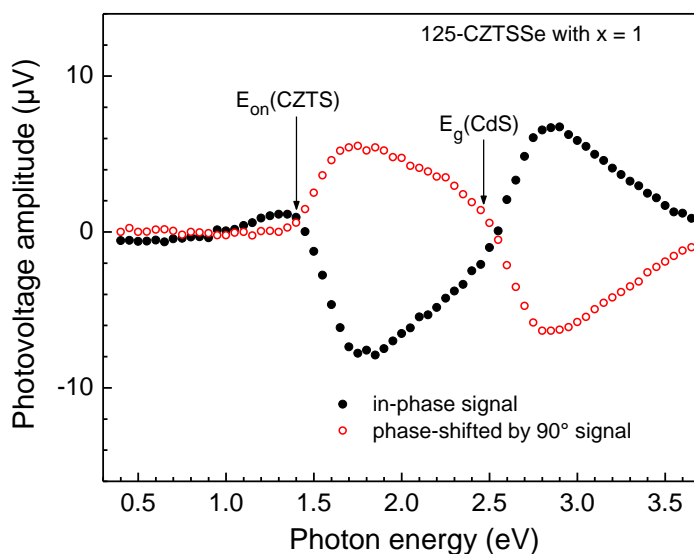


Figure 6.4 Spectra of the in-phase and phase-shifted surface photovoltage signals (filled and open circles, respectively) of sample 125-CZTSSe ($x=1$) covered with a CdS surface layer.

By changing the preparation conditions (precursor composition, deposition procedure and annealing conditions, details please go to Table 6.1, the SPV signals varied significantly. However, the in-phase signals for all these four samples are negative due to the electron move towards the surface, suggesting that the samples are p-type. The spectra of the absolute in-phase SPV signals are given in Figure 6.5 (a) for samples with $x=0.28$, 0.36 , 0.67 and 0.79 (145-CZTSSe, 137-3-CZTSSe, 137-5-CZTSSe, and 137-4-CZTSSe, respectively). The SPV signals increased strongly with increasing selenium content in the spectral range between 1 and about 1.7 eV while the lowest SPV signal was obtained for sample 137-5-CZTSSe ($x=0.67$). Further there was a qualitative change of the SPV spectra between samples 137-5-CZTSSe ($x=0.67$) and 137-3-CZTSSe ($x=0.36$). Regarding to XRD measurements the qualitative change

can be attributed to the co-existence of phases for sample 137-5-CZTSSe ($x = 0.67$). The phase-shifted by 90° spectrum is shown for the sample 145-CZTSSe with $x = 0.28$.

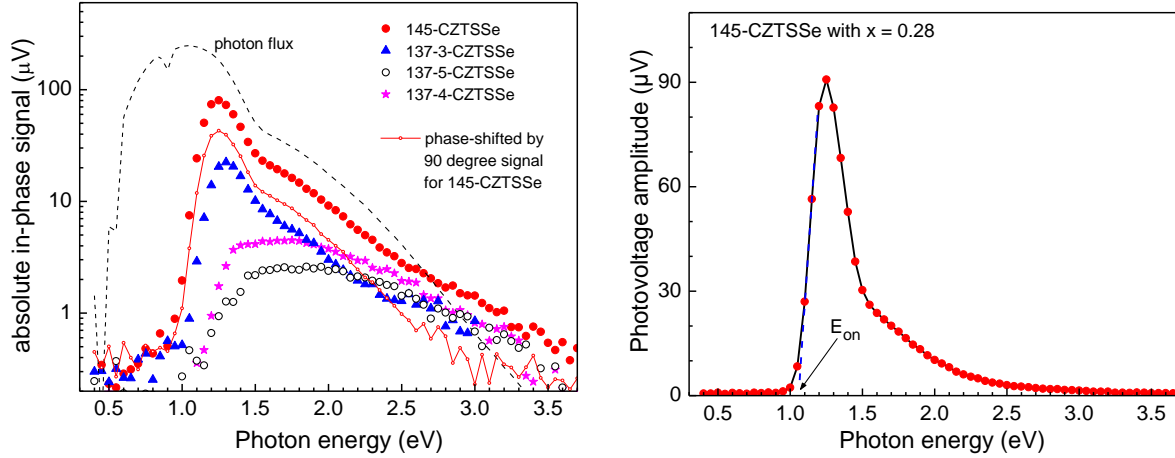


Figure 6.5(a) Spectra of the absolute in-phase surface photovoltage for samples 145-CZTSSe ($x = 0.28$), 137-3-CZTSSe ($x = 0.36$), 137-5-CZTSSe ($x = 0.67$) and 137-4-CZTSSe ($x = 0.79$) (filled circles, filled triangles, open circles, stars, respectively). The photon flux spectrum as well as the signal phase-shifted by 90° for sample 145-CZTSSe ($x = 0.28$) is shown for comparison; (b) Spectrum of the surface photovoltage amplitude for the sample 145-CZTSSe ($x = 0.28$).

Figure 6.5 (b) shows the spectrum of the SPV amplitude for sample 145-CZTSSe ($x = 0.28$). The band gap of the $\text{Cu}_2\text{ZnSn}(\text{S}_{0.28}\text{Se}_{0.72})_4$ layer can be obtained as the onset energy of the SPV signal and amounts to $E_{\text{on}} = 1.054$ eV. Below E_{on} the SPV signals are caused by transitions from defect states in the forbidden band gap. The onset energies for the other samples of 137-4-CZTSSe, 137-5-CZTSSe, and 137-3-CZTSSe, determined by the same method, are 1.173, 1.14, and 1.105 eV, respectively.

The values of E_{on} are correlated with x in Figure 6.6. The values of E_{on} increased with increasing x while the increase of E_{on} from sample 137-4-CZTSSe ($x = 0.79$) to sample 125-CZTSSe ($x = 1$) was rather steep. Values of E_{g} from literatures [20, 98, 111, 144, 145] are shown for comparison in Figure 6.6. All values of E_{on} and E_{g} correlated well with x up to about 0.4 (region I in figure 6.6). The values of E_{on} and E_{g} scattered over a wide range for x larger than 0.5 and lower than 1.0 (region II in figure 6.6). The values of E_{on} and E_{g} obtained by

electro reflectance of samples with $x= 1.0$ were very similar but underestimated in comparison to E_g measured by pure optical methods (region III in Figure 6.6).

The onset energies measured by SPV seem to be greatly underestimated for samples 137-4-CZTSSe ($x= 0.79$) and 137-5-CZTSSe ($x= 0.67$) in relation to E_g deduced from optical measurements. Comparing the optical measurements of the band gap by He *et al.* [111] and the onset energies measured by SPV one would expect for samples 137-4-CZTSSe and 137-5-CZTSSe much lower values for x (between 0.4 and 0.5). SPV measurements are only sensitive to the part of the sample in which charge separation becomes efficient whereas optical and XRD measurements probe the whole sample volume. Therefore it can be concluded that efficient charge separation in $\text{Cu}_2\text{ZnSnSe}_4$ is only possible in a phase in which the amount of selenium is larger than the amount of sulfur.

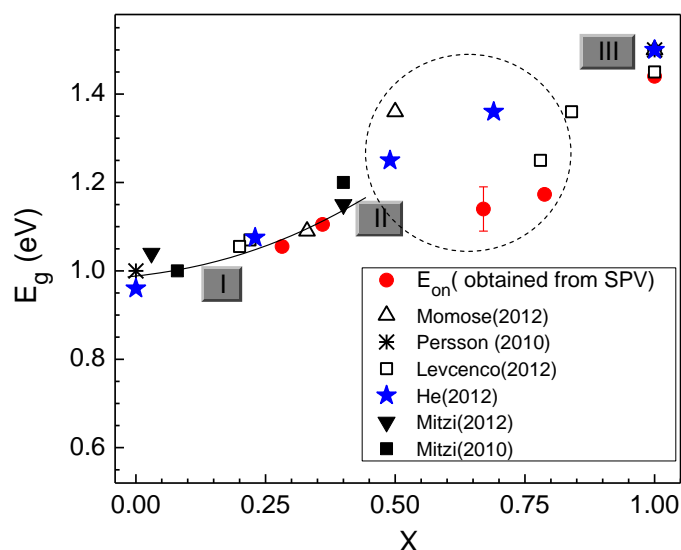


Figure 6.6 Dependence of the band gap on the stoichiometry of $\text{Cu}_2\text{ZnSn}(\text{S}_x\text{Se}_{1-x})_4$ for samples used in this work and for values from the literature. I, II, and III mark regions of different degree of correlation.

Determination of the diffusion length of sample 145-CZTSSe

The diffusion length of minority charge carriers, i.e. of electrons in $\text{Cu}_2\text{ZnSn}(\text{S}_x\text{Se}_{1-x})_4$ layers (L_e), can be obtained from SPV measurements by keeping the SPV signal constant and measuring the light intensity as a function of the reciprocal absorption coefficient (α^{-1}) [142]. The relationship between the light intensity and the absorption coefficient can be express by

equation (6.8). Here, the measurements were performed on sample 145-CZTSSe ($\text{Cu}_2\text{ZnSn}(\text{S}_x\text{Se}_{1-x})_4$ with $x=0.28$) which shows the strongest SPV signal among all the samples investigated. Another important parameter that should be known for getting information about L_e is absorption spectrum. The absorption spectra of prepared $\text{Cu}_2\text{ZnSn}(\text{S}_x\text{Se}_{1-x})_4$ layers cannot be well measured due to uncertainties in phase composition (as discussed in chapter 4 the samples prepared in this approach normally contain double layers or even multiple layers.). Therefore, in this case, for the SPV analysis the absorption coefficients were obtained from the absorption spectrum of $\text{Cu}_2\text{ZnSnSe}_4$ [13] shifted to the band gap of 1.054 eV.

Figure 6.7 displays the dependence of the light intensity on the absorption length for sample 145-CZTSSe ($\text{Cu}_2\text{ZnSn}(\text{S}_x\text{Se}_{1-x})_4$ with $x=0.28$). At larger values of α^{-1} the intensity increases practically linearly with increasing α^{-1} what gives evidence for diffusion limited transport. According to Equation 6.7, the diffusion length corresponds to the negative value of the interception point at zero intensity [144]. It can be seen that L_e is about 1.2 μm for the $\text{Cu}_2\text{ZnSn}(\text{S}_x\text{Se}_{1-x})_4$ layer with $x=0.28$. On the other side the intensity increases strongly with decreasing α^{-1} at low values of α^{-1} which could be due to the high surface recombination.

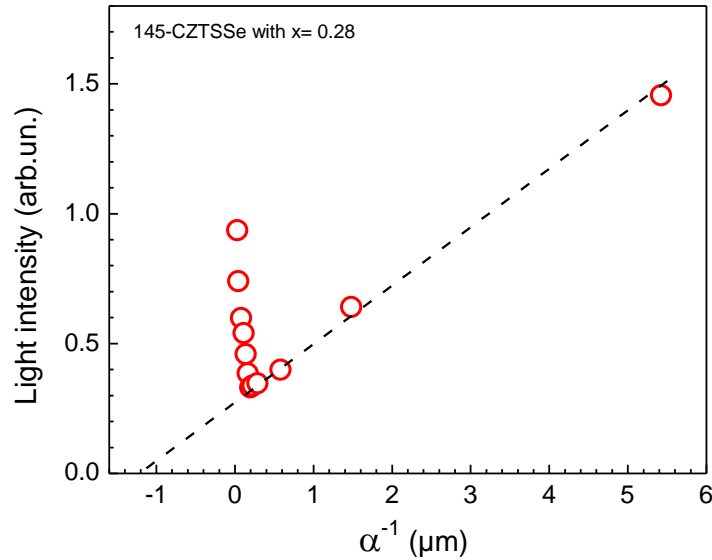


Figure 6.7 Dependence of the light intensity (measured with a pyro-detector) on the absorption length obtained from [13] for sample 145-CZTSSe ($x=0.28$).

Temperature dependent SPV analysis on sample 145-CZTSSe

To understand charge carriers recombination processes in CZTSSe samples, temperature dependent SPV measurements were performed on sample 145-CZTSSe with $x = 0.28$. The measurements were carried out between 93 and 398 K in the photon energy range of 0.9 to 1.3 eV. Figure 6.8 (a) shows the representative temperature dependent absolute in-phase SPV spectra. The decrease of the sample temperature leads to the increase of the absolute in-phase SPV signals. This is due to the decrease of the density of defect states which act as recombination center of the carriers.

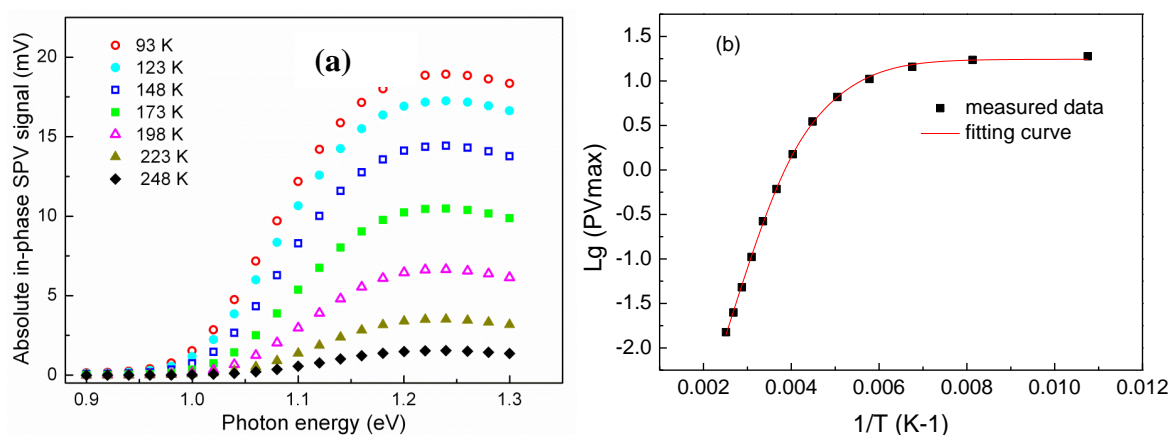


Figure 6.8 (a) Temperature dependent absolute in-phase SPV spectra of sample 145-CZTSSe ($x = 0.28$), and (b) Temperature dependence of the maximum SPV in-phase intensity of sample 145-CZTSSe ($x = 0.28$) together with the fitting curve using a two activation energies model (Equation 5.6).

To find out the activation energy of the defects involving in the recombination process, a two activation energy model, equation (5.6), was used to fitting the experimental data, as shown in Figure 6.8 (b). The two activation energies were found to be 120 ± 13 meV and 320 ± 13 meV. The activation energy of 120 ± 13 meV is very close to the value of 136 ± 10 meV determined by temperature dependent PL measurement, and therefore can be attributed to $(Zn_{Cu})^+$ defect states. Actually, the Cu and Zn disorders has also been revealed experimentally in kesterite type CZTS by Schorr *et al.* using neutron diffraction [14]. On the other hand, according the calculations by Chen *et al.* [138, 146], the observed defects with the ionization energy around 300 meV could be Cu_{Sn} , Sn_{Cu} , Zn_{Sn} , V_{Zn} , V_{Sn} , or V_{Se} . Among these all these defects, Cu_{Sn} and Zn_{Sn} were found to have the lowest formation energy. In particular, when the

CZTSSe is Cu-poor and Zn-rich, the formation energy for Zn_{Sn} is significantly decreased and the concentration of $[Zn_{Sn} + Cu_{Zn}]$ defect states increase significantly [138, 146]. Since our sample is Cu-poor and Zn rich, we proposed that Zn_{Sn} could be the observed acceptor defect.

6.4 Summary

In summary, this chapter has investigated the influence of preparation conditions such as the precursors, deposition processes and annealing conditions on the quality of the $Cu_2ZnSn(S_xSe_{1-x})_4$ thin film absorbers as revealed by surface photovoltage spectroscopy. The selenium content of the photo-electrically active phase in $Cu_2ZnSn(S_xSe_{1-x})_4$ thin films and the diffusion length are of great importance for the development of solar cells using $Cu_2ZnSn(S_xSe_{1-x})_4$ layers as absorbers. Our results implement that the annealing under selenium-containing atmosphere is necessary to get a high quality $Cu_2ZnSn(S_xSe_{1-x})_4$ thin film absorbers and the sample with the lowest sulfur content ($x= 0.28$) shows the strongest SPV signal. This is in accordance with the facts that record solar cells with $Cu_2ZnSn(S_xSe_{1-x})_4$ absorbers were obtained for $x= 0.03$ and $x= 0.4$ [20] (hydrazine based precursors) and that partial selenization of Cu_2ZnSnS_4 nanoparticle layers was needed for achieving a high energy conversion efficiency [9]. We have determined the diffusion length of sample 145-CZTSSe with $x= 0.28$ to be around $1 \mu m$. Two deep defect states with activation energies of 120 ± 13 meV and 320 ± 13 meV related to the recombination process have been identified. The defects states can be attributed to $[Zn_{Cu} + Zn_{Sn}]$ defect clusters.

7 Photovoltaic performance of $\text{Cu}_2\text{ZnSn}(\text{S}_x\text{Se}_{1-x})_4$ thin film absorbers

In order to examine the photovoltaic device properties of the synthesized $\text{Cu}_2\text{ZnSn}(\text{S}_x\text{Se}_{1-x})_4$ absorbers, solar cells were fabricated. In this chapter, the $\text{Cu}_2\text{ZnSn}(\text{S}_x\text{Se}_{1-x})_4$ thin films were used as absorber layers to fabricate solar cells with a Mo/CZTSSe/CdS/ZnO/ZnO:Al/Ni:Al grid structure, which is similar to traditional CIGS-based solar cell structure. The solar cells were characterized by current-voltage measurements under dark and illumination and by external quantum efficiency. To learn more about the limitation of device performance, temperature dependent current voltage characteristics were performed.

7.1 Basics of solar cells

To better understand the solar cells characterization, this section introduces the basic background and characteristic parameters of solar cells.

7.1.1 Characteristic parameters of solar cells

Solar cells are built to convert sunlight into electricity and consequently the most important parameter to classify solar cells is the power conversion efficiency η . The power conversion is defined as the ratio of electric power output (P_{el}) at the maximum power point P_{MPP} to the incoming irradiative power P_{in} . P_{MPP} is often described as a product of the current under short circuit conditions I_{SC} (with $j_{SC} = I_{SC}/A$, A being the area of the device), the voltage under open circuit conditions V_{OC} and the fill factor FF :

$$\eta = \frac{P_{el}}{P_{in}} = \frac{I_{SC} V_{OC} FF}{P_{in}} \quad (7.1)$$

To determine the maximum power output of the device it is necessary to measure the current flowing through the device as a function of the applied bias voltage, a measurement that in the following will be called an IV -curve or jV -curve, depending if it is referring to the current I (in mA) or the current density j (in mA/cm^2). The current I_{MPP} and voltage V_{MPP} correspond then to the point of the IV -curve where the power is at its maximum (Maximum Power Point, P_{MPP}). The fill factor is defined as:

$$FF = \frac{I_{MM} V_{MM}}{I_{SC} V_{OC}} \quad (7.2)$$

As the response of solar cells is not constant for different parts of the solar spectrum, it is necessary to define a common spectrum for usage in standard testing conditions. There are different definitions for this standards, but the one used in this dissertation is the most common one referred to as global AM1.5 solar spectrum (IEC 60904-3: 2008, see [147] for more details). Here the AM stands for the air mass. This spectrum simulates the terrestrial sunlight with an air mass of 1.5 and has a total intensity of 1000W/m². In practice, this spectrum is simulated with a carefully calibrated sun simulator which uses a combination of a Xe lamp and a Ha lamp to match the reference spectrum. In the standard testing conditions the efficiency is measured at a cell temperature of 25 °C.

7.1.2 Diode characteristic of solar cells

The main component of a solar cell is a p-n junction, as a result the current voltage response of a solar cells can be described by a diode with the saturation current density $J_{0,1}$ and diode quality factor A_1 :

$$j(V) = j_{0,1} \left(\exp\left(\frac{qV}{A_1 kT}\right) - 1 \right) \quad (7.3)$$

where k is the Boltzmann constant, T the temperature, V is the applied bias voltage, $j(V)$ the current density and q the elementary electric charge. For a better description of a real device, resistive losses have to be taken into account (a series resistance R_S corresponding to the resistive losses at the contacts and a parallel resistance R_P accounting for all other electronic losses in the device such as losses along the grain boundaries or through pinholes). Additionally, a photo-generated current density j_L has to be introduced into the equation to describe the device under illumination (in the dark $j_L = 0$). In thin film solar cells, J_L may depend on the applied bias voltage. The so-called 1-diode model describing the current-voltage characteristic of a solar cell is given by the following equation (for the equivalent circuit diagram, see figure 7.1):

$$j(V) = j_L - j_{0,1} \left(\exp\left(\frac{q(V - R_S j(V))}{A_1 kT}\right) - 1 \right) - \frac{V - R_S j(V)}{R_P} \quad (7.4)$$

where $J(V)$ accounts for the current density flowing through the device which is the sum of the current density flowing through the diode (first term), the current density flowing through the parallel resistance (second term) and the photo-generated current density (last term).

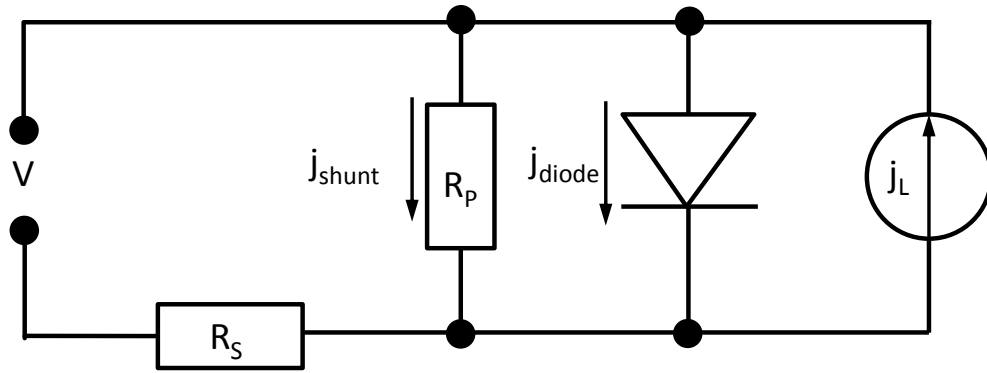


Figure 7.1 Equivalent circuit diagram of the solar cell in the 1-diode-model.

7.1.3 Quantum Efficiency

The quantum efficiency (QE) represents the photogenerated charge carriers collection ability of the photovoltaic device. The definition of the quantum efficiency is the ratio between numbers of collected photogenerated charge carriers to the number of irradiating photons. A quantum efficiency of 1 means therefore that all the photogenerated charge carriers can be collected by the photovoltaic device.

It should be noted that the internal and external QE are different. The internal quantum efficiency (IQE) includes all photons arriving at the surface of the device while external quantum efficiency (EQE) only takes the photons entering the device into account. In practice due to the reflection of the device surface, not all the photons reached the surface can enter into the device. Generally, EQE is measured, while the internal QE (IQE) can be calculated if the reflectivity (R_λ) of the device is known. The relationship between the EQE and IQE can be expressed as:

$$EQE(\lambda) = \frac{j(\lambda)}{q \Phi_0(\lambda)} = (1 - R_\lambda) IQE(\lambda) \quad (7.5)$$

where Φ_0 is the initial photon flux given in photons/ ($m^2 s$), $j(\lambda)$ is the electric current density of the device as a function of the incident photon wavelength, and q is the elementary electric charge. EQE data can be used to estimate the short circuit current density j_{SC} according to the following equation:

$$j_{SC} = \int q EQE(\lambda) \Phi_0(\lambda) d\lambda \quad (7.6)$$

7.2 Solar Cells fabrication and characterization

CZTSSe samples of 137-1-CZTSSe, 137-2-CZTSSe, 137-3-CZTSSe, and 145-CZTSSe, prepared by ligand-exchange process were used to fabricate solar cells (see details in Table 4.2). The structure of the solar cells is shown in Figure 7.2.

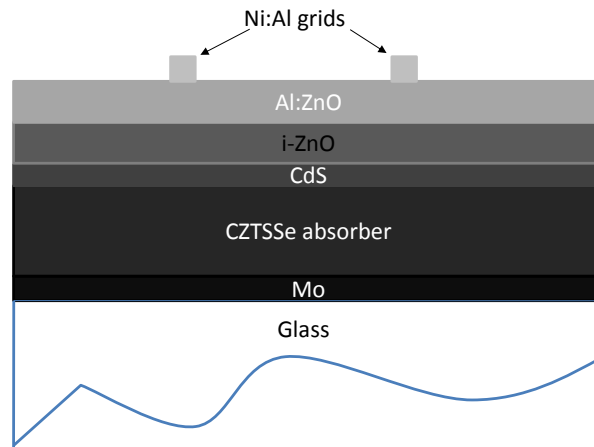


Figure 7.2 Schematic diagram of the CZTSSe-based thin film solar cell structure.

Prior to the deposition of CdS, the CZTSSe absorbers were sequentially etched by 5 % HCl (volume ratio) at 75 °C and KCN for 5 min, respectively. The devices were completed with a chemical bath deposited CdS buffer layer, followed by sputtered intrinsic ZnO window layer, and highly conductive Al-doped ZnO front contact. Ni:Al grids were deposited as the charge carriers collector by evaporation. Finally, the devices were mechanically scratched into a total area 0.5 cm² solar cells. J-V measurements were performed using an in-house class A sun simulator under standard test conditions (AM 1.5G, 100 mW/cm² and 23 °C).

To identify the dominated recombination mechanism, temperature and illumination dependent J-V measurements were carried out inside a cryostat which has a transparent window allowing the light pass through. The samples were mounted on a hollowed steel stage which can be flooded with liquid nitrogen to cool down the sample. The temperature was detected by a thermocouple and balanced by an electrical heater. During the measurement, the cryostat is maintained at a pressure of about 10⁻⁶ mbar by using a turbo pump. The measuring temperature was in the range of 150 to 300 K in step of 10 K. The sample is illuminated by a

single halogen lamp and there is a shutter to switch from dark to illuminated conditions. It should be noted that a single halogen lamp used leads to differences in the spectral content compared to the measurements under standard sun simulator. The mismatch was partly compensated by adjusting the short circuit current to be the same as measured under standard sun simulator, which was fulfilled by adjusting the distance between the lamp and the solar cell measured. This ensures that the current flowing across the device is the same as that obtained under one sun simulator.

External Quantum efficiency (EQE) analysis was carried out using an illumination system including two sources (halogen and xenon lamps) and a Bentham TM300 monochromator (Bentham Instruments, Berkshire, UK). Reference measurements were performed on calibrated Si and Ge detectors.

7.3 Current-Voltage characteristics and external quantum efficiency

Figure 7.3 shows the current density - voltage (J-V) characteristic of the best devices samples 137-1-CZTSSe, 137-2-CZTSSe, 137-3-CZTSSe, and 145-CZTSSe under dark and simulated 1 sun AM1.5G illumination. Devices fabricated from 137-1-CZTSSe absorbers show nearly straight line which indicates that there is shunting in the devices. As a result, no efficiency was measured from this sample. This CZTSSe absorbers were prepared by spin coating four sequential layers of nanoparticle precursors with each layer experienced ligand exchange with $(\text{NH}_4)_2\text{S}$. The shunting could be due to the existence of cracks in the CZTSSe thin film absorbers resulting from the ligand-exchange processes (see Figure 4.13).

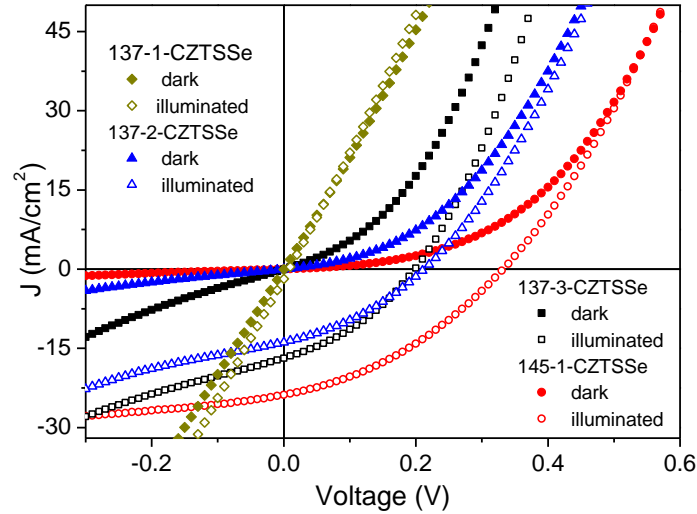


Figure 7.3 J - V characteristics of the best photovoltaic devices from samples 137-1-CZTSSe, 137-2-CZTSSe, 137-3-CZTSSe, and 145-CZTSSe under dark and simulated 1 sun AM1.5G illumination.

To reduce the cracks in the CZTSSe absorbers, the ligand-exchange layer/layers were cover with non-ligand-exchange layers/layer (samples 137-2-CZTSSe, and 137-3-CZTSSe, see detail in Table 4.2). Solar cells fabricated from these CZTSSe absorbers shows efficiencies of 1.0 % and 1.2 % for samples 137-2-CZTSSe, and 137-3-CZTSSe, respectively. In addition, by using a two-step annealing process, the solar cell performance was further improved to 2.8 % with open circuit voltage of 332.2 mV, short circuited current density of 23.8 mA/cm² and fill factor of 35.7 %. It should be noted that the efficiency of this device was increased to 3.0 % after storage of the device in a desiccator under vacuum for around four months, which is due to the increase of the short circuit current density by 3.7 mA/cm² despite a decrease of the open circuit voltage by around 26 mV.

Nevertheless, the efficiencies of our solar cells are still much lower than the record efficiencies of 11.1 % reported by Todorov *et al.* [4] who fabricated the CZTSSe solar cells from a hydrazine-based CZTSSe absorbers. One of the possible reasons for the low efficiencies is the existence of a carbon-rich layer near the back contact in our CZTSSe absorber layers (See Figure 4.15). Another possible reason could be that the chemical composition in our CZTSSe thin film absorbers ($\text{Cu}/(\text{Zn}+\text{Sn}) = 0.72$ and $\text{Zn}/\text{Sn} = 1.0$) was not

well optimized. Although it is still unclear what the optimal chemical composition is for the CZTSSe-based solar cells, the reported chemical composition of CZTSSe absorber for the high efficient CZTSSe-based solar cells is Cu-poor and Zn-rich with the metal ratio in the range of $Cu/(Zn+Sn) = 0.78-0.86$, and $Zn/Sn = 1.15-1.35$ [7, 9, 31, 36, 55].

Table 7.1 Device characteristics for the best solar cells from samples 137-1-CZTSSe, 137-2-CZTSSe, 137-3-CZTSSe, and 145-CZTSSe. The diode ideality factor A_1 , diode saturation current density j_{01} , dark series resistance R_{SD} and dark shunt resistance R_{PD} were obtained by fitting the dark j-V curves of the corresponding devices using one diode model (equation (7.4)).

	illuminated				dark			
	V_{oc} (mV)	j_{sc} (mA/cm ²)	FF (%)	η (%)	A_1	J_{01} (mA/cm ²)	R_{SD} (Ω cm ²)	R_{PD} (Ω cm ²)
137-1-CZTSSe	8.1	0.9	25.0	0.0	1.33	1.46	2.67	2
137-2-CZTSSe	212.4	13.8	34.2	1.0	2.61	0.36	2.30	109
137-3-CZTSSe	198.6	16.8	34.9	1.2	2.34	0.61	1.28	30
145-CZTSSe	332.2	23.8	35.6	2.8	3.33	0.22	2.25	449

Table 7.1 summarizes the characteristic parameters for the best solar cells from samples 137-1-CZTSSe, 137-2-CZTSSe, 137-3-CZTSSe, and 145-CZTSSe. All the devices show similar series resistance of around 1.28-2.67 Ω cm² under dark. However, the shunt resistances are significant difference with sample 137-1-CZTSSe showing the lowest value at 2 Ω cm² and 145-CZTSSe showing the highest value at 449 Ω cm², which could be due to the reducing cracks and increasing coverage of the large grains over the carbon-rich layer.

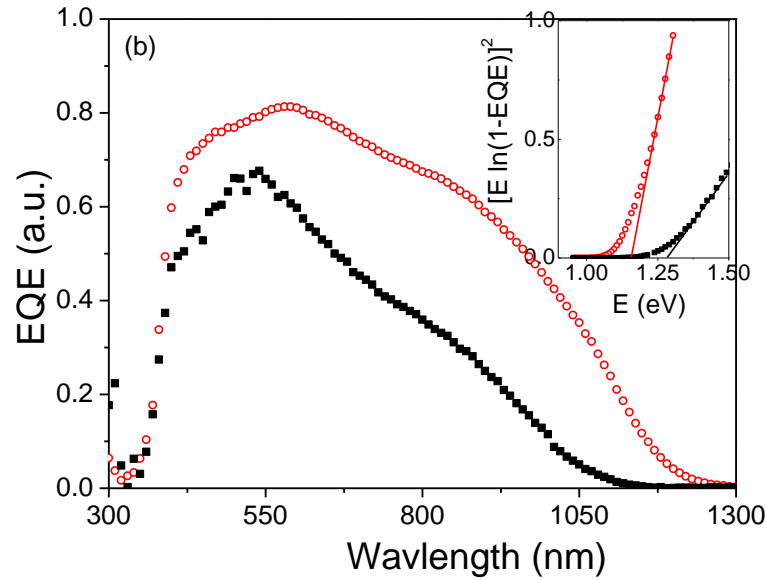


Figure 7.4 External quantum efficiency curves of the best photovoltaic cells from samples of 137-3-CZTSSe, and 145-CZTSSe. Inset: band gap determination from EQE data.

Figure 7.4 shows the external quantum efficiency (EQE) curve of the best photovoltaic cells from samples of 137-3-CZTSSe, and 145-CZTSSe. The highest EQE is over 65 % and 80 % for devices 137-3-CZTSSe, and 145-CZTSSe, respectively. In addition, device of sample 145-CZTSSe shows better response than that of device from 137-3-CZTSSe in the infrared region, which is related to the band gap of the CZTSSe absorbers. By integration the EQE curve over the wavelength using equation (7.6) [148], the short circuit current density were obtained to be 16.9 for devices of 137-3-CZTSSe, which is in good agreement with the value determined by the J-V measurement under one sun simulator. Similarly, the short circuit current density is estimated to be 28.2 mA/cm² from the EQE curve of device 145-CZTSSe. This value is larger than that of 23.8 mA/cm² but close to the value of 27.5 mA/cm² measured around four months later using one sun simulator.

The band gaps of the CZTSSe absorber layers were estimated to be 1.28 eV and 1.15 eV for sample 137-3-CZTSSe and 145-CZTSSe, respectively, from the EQE data by plotting the square of $(E - \ln(1 - EQE))$ versus photon energy [4]. The band gap of 1.15 eV is very close to the reported 1.13 eV for record efficiencies solar cells [4].

7.4 Temperature dependent current-voltage characterization

To identify the limitation of the device performance, temperature dependent J-V measurements were performed on the best device of sample 145-CZTSSe. Figure 7.5 illustrates the evolution of the J-V curves as a function of temperature. The open circuit voltage of the device shifted towards higher value with decreasing temperature while the short circuit current density decreased as the temperature decreased.

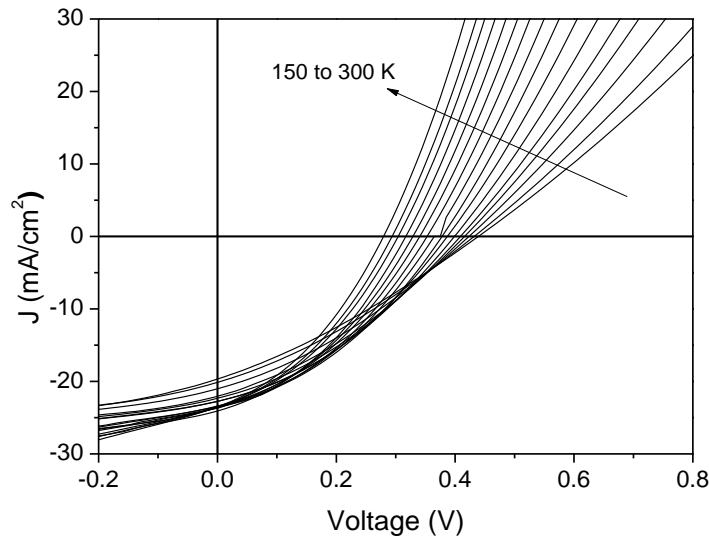


Figure 7.5 Temperature dependent J-V characteristics of the device from sample 145-CZTSSe. The measurements were performed in the temperature range of 150 – 300 K.

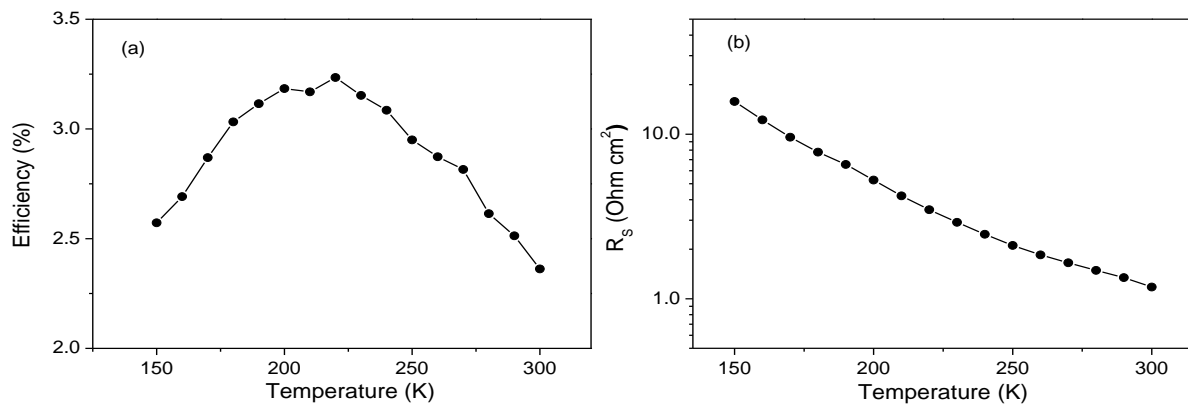


Figure 7.6 (a) Evolution of efficiencies with temperature; (b) evolution of series resistance (R_s) with temperature under dark condition. The series resistance was determined by fitting the J-V curve using the one diode model (equation (7.4)).

Figure 7.6 (a) depicts the evolution of the efficiencies as a function of temperatures. The efficiencies increased drastically with decreasing temperature and saturated below 220 K after which the efficiencies collapsed. This effect can be related to the dramatic increase of series resistance in the low temperature range, as shown in Figure 7.6 (b). This behavior is in agreement with the literature reports for the CZTSSe-based thin films solar cells [4, 149].

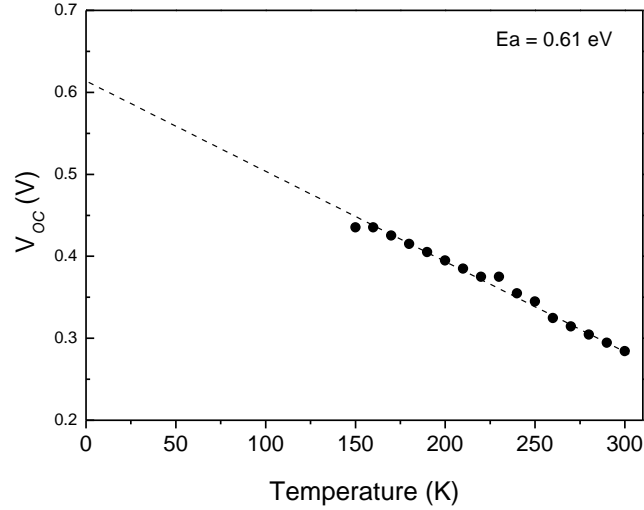


Figure 7.7 Temperature dependent open circuit voltages. The activation energy was estimated to be 0.61 eV.

Figure 7.7 shows the temperature dependent open circuit voltage for the record CZTSSe solar cells from sample 145-CZTSSe. The relationship between V_{OC} and temperature (T) is given as equation (7.7):

$$V_{OC} = \frac{E_a}{q} - \frac{AkT}{q} \ln\left(\frac{J_{00}}{J_L}\right) \quad (7.7)$$

where E_a , A , k , J_{00} , and J_L are the activation energy of the dominant recombination mechanism, diode ideality factor, Boltzmann constant, reverse saturation current prefactor and the photocurrent, respectively. The activation energy E_a is the intercept of the linear extrapolation of the temperature dependent V_{oc} curve when the temperature T is 0 K. The activation energy E_a was found to be 0.61 eV, which is significantly lower than the observed band gap of 1.15 eV for the current solar cell. Generally, if E_a equals to the band gap of the absorber, then the dominated recombination pathways is situated in the bulk of the absorbers;

when E_a is smaller than the band gap of the absorbers, the dominated recombination is located at the interface of the heterojunction[150]. Therefore, we can conclude that in our case the dominated recombination pathway is situated at the CZTSSe and CdS interface, which is in agreement with the previous reports [4, 21, 151].

7.5 Summary

As a proof of concept, CZTSSe-based solar cells have been fabricated from the ligand-exchange samples using a soda lime glass/Mo/CZTSSe/CdS/ZnO/ZnO:Al/Ni:Al grid structure. No efficiency has been observed in the devices fabricated from a CZTSSe absorber with ligand-exchange for all four sequential layers due to lots of cracks in CZTSSe thin films. By covering the ligand-exchange layer/layers with non-ligand-exchange layers/layer, solar cells with efficiencies around 1 % can be achieved. Further optimizing the deposition process of the CZTSSe thin film absorbers using a two-step annealing processes, solar cells performance was improved to 2.8 %, which was improved to 3.0 % after being stored in a desiccator for around four months. The limitation for the device performance was found to be the high interface recombination by temperature dependent j-V analysis, which is in accordance with that of the recorded efficient CZTSSe solar cells. However, the activation energy was reported to be 0.97 eV which is higher than that of 0.61 eV observed for our devices. Another limitation for the performance of our devices is the low shunt resistance for our CZTSSe solar cells. Further optimization of the preparation parameters of the absorber layers such as the annealing process and the chemical composition of the absorbers is important in order to further improve the performance of the solar cells.

8 Summary

The goal of this thesis is to develop a cost-effective approach for the deposition of $\text{Cu}_2\text{ZnSn}(\text{S}_x\text{Se}_{1-x})_4$ with $0 \leq x \leq 1$ thin film absorbers using solution processes. The CZTSSe thin film absorbers were achieved by a four-step process.

In the first step, ZnS, SnS and Cu_3SnS_4 nanoparticles were synthesized by a heating-up colloidal route in the reaction temperature range 200 °C and 300 °C using oleylamine as both solvent and surfactant. It is found that the reaction temperature below 250 °C and the precursor ratio of Sn: S = 1: 1 gave the purest SnS nanoparticles while a precursor ratio of Sn: S = 1: 2 and a reaction temperature of 300 °C resulted in more homogeneous in terms of size and shape of the nanoparticles but containing increasing amount of SnS_2 secondary phase. The growth of the Cu_3SnS_4 nanoparticles was found to first follow the focusing of size distribution mechanism up to a reaction time of 120 min, after which it follows an Ostwald ripening mechanism.

In the second step, Cu-Zn-Sn-S precursor films were deposited by spin coating ZnS, SnS and CTS nanoparticle inks. Heat treatments at moderate temperature to remove the solvent and partial oleylamine surfactant as well as to dense the films on the substrates served as the third step. In the fourth step, the $\text{Cu}_2\text{ZnSn}(\text{S}_x\text{Se}_{1-x})_4$ with $0 \leq x \leq 1$ absorbers were formed by annealing the Cu-Zn-Sn-S precursor films at the temperature range of 400 °C to 580 °C under S/Se-containing atmosphere.

Formation of $\text{Cu}_2\text{ZnSn}(\text{S}_x\text{Se}_{1-x})_4$ ($0 \leq x \leq 1$) phases was confirmed by both XRD and Raman spectroscopy for the annealing temperature above 400°C. Crystal quality increased with increasing annealing temperature and increasing amount of Se can be achieved with increasing annealing temperature. Secondary phases of SnS and Cu_2S were found in the non-ligand-exchanged in all these samples and an extra secondary phase of SnS_2 was detected in samples annealed above 540 °C. For the samples annealed under Se atmosphere, except for the dominant CZTSSe phases, SnS and SnSe_2 phases were observed as minor secondary phases.

Ligand-exchange with $(\text{NH}_4)_2\text{S}$ for all successive spin coated precursors' layers resulted in cracks in the resulting CZTSSe thin films. Crack-free CZTSSe thin film absorbers can be achieved by combining the ligand-exchange and non-ligand-exchange processes. A double-layered structure with homogeneous large grain layer on top and fine grain layer near the substrates was formed when the precursor films were annealed under Se-containing atmosphere. The reasons for the formation of layered structure were found to be the existence of high content of carbon in the fine grains which serves as barrier for the growth of the nanoparticles and the highly Sn-rich in the fine grain layer which deviates from the stoichiometry of CZTSSe.

Photoluminescence from $\text{Cu}_2\text{ZnSn}(\text{S}_x\text{Se}_{1-x})_4$ thin films with different stoichiometry was generally attributed to donor to acceptor pair recombination. The activation energies for the DAP recombination process in the pure sulfide CZTS was estimated to be 20 ± 10 meV, which could probably be attributed to the V_{Cu} . For the selenium-containing CZTSSe thin films with Cu-poor and Zn-rich, defect states related to $(\text{Zn}_{\text{Cu}})^+ / V_{\text{Cu}}^-$ donor and acceptor pairs were identified. It should be pointed out that potential fluctuation may exist in the selenium containing CZTSSe thin films where a blue shift over 10 meV with increasing excitation power were observed.

Surface photovoltage spectroscopy analysis on the $\text{Cu}_2\text{ZnSn}(\text{S}_x\text{Se}_{1-x})_4$ (with $0 \leq x \leq 1$) thin film absorbers indicates that the $\text{Cu}_2\text{ZnSn}(\text{S}_x\text{Se}_{1-x})_4$ thin films were p-type. Annealing under Se-containing atmosphere is necessary to obtain high quality $\text{Cu}_2\text{ZnSn}(\text{S}_x\text{Se}_{1-x})_4$ thin film absorbers (with higher SPV signal). A diffusion length of electrons in $\text{Cu}_2\text{ZnSn}(\text{S}_x\text{Se}_{1-x})_4$ with $x=0.28$ was estimated to be around 1 μm . Two deep defect states with activation energies of 120 ± 13 meV and 320 ± 13 meV related to the recombination process in $\text{Cu}_2\text{ZnSn}(\text{S}_x\text{Se}_{1-x})_4$ with $x=0.28$ have been identified. The defect states could be attributed to $[\text{Zn}_{\text{Sn}} + \text{Zn}_{\text{Cu}}]$ defect clusters according to the theoretical calculations [138, 146].

As a proof of concept, CZTSSe-based solar cells have been fabricated from the ligand-exchange processed CZTSSe thin film absorbers using a soda lime glass/Mo/CZTSSe/CdS/ZnO/ZnO:Al/Ni:Al grid structure. Preliminary optimization of the deposition process of CZTSSe thin films, 3.0 % efficient solar cells were achieved, showing the promising of this solution deposition approach for CZTSSe thin film solar cells. The loss

mechanism of the device was found to be dominated by the CZTSSe/CdS interface recombination.

Further work on optimization of the ligand-exchange process is important, i.e. concentration of the $(\text{NH}_4)_2\text{S}$ solution exchanging time, to reduce carbon content in the resulting absorber layers. Formation of the kesterite $\text{Cu}_2\text{ZnSn}(\text{S}_x\text{Se}_{1-x})_4$ ($0 \leq x \leq 1$) phase at low temperature i.e. 400°C may be helpful in minimizing the diffusion of the Cu and Zn from the bottom to the surface of thin films before going to the high temperature selenization process. Further work involving the adjustment of the chemical composition of the resulting CZTSSe absorbers to that of the record devices reported by Todorov *et al.* [4] is essential for the further improvement of the device performance. Further analysis of band alignment at CZTSSe/buffer layers interfaces would be crucial in selection of an optimal buffer layer for CZTSSe-based heterojunction solar cells.

Appendix A

A.1 Overview of samples used for PL and SPV analysis

Table A.1 Detail preparation parameters of CZTSSe samples using for the photoluminescence and surface photovoltage analysis. The nanoparticles were dispersed in 2.5-3 mL hexanethiol. All the samples are on Mo-coated soda lime glass substrates. Heat treatments at 170 °C for 2 min and 350 °C for 2 min for every layer were carried out for all the samples. Samples 137-3-CZTSSe and 145-CZTSSe which are shown in Table 4.2 are also listed below.

	Precursor inks	No. of layers	Annealing conditions			Ligand exchange with 0.04 M (NH ₄) ₂ S Me-OH solution for around 30 s
			Tem. (°C)	Time (min)	atmosphere	
125-CZTSSe	1 mmol CTS-B and 1.25 mmol ZnS	1	540	60	Ar-H ₂ S (5 %)	/
137-3-CZTSSe	0.67 mmol CTS-B, 1.37 mmol ZnS and 0.45 mmol SnS-300	4	580	25	Ar-Se	the first spin coated layer
137-4-CZTSSe		5	560	20	Ar-H ₂ S (5 %) –Se	/
137-5-CZTSSe		5	560	20	Ar-H ₂ S (5 %) –Se	/
145-CZTSSe	0.67 mmol CTS-B, 1.45 mmol ZnS and 0.65 mmol SnS-300	2	580	5	Ar-Se	the first spin coated layer
		3	580	25	Ar-Se	first two spin coated layers
154-CZTSSe-B A	0.67 mmol CTS-B, 1.69 mmol ZnS and 0.87 mmol SnS-300	3	/	/	/	Only for the first spin coated layer

A.2 Relative chemical composition of samples used for PL analysis

Table A.2 The relative ratios of Cu/(Zn+Sn), Zn/Sn and S/(S+Se) for samples used for PL analysis are shown in table 5.2. The ratios of Cu/(Zn+Sn) and Zn/Sn were calculated from the

Appendix A

EDX analysis for samples 125-CZTSSe, 137-CZTSSe, and 145-CZTSSe. The ratios of S/(S+Se) were determined from the XRD data (Figure A.1) according to the Vegard's Law (Equation 4.2) using the 112 peak.

	Cu/(Zn+Sn)	Zn/Sn	S/(S+Se)
125-CZTSSe	1.0	1.5	1
137-3-CZTSSe	0.93	1.27	0.36
145-CZTSSe	0.72	1.00	0.28

A.3 XRD patterns of samples used for PL and SPV analysis

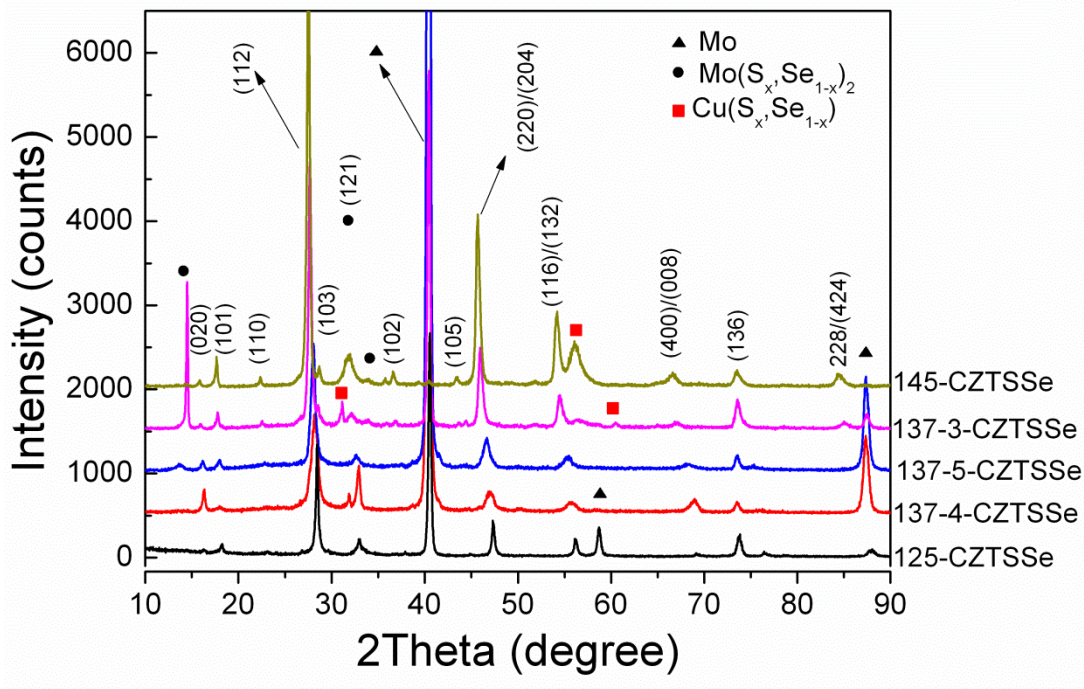


Figure A.1 XRD patterns of samples used for the PL and SPV analysis.

The XRD patterns show the formation of CZTSSe phase. Secondary phases like $\text{Cu}(\text{S}_x\text{Se}_{1-x})$ were also found in samples 137-3-CZTSSe and 145-CZTSSe. Formation of $\text{Mo}(\text{S}_x\text{Se}_{1-x})_2$ phases were found in samples 137-3-CZTSSe and 145-CZTSSe.

A.4 EDX line scanning profile of precursors' films

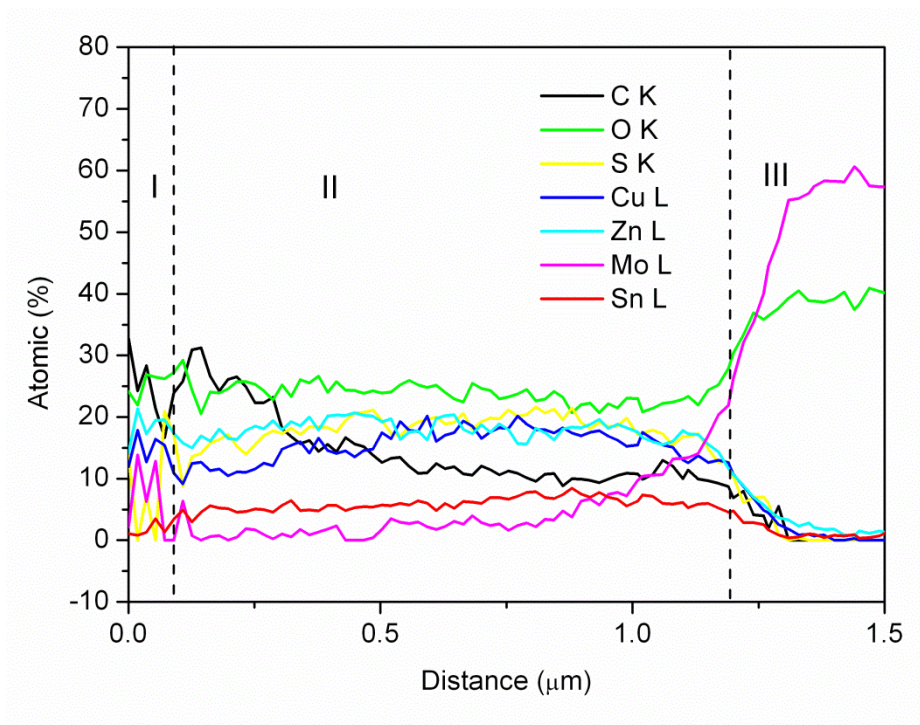


Figure A.2 EXD line scanning across the cross section of the as-deposited precursor films (154-CZTSSe-BA). Three regions are marked in the figure: region I is the sample surface; region II is the cross section of the precursor films and region III is the Mo substrate.

Figure A.2 shows the EDX line scanning profile through the cross section of the as-deposited 154-CZTSSe-BA thin films. The elements of Cu, Zn, Sn, and S are homogeneously distributed. Higher content of C is observed in the surface of the precursor films than in the films near the substrate, indicating the reduction of C content due to the ligand exchange. However, existence of around 10 at.% of C near the in the ligand-exchange layer reveals that the ligand-exchange process is not sufficient to remove all the organic ligand. Therefore, further optimization of the ligand-exchange process is necessary to completely remove the organic ligand from the precursor thin films.

Appendix B Synthesis of $\text{Cu}_2\text{Zn}_x\text{Sn}_y\text{Se}_{1+x+2y}$ nanocrystals with wurtzite-derived structure

The content in this Appendix has been published in [152].

B.1 Introduction

Copper-based ternary and quaternary semiconductors such as CuInS_2 (CIS), $\text{Cu}(\text{In,Ga})\text{Se}_2$ (CIGS), $\text{Cu}_2\text{ZnSnS}_4$ (CZTS) and $\text{Cu}_2\text{ZnSnSe}_4$ (CZTSe) are of great interest due to their potential application as light absorbing materials in thin film solar cells. Among them, CZTS and CZTSe have been considered as the alternative of CIGS as the absorber layers for low cost, high efficiency and sustainable solar cells owing to their intrinsic properties such as abundance of constituents, direct band gap of 1.0-1.5 eV, and high optical absorption coefficient exceeding 10^4 cm^{-1} in the visible range [17, 153, 154]. Solution thin film deposition techniques have been considered as one of the most promising routes to decrease the cost of the device fabrication due to the non-vacuum environment and low capital equipment costs [3, 9, 56, 155, 156]. Hydrazine-based solution process of $\text{Cu}_2\text{ZnSn}(\text{S,Se})_4$ (CZTSSe) thin film solar cells have achieved efficiencies as high as 11.1 % [4], which is the best CZTS(Se)-based thin film solar cells so far while CZTS nanocrystal-based solution process yielded 7.2 % efficiencies [9]. Both of these reports demonstrated CZTSSe as a promising absorber layer for high performance photovoltaic devices. Generally, there are two kinds of crystal structures, kesterite and stannite, for both CZTS and CZTSe based on the literature reported while kesterite is the ground-state structure according to the theoretical and experimental studies [14, 15, 157]. Both of these two structures are zinc-blende derived structures. Interestingly, two corresponding wurtzite derived structures, wurtzkesterite and wurtzstannite, are reported theoretically by Chen *et al.* [158] recently through a global search based on the valence octet rule. Similar the structure relation between kesterite and stannite, wurtzkesterite and wurtzstannite have a similar unit cell but differ in the occupation of Cu, Zn and Sn cations. Kesterite and stannite types CZTS(Se) NCs, nanosheets and nanowires have been extensively reported [58, 59, 159-164]. Moreover,

recently several groups reported the synthesis of metastable phases of CZTS and CZTSe such as wurtzite-type [164-167], orthorhombic wurtz-stannite [167] CZTS NCs and wurtzite type CZTSe NCs [168]. All these reports focus on the manipulation of the organic solvents to get a single phase of the metastable structure CZTS(Se) NCs. However, there are few reports about the influence of the metal salt precursors on the structure and composition of the CZTS(Se) NCs. Rath *et al.*[169] reported that the chemical composition of CZTSe NCs strongly depends on the metal salt reactants used for the synthesis. Herein we report a synthesis of CZTSe NCs by using oleylamine and oleic acid as solvent and capping agent. We found that the influence of the metal salt reactants not only on the chemical composition but also on the structure of the CZTSe NCs.

B.2 Experimental details

Materials

Copper (II) chloride dehydrate (99 %), zin chloride anhydrate (97 %) and zinc acetate dihydrate (98 %) were purchased from Alfa Aesar. Copper acetylacetonate (>99,99 %), Tin(II) chloride (>99,99 %), diphenyl diselenide (98 %), oleic acid (technical grade, 90 %), oleylamine (technical grade, 70 %), absolute ethanol, hexane and toluene were purchased from Aldrich. Sodium oleate (>97.0 %) was from TCI Europe. All chemicals were used directly without any further purification.

Preparation of copper-oleate and zinc-oleate precursors

The copper-oleate complex was synthesized by reaction of $\text{CuCl}_2 \cdot 2\text{H}_2\text{O}$ with sodium oleate [170]. Specifically, 10mmol $\text{CuCl}_2 \cdot 2\text{H}_2\text{O}$ and 20 mmol sodium oleate were dissolved in a mixture solvent composed of 10 ml ethanol, 15 ml distilled water and 35 ml hexane with continuous stirring. The obtained solution was heated to 70 °C and held at this temperature for 4 hours. When the reaction was completed, the upper organic layer containing the copper–oleate complex was washed three times with 10 ml distilled water in a separatory funnel. After washing, hexane was evaporated off, resulting in copper–oleate complex in a waxy solid form. Zinc-oleate was prepared by the same procedure.

Synthesis of CZTSe NCs

Sample A: CZTSe NCs containing both wurtzite type and kesterite structure were synthesized by using copper oleate, zinc oleate and tin chloride as the cation precursors. In a typical synthesis, 1 mmol copper oleate, 0.5 mmol zinc oleate, 1 mmol diphenyl diselenide and 25 mL oleylamine were added to a 100 mL three-neck flask in air, then the flask was removed to a glove box filled with nitrogen and heated to 120 °C with N₂ bubbling and held at this temperature for 30 min. The mixture was then heated to 250 °C. In a separate two-neck flask, the mixture of 0.5 mmol SnCl₂, 2 mL oleic acid and 5 mL oleylamine was heated to 120 °C with N₂ bubbling in the glove box for 30 min, then allowed to cool to 70 °C. When the temperature of the former solution was raised to 250 °C, the mixture of SnCl₂, oleic acid and oleylamine was injected. After injection the temperature was raised to 230 °C and kept at this temperature for 60 min to allow the reaction. After that, the reaction solution was cooled down to room temperature. The NCs were precipitated with excess ethanol and were centrifuged at 6000 rpm for 10 min. After centrifugation, the supernatant was discarded, and the NCs were redispersed in toluene. The precipitation and dispersion steps were repeated one more time to remove excess oleylamine and oleic acid. Finally the NCs were redispersed in 10 ml toluene for further characterization.

Sample B: sample B was synthesized by changing the injection temperature and the reaction temperature to 230 and 250 °C respectively while maintaining the other conditions in the preparation of sample A.

Samples C was synthesized by replacing the copper oleate and zinc oleate with copper acetylacetonate and zinc acetate dihydrate respectively but keeping the other conditions unchanged in the preparation of sample B.

Characterization

X-ray diffraction (XRD) patterns were operated in the 2θ range from 10 to 90° on a Bruker D8-Advance X-ray diffractometer with CuKα1 radiation using a step size of 0.02° and step time of 4 second. The data were analysed by Rietveld refinement to determine the lattice parameters and weight fractions of the phases [171]. Transmission electron microscopy (TEM) samples were prepared by dropping diluted NCs solution onto a carbon film coated gold grids and a Philips CM12 transmission electron microscopy was used to acquire TEM images of the NCs. For the Raman measurement a Ti: Sa-ring-laser was used as an excitation. The

wavelength of the laser is fully tunable from 690 nm to 1050 nm. To avoid laser heating the beam power was kept below 3.5 mW. Raman spectra were recorded with a Horiba T64000 triple monochromator system in backscattering configuration with a microscope and a motorized XY stage. The micro-Raman spectroscopy with a 100× objective was performed at room temperature for a wavelength of 747 nm. The optical properties of the as-prepared CZTSe NCs were characterized by UV-visible absorption spectroscopy recorded on a Lambda 950 UV-Vis spectrometer.

B.3 Results and discussion

Figure B.1 shows the XRD patterns of CZTSe NCs prepared under different conditions. By visual inspection of the data it can be noticed, that additional to the Bragg peaks arising from a kesterite type phase other peaks occur, which may belong to secondary

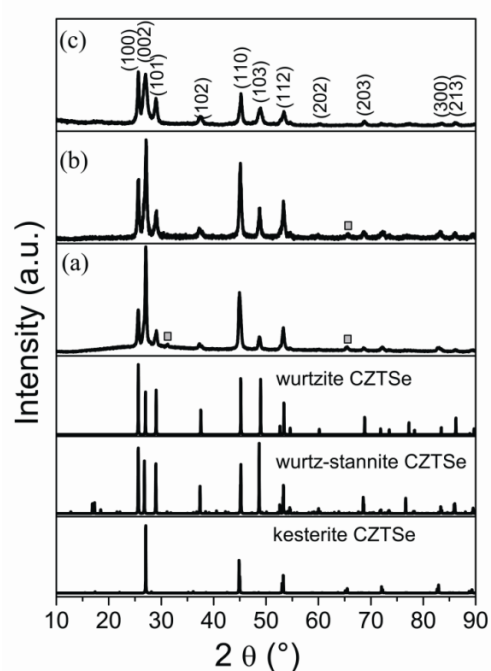


Figure B.1. XRD patterns of (a) sample A, (b) sample B and (c) sample C. For reference, the simulated diffraction patterns of wurtzite type, wurtz-stannite type and kesterite type CZTSe are shown below. The simulated patterns were obtained by the software of powder cell.

phases. Therefore, we simulated the diffraction pattern of wurtzite type CZTSe assuming a random distribution of the cations on the *Wyckhoff* position 2b and of the wurtz-stannite type CZTSe assuming copper on the 4b position and zinc and tin on two different 2a positions (See Table B.S1 and S2 for details), to compare them with the experimental results. The intensity ratio of the three Bragg peaks in the 2θ region $24^\circ - 30^\circ$ indicate clearly the existence of a kesterite type phase and a wurtzite type phase. Special attention should be paid to the Bragg peaks in the region from 28.3° to 29.8° and 36.2° to 39.2° (see figure B. 2). The peak fits show clearly the existence of a third phase with wurtz-stannite type structure. In order to determine the lattice parameters and the fractions of the different phases, a Rietveld analysis of the powder X-ray diffraction pattern was performed. In the refinement three CZTSe phases were included, a kesterite type phase, a wurtzite type phase and a wurtz-stannite type phase. The Rietveld analysis shows, that the wurtzite and wurtz-stannite type phases are Sn poor, moreover the wurtzite type phase obeys a strong preferred orientation in $[00.1]$, which may be explained by the platelet like crystals.

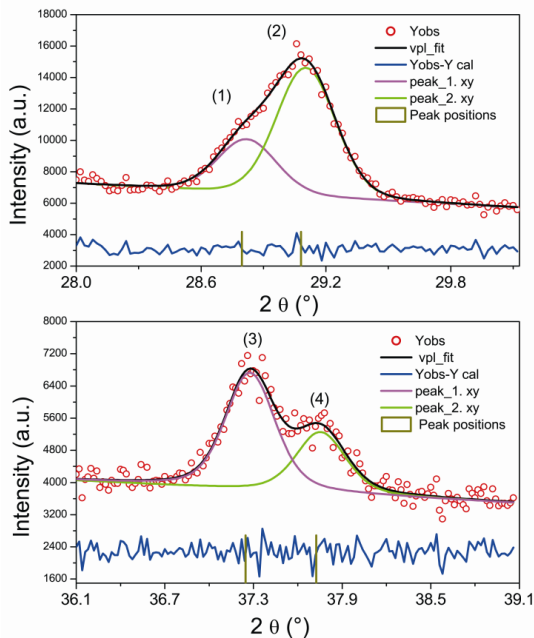


Figure B.2. Peak fits of parts of the diffraction pattern (within $28.3^\circ - 29.8^\circ$ and $36.2^\circ - 39.2^\circ$). The marked Bragg peaks correspond to: (1) 101 wurtzite and 211 wurtz-stannite; (2) 021 wurtz-stannite; (3) 102 wurtzite and 212 wurtz-stannite and (4) 022 wurtz-stannite.

Appendix B

The results of the Rietveld analysis are summarized in Table B.1. Comparing the phase content in the samples, in sample A kesterite type CZTSe is the main phase, whereas in sample C wurtzite type CZTSe dominates. The XRD results indicate that structure of the NCs can be transformed from kesterite type dominated structure to the wurtzite type dominated structure by controlling the reaction conditions. It should be noticed, that a third phase with wurtz-stannite structure is always present as a secondary phase, but with changing fraction. Furthermore, the average crystal sizes of samples A, B and C are 20.0, 22.2 and 17.6 nm, respectively, as determined by Scherrer equation using the 100 Bragg peak.

Table B.1. Results of the Rietveld analysis of the diffraction pattern (a), (b) and (c): lattice parameters and weight fractions. The d_{100} value of the wurtzite type phase was calculated using the obtained lattice parameters.

sample	phase (structure type)	lattice parameters (Å)	d_{100} [Å]	weight fraction
A	kesterite type	a=5.696 (1), c=11.451(2)		59 (5) %
	wurtzite type	a=4.017 (1), c=6.479 (1)	3.479	7 (2) %
	wurtz-stannite type	a=8.032 (2), b=6.938 (1), c=6.651 (1)		34 (3) %
B	kesterite type	a=5.684 (1), c =11.408 (2)		48 (4) %
	wurtzite type	a=4.015 (1), c =6.632 (1)	3.477	45 (4) %
	wurtz-stannite type	a=8.001 (2), b = 6.892 (1), c = 6.678 (1)		7 (2) %
C	kesterite type	a=5.680 (1), c =11.418 (2)		26 (2) %
	wurtzite type	a=4.004 (1), c =6.617 (1)	3.467	71 (5) %
	wurtz-stannite type	a=7.958 (2), b =7.413 (1), c = 6.675 (1)		3 (1) %

To study the morphology and further confirm the structure of the synthesized CZTSe NCs, TEM analysis on all three samples was carried out, as shown in Figure B.3. Figure B.3 (a) shows a low magnification TEM image of polydispersed CZTSe NCs with

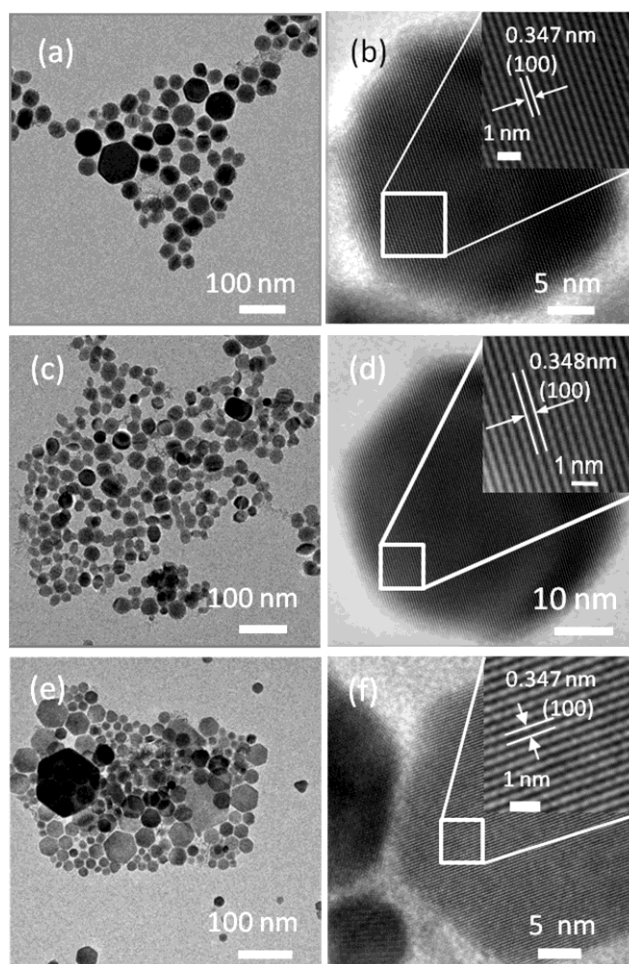


Figure B.3. (a) TEM image and (b) HRTEM of sample A; (c) TEM image and (d) HRTEM of sample B; (e) TEM image and (f) HRTEM of sample C.

hexagonal shape. The size of the NCs varies from 15 nm to 80 nm. High resolution TEM (HRTEM) image of a typical NC (Figure B.3 (b)) shows the high crystallinity of the CZTSe NCs with continuous lattice fringes throughout the whole particle. The distance between two lattice fringes was measured to be 0.347 nm corresponding to the (100) lattice plane distance (d_{100}) of wurtzite type CZTSe. Fig. 3(c) shows a low magnification image of sample B. Unlike sample A, the shape of CZTSe NCs of sample B is slightly irregular and the size distribution of the NCs is smaller in the range of 10 nm to 45 nm. However, the measured d spacing value of 0.348 nm from HRTEM image of a single NC (Figure B.3 (d)) is in agreement with the (100) lattice plane distance (d_{100}) of the wurtzite type CZTSe. Figure B.3 (e) indicates that CZTSe NCs of sample C are shaped in hexagon, which is similar with sample A. HRTEM image (Figure B.3 (f)) of a typical

Appendix B

hexagonal CZTSe NC exhibits clear lattice fringes with the same measured d spacing distance with that of sample A, indicating a wurtzite type structure.

Table B.2 Chemical composition of CZTSe NCs determined by EDX

	Cu (at %)	Zn (at %)	Sn (at %)	Se (at %)
Sample A	36.9	0.5	13.1	49.5
Sample B	33.1	2.5	12.9	51.5
Sample C	25.0	14.2	6.8	54.0

The chemical composition of the as-synthesized CZTSe NCs were studied by energy dispersive X-ray spectroscopy (EDX). Haas *et al.* [162], pointed out that CZTSe NCs prepared by oleylamine chemical route showd a broad range of chemical composition heterogeneity, therefore we analysed several randomly selected areas of the samples by EDX. The average atomic concentrations of the samples are shown in Table B.2. As shown in Table B.2, the chemical composition of the obtained CZTSe NCs can be tuned by changing the reaction conditions. For example, when the reaction temperature changed from 230 °C to 250 °C, the atomic ratio of zinc increased from 0.5 at% to 2.5 at%. Furthermore, Zn at% rose to 14.0 at% by substitutionreactants of copper acetylacetonate and zinc acetate dehydrate for Cu-oleate and Zn-oleate. The difference of the chemical composition may due to the differential relative reactivity of the reactants. The results of the PXRD and TEM measurements indicate that the structure and the composition of CZTSe NCs can be tuned by controlling the reaction conditions such as temperature and reactants.

It is known that XRD alone is not enough to rule out the the existence of secondary phases such as ZnSe, Cu₂SnSe₃ because of the similar XRD patterns among ZnSe, Cu₂SnSe₃ and CZTSe. Although the EDX measurements indicate that all four elements (Cu, Zn, Sn and Se) are presented in the as-synthesized products, it is also possible that the signals came from the mixture of ZnSe ad Cu₂SnSe₃. Therefore, to further confirm that the obtained products are CZTSe NCs rather than ZnSe, Cu₂SnSe₃ or the mixture of ZnSe and Cu₂SnSe₃, Raman spectroscopy measurement was performed on samples C, as shown in Figure B.4. The spectrum displays the strongest peak located at 191 cm⁻¹ which

is considered as the main feature of vibrational A1 symmetry mode from CZTSe [3, 101, 163, 172]. In addition, a shoulder peak at 173 cm^{-1} and a broad peak at 235 cm^{-1} were found by fitting the spectrum with Lorentzian curve using the software of Peak-of-mat. These two peaks can be attributed to CZTSe according to the literature reports [3, 101, 163, 172]. There are no additional peaks indicating the as-synthesized NCs are CZTSe.

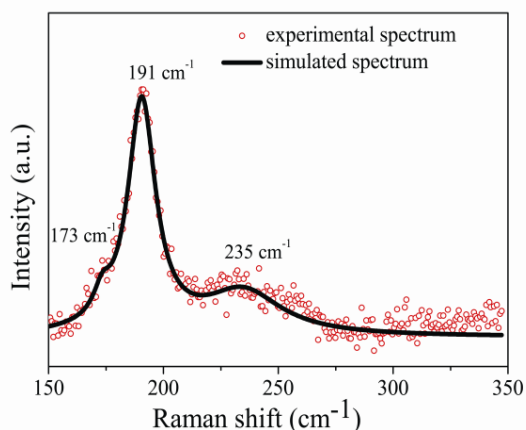


Figure B.4 Raman spectrum of CZTSe NCs (sample C) measured at room temperature.

The optical properties of the CZTSe NCs from the typical sample C have been studied by UV-Vis absorption spectroscopy, as shown in Figure B.5. The optical band gap energy was determined by extrapolating the linear region of the plot of $(\alpha h\nu)^2$ versus photon energy ($h\nu$) and taking the intercept on the $h\nu$ -axis. There are large discrepancies about the optical band gap energy of CZTSe based on the reported values which varied from 0.85 eV to 1.6 eV [34, 161, 163, 168, 172, 173]. Therefore, the estimated optical band gap energy of 1.38 eV is within the reasonable range.

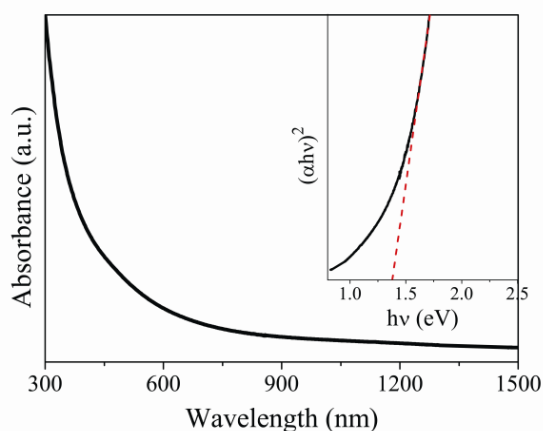


Figure B.5 UV-Vis absorption spectrum of CZTSe nanocrystals (sample C) dispersed in toluene. Inset is the plot of $(\alpha hv)^2$ versus $h\nu$ (eV) for the nanocrystals.

For the application of the CZTSe NCs in thin film photovoltaic devices, further annealing process of the CZTSe NC thin films at higher temperature to get a larger grain is necessary. Therefore, it is important to know the phase stability of wurtzite type CZTSe NCs. Jiang et al. showed that orthorhombic wurtz-stannite type CZTS particles can be transformed into kesterite type CZTS by annealing at 500 °C for 2h [167]. However, tin loss is known during the annealing process according to the literature reports [59, 93, 94]. To reduce the loss of tin, we annealed the samples at shorter time of 30 minutes at different temperatures (500 and 540 °C). The result of the XRD measurement (Figure B.6 (b)) shows that a kesterite type CZTSe phase is present besides the wurtzite type CZTSe after annealing at 500 °C at selenium vapour atmosphere for 30 minutes. However, the XRD pattern of CZTSe NCs annealed at 540 °C for 30 minutes (Figure B.6 (c)) reveals that all the Bragg peaks match very well with the kesterite type CZTSe and the Bragg peaks ascribing to wurtzite type CZTSe disappeared, indicating that the wurtzite CZTSe NCs have completely transformed to kesterite type structure.

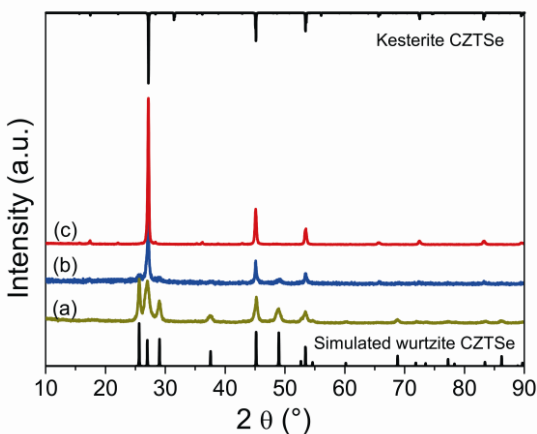


Figure B.6 XRD patterns of wurtzite-derived CZTSe before (a) and after annealing at 500 °C (b) and 540 °C (c) for 30 minutes in a selenium atmosphere.

B.4 Conclusions

In summary, a simple synthetic route for producing CZTSe NCs with tunable structure and composition is presented. The crystal structure of the CZTSe NCs can be tuned from mainly kesterite type to mainly wurtzite type by controlling the reaction conditions such as metal salt reactants and reaction temperature. XRD and TEM measurements confirm the structural properties of the CZTSe NCs. Raman spectroscopy measurement reveals that the as-obtained NCs are pure CZTSe without secondary phases such as ZnSe and Cu_2SnSe_3 . The wurtzite type CZTSe NCs transformed into the kesterite type CZTSe when annealed at 540 °C for 30 minutes. The optical band gap of the CZTSe NCs in solution was estimated to be 1.38 eV which is ideal for solar energy conversion.

B.5 Simulation diffraction pattern of kesterite type, wurtzite type and wurtz-stannite type CZTSe

Crystal structures

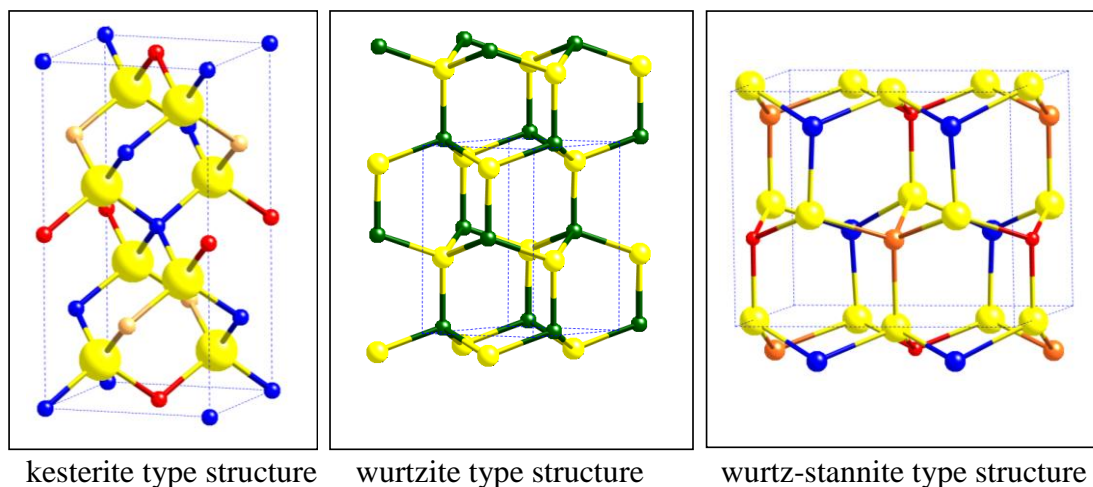


Figure. B.S1 Schematic representation of the unit cells of kesterite type, wurtzite type and wurtz-stannite type CZTSe (blue – Cu; orange – Zn; red – Sn; yellow – Se; green – random distribution of Cu,Zn and Sn)

Crystal structure data

Molecular formula	structure type	crystal system	space group
$\text{Cu}_2\text{ZnSnSe}_4$	kesterite	tetragonal	$\bar{1}42d$
$\text{Cu}_2\text{ZnSnSe}_4$	wurtzite	hexagonal	$P6_3mc$
$\text{Cu}_2\text{ZnSnSe}_4$	wurtz-stannite	orthorhombic	$Pmn2_1$

Table S0: Atomic coordinates related to the kesterite type structure (8g is an (x,y,z) position, nevertheless x and y are very similar)

Atom	Wyckhoff position	x	y	z
Cu	2a	0	0	0
Cu	2c	0	1/2	1/4
Zn	2d	1/2	0	1/4

Appendix B

Sn	2b	1/2	1/2	1
Se	8g	0.2587	0.2587	0.3714

Table S1: Atomic coordinates related to the wurtzite type structure (2b is the $(1/3, 2/3, z)$ position)

Atom	Wyckhoff position	x	y	z
Se	2b	1/3	2/3	3/8
Zn	2b	1/3	2/3	1.00
Cu	2b	1/3	2/3	1.00
Sn	2b	1/3	2/3	1.00

Chen et al. [158] have shown that the kesterite structure of CZTSe can be derived from zinc-blende type ZnSe by substituting Zn^{2+} atoms with Cu^+ , Zn^{2+} and Sn^{4+} . Hereby we simulated diffraction pattern from the wurtzite ZnSe by replacing Zn^{2+} atomic position with Cu^+ , Zn^{2+} and Sn^{4+} . The atomic ratio of Cu:Zn:Sn is 50:25:25.

Table S2: Atomic coordinates related to the wurtz-stannite type structure (4b is the general position (x, y, z) ; 2a is the position $(0, y, z)$). The structure is based on Cu_2ZnSiS_4 (ICSD-261267). The given values result from the Rietveld analysis.

Atom	Wyckhoff position	x	y	z
Cu	4b	0.7524	0.6780	0.1790
Zn	2a	0.00	0.8448	2/3
Sn	2a	0.00	0.1773	0.1697
Se	2a	0.00	0.86280	0.0635
Se	2a	0.00	0.1913	0.5144
Se	4b	0.7290	0.6645	0.5508

References

- [1] EMPA, A new world record for solar cell efficiency, in: Media Release, http://www.empa.ch/plugin/template/empa/*/131441, 2013.
- [2] K. Ito, t. Nakazawa, Electrical and optical properties of stannite type quaternary semiconducto thin films, *Japanese Journal of Applied Physics*, 27 (1988) 2094-2097.
- [3] D.B. Mitzi, O. Gunawan, T.K. Todorov, K. Wang, S. Guha, The path towards a high-performance solution-processed kesterite solar cell, *Solar Energy Materials & Solar Cells*, 95 (2011) 1421-1436.
- [4] T.K. Todorov, J. Tang, S. Bag, O. Gunawan, T. Gokmen, Y. Zhu, D.B. Mitzi, Beyond 11% Efficiency: Characteristics of State-of-the-Art $\text{Cu}_2\text{ZnSn}(\text{S},\text{Se})_4$ Solar Cells, *Advanced Energy Materials*, 3 (2013) 34-38.
- [5] H. Katagiri, K. Saitoh, T. Washio, H. Shinohara, T. Karumadani, S. Miyajima, Development of thin film solar cell based on $\text{Cu}_2\text{ZnSnS}_4$ thin films, *solar Energy Materials & Solar Cells*, 65 (2001) 141-148.
- [6] K. Moriya, K. Tanaka, H. Uchiki, Fabrication of $\text{Cu}_2\text{ZnSnS}_4$ Thin-Film Solar Cell Prepared by Pulsed Laser Deposition, *Japanese Journal of Applied Physics*, 46 (2007) 5780-5781.
- [7] T.K. Todorov, K.B. Reuter, D.B. Mitzi, High-Efficiency Solar Cell with Earth-Abundant Liquid-Processed Absorber, *Advanced Materials*, 22 (2010) E156-E159.
- [8] L. Guo, Y. Zhu, O. Gunawan, T. Gokmen, V.R. Deline, S. Ahmed, L.T. Romankiw, H. Deligianni, Electrodeposited $\text{Cu}_2\text{ZnSnSe}_4$ thin film solar cell with 7% power conversion efficiency, *Progress in Photovoltaics: Research and Applications*, (2013) DOI: 10.1002/pip.2332.
- [9] Q. Guo, G.M. Ford, W.-C. Yang, B.C. Walker, E.A. Stach, H.W. Hillhouse, R. Agrawal, Fabrication of 7.2% Efficient CZTSSe Solar Cells Using CZTS Nanocrystals, *Journal of the American Chemical Society*, 132 (2010) 17384-17386.
- [10] L. Kronik, Y. Shapira, Surface photovoltage phenomena theory experiment and applications, *Surface Science Reports*, 37 (1999) 1-206.

References

- [11] D. Cavalcoli, A. Cavallini, Surface photovoltage spectroscopy - method and applications, *Physica Status Solidi (c)*, 7 (2010) 1293-1300.
- [12] http://en.wikipedia.org/wiki/Abundance_of_elements_in_Earth's_crust.
- [13] C. Persson, Electronic and optical properties of $\text{Cu}_2\text{ZnSnS}_4$ and $\text{Cu}_2\text{ZnSnSe}_4$, *Journal of Applied Physics*, 107 (2010) 053710.
- [14] S. Schorr, The crystal structure of kesterite type compounds: A neutron and X-ray diffraction study, *Solar Energy Materials & Solar Cells*, 95 (2011) 1482-1488.
- [15] S. Chen, X.G. Gong, A. Walsh, S.-H. Wei, Crystal and electronic band structure of $\text{Cu}_{2}\text{ZnSnX}_{4}$ ($\text{X}=\text{S}$ and Se) photovoltaic absorbers: First-principles insights, *Applied Physics Letters*, 94 (2009) 041903.
- [16] H. Katagiri, N. Sasaguchi, S. Hando, S. Hoshino, J. Ohashi, T. Yokota, Preparation and evaluation of $\text{Cu}_2\text{ZnSnS}_4$ thin films by sulfurization of E-B evaporated precursors, *solar Energy Materials & Solar Cells*, 49 (1997) 407-414.
- [17] H. Katagiri, K. Jimbo, W.S. Maw, K. Oishi, M. Yamazaki, H. Araki, A. Takeuchi, Development of CZTS-based thin film solar cells, *Thin Solid Films*, 517 (2009) 2455-2460.
- [18] H. Katagiri, K. Jimbo, S. Yamada, T. Kamimura, W.S. Maw, T. Fukano, T. Ito, T. Motohiro, Enhanced Conversion Efficiencies of $\text{Cu}_2\text{ZnSnS}_4$ -Based Thin Film Solar Cells by Using Preferential Etching Technique, *Applied Physics Express*, 1 (2008) 041201.
- [19] D.B. Mitzi, M. Yuan, W. Liu, A.J. Kellock, S.J. Chey, V. Deline, A.G. Schrott, A High-Efficiency Solution-Deposited Thin-Film Photovoltaic Device, *Advanced Materials*, 20 (2008) 3657-3662.
- [20] S. Bag, O. Gunawan, T. Gokmen, Y. Zhu, T.K. Todorov, D.B. Mitzi, Low band gap liquid-processed CZTSe solar cell with 10.1% efficiency, *Energy & Environmental Science*, 5 (2012) 7060.
- [21] D.A.R. Barkhouse, O. Gunawan, T. Gokmen, T.K. Todorov, D.B. Mitzi, Device characteristics of a 10.1% hydrazine-processed $\text{Cu}_2\text{ZnSn}(\text{Se,S})_4$ solar cell, *Progress in Photovoltaics: Research and Applications*, 20 (2012) 6-11.
- [22] F. Liu, K. Zhang, Y. Lai, J. Li, Z. Zhang, Y. Liu, Growth and Characterization of $\text{Cu}_2\text{ZnSnS}_4$ Thin Films by DC Reactive Magnetron Sputtering for Photovoltaic Applications, *Electrochemical and Solid-State Letters*, 13 (2010) H379.

References

- [23] P.A. Fernandes, P.M.P. Salomé, A.F. da Cunha, B.-A. Schubert, Cu₂ZnSnS₄ solar cells prepared with sulfurized dc-sputtered stacked metallic precursors, *Thin Solid Films*, 519 (2011) 7382-7385.
- [24] T. Tanaka, T. Nagatomo, D. Kawasaki, M. Nishio, Q. Guo, A. Wakahara, A. Yoshida, H. Ogawa, Preparation of Cu₂ZnSnS₄ thin films by hybrid sputtering, *Journal of Physics and Chemistry of Solids*, 66 (2005) 1978-1981.
- [25] K. Jimbo, R. Kimura, T. Kamimura, S. Yamada, W.S. Maw, H. Araki, K. Oishi, H. Katagiri, Cu₂ZnSnS₄-type thin film solar cells using abundant materials, *Thin Solid Films*, 515 (2007) 5997-5999.
- [26] T. Fukano, S. Tajima, T. Ito, Enhancement of Conversion Efficiency of Cu₂ZnSnS₄ Thin Film Solar Cells by Improvement of Sulfurization Conditions, *Applied Physics Express*, 6 (2013) 062301.
- [27] P.A. Fernandes, P.M.P. Salomé, A.F. da Cunha, Precursors' order effect on the properties of sulfurized Cu₂ZnSnS₄ thin films, *Semiconductor Science and Technology*, 24 (2009) 105013.
- [28] R.B.V. Chalapathy, G.S. Jung, B.T. Ahn, Fabrication of Cu₂ZnSnS₄ films by sulfurization of Cu/ZnSn/Cu precursor layers in sulfur atmosphere for solar cells, *Solar Energy Materials & Solar Cells*, 95 (2011) 3216-3221.
- [29] B.-A. Schubert, B. Marsen, S. Cinque, T. Unold, R. Klenk, S. Schorr, H.-W. Schock, Cu₂ZnSnS₄ thin film solar cells by fast coevaporation, *Progress in Photovoltaics: Research and Applications*, 19 (2011) 93-96.
- [30] H. Katagiri, Cu₂ZnSnS₄ thin film solar cells, *Thin Solid Films*, 480-481 (2005) 426-432.
- [31] I. Repins, C. Beall, N. Vora, C. DeHart, D. Kuciauskas, P. Dippo, B. To, J. Mann, W.-C. Hsu, A. Goodrich, R. Noufi, Co-evaporated Cu₂ZnSnSe₄ films and devices, *Solar Energy Materials & Solar Cells*, 101 (2012) 154-159.
- [32] K. Wang, O. Gunawan, T. Todorov, B. Shin, S.J. Chey, N.A. Bojarczuk, D. Mitzi, S. Guha, Thermally evaporated Cu₂ZnSnS₄ solar cells, *Applied Physics Letters*, 97 (2010) 143508.
- [33] T. Tanaka, D. Kawasaki, M. Nishio, Q. Guo, H. Ogawa, Fabrication of Cu₂ZnSnS₄ thin films by co-evaporation, *Physica Status Solidi (c)*, 3 (2006) 2844-2847.

References

- [34] G. Suresh Babu, Y.B. Kishore Kumar, P. Uday Bhaskar, S. Raja Vanjari, Effect of Cu/(Zn+Sn) ratio on the properties of co-evaporated $\text{Cu}_2\text{ZnSnS}_4$ thin films, *Solar Energy Materials & Solar Cells*, 94 (2010) 221-226.
- [35] B. Shin, Y. Zhu, N.A. Bojarczuk, S. Jay Chey, S. Guha, Control of an interfacial MoSe_2 layer in $\text{Cu}_2\text{ZnSnS}_4$ thin film solar cells: 8.9% power conversion efficiency with a TiN diffusion barrier, *Applied Physics Letters*, 101 (2012) 053903.
- [36] B. Shin, O. Gunawan, Y. Zhu, N.A. Bojarczuk, S.J. Chey, S. Guha, Thin film solar cell with 8.4% power conversion efficiency using an earth-abundant $\text{Cu}_2\text{ZnSnS}_4$ absorber, *Progress in Photovoltaics: Research and Applications*, 21 (2013) 72-76.
- [37] T. Kobayashi, K. Jimbo, K. Tsuchida, S. Shinoda, T. Oyanagi, H. Katagiri, Investigation of $\text{Cu}_2\text{ZnSnS}_4$ -Based Thin Film Solar Cells Using Abundant Materials, *Japanese Journal of Applied Physics*, 44 (2005) 783-787.
- [38] R. Adhi Wibowo, E. Soo Lee, B. Munir, K. Ho Kim, Pulsed laser deposition of quaternary $\text{Cu}_2\text{ZnSnS}_4$ thin films, *Physica Status Solidi (a)*, 204 (2007) 3373-3379.
- [39] A.V. Moholkar, S.S. Shinde, A.R. Babar, K.-U. Sim, Y.-b. Kwon, K.Y. Rajpure, P.S. Patil, C.H. Bhosale, J.H. Kim, Development of CZTS thin films solar cells by pulsed laser deposition: Influence of pulse repetition rate, *Solar Energy*, 85 (2011) 1354-1363.
- [40] A.V. Moholkar, S.S. Shinde, G.L. Agawane, S.H. Jo, K.Y. Rajpure, P.S. Patil, C.H. Bhosale, J.H. Kim, Studies of compositional dependent CZTS thin film solar cells by pulsed laser deposition technique: An attempt to improve the efficiency, *Journal of Alloys and Compounds*, 544 (2012) 145-151.
- [41] K. Tanaka, N. Moritake, H. Uchiki, Preparation of $\text{Cu}_2\text{ZnSnS}_4$ thin films by sulfurizing sol-gel deposited precursors, *Solar Energy Materials & Solar Cells*, 91 (2007) 1199-1201.
- [42] K. Tanaka, M. Oonuki, N. Moritake, H. Uchiki, $\text{Cu}_2\text{ZnSnS}_4$ thin film solar cells prepared by non-vacuum processing, *Solar Energy Materials & Solar Cells*, 93 (2009) 583-587.
- [43] K. Tanaka, Y. Fukui, N. Moritake, H. Uchiki, Chemical composition dependence of morphological and optical properties of $\text{Cu}_2\text{ZnSnS}_4$ thin films deposited by sol-gel sulfurization and $\text{Cu}_2\text{ZnSnS}_4$ thin film solar cell efficiency, *Solar Energy Materials & Solar Cells*, 95 (2011) 838-842.

References

- [44] W. Ki, H.W. Hillhouse, Earth-Abundant Element Photovoltaics Directly from Soluble Precursors with High Yield Using a Non-Toxic Solvent, *Advanced Energy Materials*, 1 (211) 732-735.
- [45] C.M. Fella, A.R. Uhl, Y.E. Romanyuk, A.N. Tiwari, Cu₂ZnSnSe₄ absorbers processed from solution deposited metal salt precursors under different selenization conditions, *Physica Status Solidi (a)*, 209 (2012) 1043-1048.
- [46] N. Nakayama, K. Ito, Sprayed films of stannite Cu₂ZnSnS₄, *Applied Surface Science*, 92 (1996) 171-175.
- [47] J. Madarász, P. Bombicz, M. Okuya, S. Kaneko, <Thermal decomposition of thiourea complexes of Cu(I), Zn(II), and Sn(II) chlorides as precursors for the spray pyrolysis deposition of sulfide thin films.pdf>, *Solid State Ionics*, 141-142 (2001) 439-446.
- [48] N. Kamoun, H. Bouzouita, B. Rezig, Fabrication and characterization of Cu₂ZnSnS₄ thin films deposited by spray pyrolysis technique, *Thin Solid Films*, 515 (2007) 5949-5952.
- [49] Y.B.K. Kumar, G.S. Babu, P.U. Bhaskar, V.S. Raja, Effect of starting-solution pH on the growth of Cu₂ZnSnS₄ thin films deposited by spray pyrolysis, *Physica Status Solidi (a)*, 206 (2009) 1525-1530.
- [50] Y.B.K. Kumar, P.U. Bhaskar, G.S. Babu, V.S. Raja, Effect of copper salt and thiourea concentrations on the formation of Cu₂ZnSnS₄ thin films by spray pyrolysis, *Physica Status Solidi (a)*, 207 (2010) 149-156.
- [51] V.G. Rajeshmon, C.S. Kartha, K.P. Vijayakumar, C. Sanjeeviraja, T. Abe, Y. Kashiwaba, Role of precursor solution in controlling the opto-electronic properties of spray pyrolysed Cu₂ZnSnS₄ thin films, *Solar Energy*, 85 (2011) 249-255.
- [52] V.G. Rajeshmon, C.S. Kartha, K.P. Vijayakumar, A.B. Garg, R. Mittal, R. Mukhopadhyay, Spray Pyrolysed Cu₂ZnSnS₄ Solar Cell Using Cadmium Free Buffer Layer, *AIP Conference Proceedings*, 1349 (2011) 683-684.
- [53] J.J. Scragg, P.J. Dale, L.M. Peter, G. Zoppi, I. Forbes, New routes to sustainable photovoltaics: evaluation of Cu₂ZnSnS₄ as an alternative absorber material, *Physica Status Solidi (b)*, 245 (2008) 1772-1778.
- [54] J.J. Scragg, D.M. Berg, P.J. Dale, A 3.2% efficient Kesterite device from electrodeposited stacked elemental layers, *Journal of Electroanalytical Chemistry*, 646 (2010) 52-59.

References

- [55] S. Ahmed, K.B. Reuter, O. Gunawan, L. Guo, L.T. Romankiw, H. Deligianni, A High Efficiency Electrodeposited Cu₂ZnSnS₄ Solar Cell, *Advanced Energy Materials*, 2 (2012) 253-259.
- [56] A. Ennaoui, M. Lux-Steiner, A. Weber, D. Abou-Ras, I. Kötschau, H.W. Schock, R. Schurr, A. Hölzing, S. Jost, R. Hock, T. Voß, J. Schulze, A. Kirbs, Cu₂ZnSnS₄ thin film solar cells from electroplated precursors: Novel low-cost perspective, *Thin Solid Films*, 517 (2009) 2511-2514.
- [57] H. Araki, Y. Kubo, K. Jimbo, W.S. Maw, H. Katagiri, M. Yamazaki, K. Oishi, A. Takeuchi, Preparation of Cu₂ZnSnS₄ thin films by sulfurization of co-electroplated Cu-Zn-Sn precursors, *Physica Status Solidi (c)*, 6 (2009) 1266-1268.
- [58] C. Steinhagen, M.G. Panthani, V.A. Akhavan, B.W. Goodfellow, B. Koo, B.A. Korgel, Synthesis of Cu₂ZnSnS₄ Nanocrystals for Use in Low-Cost Photovoltaics, *Journal of the American Chemical Society*, 131 (2009) 12554-12555.
- [59] Q. Guo, H.W. Hillhouse, R. Agrawal, Synthesis of Cu₂ZnSnS₄ nanocrystal ink and its use for solar cells, *Journal of the American Chemical Society*, 131 (2009) 11672-11673.
- [60] Q. Tian, X. Xu, L. Han, M. Tang, R. Zou, Z. Chen, M. Yu, J. Yang, J. Hu, Hydrophilic Cu₂ZnSnS₄ nanocrystals for printing flexible, low-cost and environmentally friendly solar cells, *CrystEngComm*, 14 (2012) 3847.
- [61] K. Woo, Y. Kim, J. Moon, A non-toxic, solution-processed, earth abundant absorbing layer for thin-film solar cells, *Energy & Environmental Science*, 5 (2012) 5340.
- [62] J. Park, J. Joo, S.G. Kwon, Y. Jang, T. Hyeon, Synthesis of Monodisperse Spherical Nanocrystals, *Angewandte Chemie International Edition*, 46 (2007) 4630-4660.
- [63] C. Burda, X. Chen, R. Narayanan, M.A. El-Sayed, Chemistry and Properties of Nanocrystals of Different Shapes, *Chemical Reviews*, 105 (2005) 1025-1102.
- [64] N.D.J. Murray C. B., Bawendi M. G., <Synthesis and characterization of nearly monodisperse CdE (E = sulfur, selenium, tellurium) semiconductor nanocrystallites, *J. Am. Chem. Soc.*, 115 (1993) 8706–8715.
- [65] Q. Dai, D. Li, J. Chang, Y. Song, S. Kan, H. Chen, B. Zou, W. Xu, S. Xu, B. Liu, G. Zou, Facile synthesis of magic-sized CdSe and CdTe nanocrystals with tunable existence periods, *Nanotechnology*, 18 (2007) 405603.

References

- [66] Z. Adam Peng, X. Peng, <Formation of High-Quality CdTe, CdSe, and CdS Nanocrystals Using CdO as Precursor>, *J. Am. Chem. Soc.*, 123 (2001) 183-184.
- [67] Xiaogang Peng, J. Wickham, and A. P. Alivisatos, <Kinetics of II-VI and III-V Colloidal Semiconductor Nanocrystal Growth “Focusing” of Size Distributions">, *J. Am. Chem. Soc.*, 120 (1998) 5343–5344.
- [68] Lin Song Li, Narayan Pradhan, Yunjun Wang, and Xiaogang Peng, <High Quality ZnSe and ZnS Nanocrystals Formed by Activating Zinc Carboxylate Precursors>, *Nano Lett.*, 4 (2004) 2261-2264.
- [69] M.E. Norako, R.L. Brutchey, Synthesis of Metastable Wurtzite CuInSe₂ Nanocrystals, *Chemistry of Materials*, 22 (2010) 1613-1615.
- [70] Q. Guo, S.J. Kim, M. Kar, W.N. Shafarman, R.W. Birkmire, E.a. Stach, R. Agrawal, H.W. Hillhouse, <Development of CuInSe₂ Nanocrystal and Nanoring Inks for Low-Cost Solar Cells>, *Nano Lett.*, 8 (2008) 2982-2987.
- [71] Q. Guo, H.W. Hillhouse, R. Agrawal, <Synthesis of Cu₂ZnSnS₄ nanocrystal ink and its use for solar cells>, *J. Am. Chem. Soc.*, 131 (2009) 11672-11673.
- [72] S.C. Riha, B.a. Parkinson, A.L. Prieto, <Solution-Based Synthesis and Characterization of Cu₂ZnSnS₄ Nanocrystals.pdf>, *J. Am. Chem. Soc.*, 131 (2009) 12054-12055.
- [73] Y.A. Yang, H. Wu, K.R. Williams, Y.C. Cao, Synthesis of CdSe and CdTe Nanocrystals without Precursor Injection, *Angewandte Chemie International Edition*, 44 (2005) 6712-6715.
- [74] Victor K. LaMer, R.H. Dinegar, <Theory, Production and Mechanism of Formation of Monodispersed Hydrosols.pdf>, *J. Am. Chem. Soc.*, 72 (1950) 4847–4854.
- [75] S.C. Riha, <Tuning optoelectronic properties and understanding charge transport in nanocrystals thin films of earth abundant semiconducting materials>, PhD thesis, Colorado State University, (2011).
- [76] Y. Yin, A.P. Alivisatos, Colloidal nanocrystal synthesis and the organic–inorganic interface, *Nature*, 437 (2005) 664-670.
- [77] J.J. Jung Ho Yu, Hyun Min Park, Sung-II Baik, Young Woon Kim, Sung Chul Kim, and Taeghwan Hyeon, <Synthesis of Quantum-Sized Cubic ZnS Nanorods by the Oriented Attachment Mechanism>, *J. Am. Chem. Soc.*, 127 (2005) 5662–5670.
- [78] X. Lin, A. Steigert, M.C. Lux-Steiner, A. Ennaoui, One-step solution-based synthesis and characterization of kuramite Cu₃SnS₄ nanocrystals, *RSC Advances*, 2 (2012) 9798-9800.

References

- [79] M. Bouaziz, J. Ouerfelli, M. Amlouk, S. Belgacem, Structural and optical properties of Cu_3SnS_4 sprayed thin films, *Physica Status Solidi (a)*, 204 (2007) 3354-3360.
- [80] H. Hu, Z. Liu, B. Yang, X. Chen, Y. Qian, Template-mediated growth of Cu_3SnS_4 nanoshell tubes, *Journal of Crystal Growth*, 284 (2005) 226-234.
- [81] P.A. Fernandes, P.M.P. Salomé, A.F. da Cunha, $\text{Cu}_x\text{SnS}_{x+1}$ ($x = 2, 3$) thin films grown by sulfurization of metallic precursors deposited by dc magnetron sputtering, *physica status solidi (c)*, 7 (2010) 901-904.
- [82] J. Joo, H.B. Na, T. Yu, J.H. Yu, Y.W. Kim, F. Wu, J.Z. Zhang, T. Hyeon, Generalized and Facile Synthesis of Semiconducting Metal Sulfide Nanocrystals, *Journal of the American Chemical Society*, 125 (2003) 11100-11105.
- [83] A. Tubtimtae, M.-W. Lee, G.-J. Wang, Ag_2Se quantum-dot sensitized solar cells for full solar spectrum light harvesting, *Journal of Power Sources*, 196 (2011) 6603-6608.
- [84] N.J.J. Johnson, A. Korinek, C. Dong, F.C.J.M. van Veggel, Self-Focusing by Ostwald Ripening: A Strategy for Layer-by-Layer Epitaxial Growth on Upconverting Nanocrystals, *Journal of the American Chemical Society*, 134 (2012) 11068-11071.
- [85] Y.Z. Haizheng Zhong, Mingfu Ye, Youjun He, Jianping Ye, Chang He, Chunhe Yang, and Yongfang Li, <Controlled Synthesis and Optical Properties of Colloidal Ternary Chalcogenide CuInS_2 Nanocrystals.pdf>, *Chemistry of Materials*, 20 (2008) 6434-6443.
- [86] L. Tian, J.J. Vittal, Synthesis and characterization of ternary AgInS_2 nanocrystals by dual- and multiple-source methods, *New Journal of Chemistry*, 31 (2007) 2083-2087.
- [87] M. Ibáñez, P. Guardia, A. Shavel, D. Cadavid, J. Arbiol, J.R. Morante, A. Cabot, Growth Kinetics of Asymmetric Bi_2S_3 Nanocrystals: Size Distribution Focusing in Nanorods, *The Journal of Physical Chemistry C*, 115 (2011) 7947-7955.
- [88] Q. Guo, G.M. Ford, W.-C. Yang, C.J. Hages, H.W. Hillhouse, R. Agrawal, Enhancing the performance of CZTSSe solar cells with Ge alloying, *Solar Energy Materials & Solar Cells*, 105 (2012) 132-136.
- [89] Y. Cao, M.S. Denny, J.V. Caspar, W.E. Farneth, Q. Guo, A.S. Ionkin, L.K. Johnson, M. Lu, I. Malajovich, D. Radu, H.D. Rosenfeld, K.R. Choudhury, W. Wu, High-Efficiency Solution-Processed $\text{Cu}_2\text{ZnSn}(\text{S},\text{Se})_4$ Thin-Film Solar Cells Prepared from Binary and Ternary Nanoparticles, *Journal of the American Chemical Society*, 134 (2012) 15644-15647.

References

- [90] I.D. Olekseyuk, I.V. Dudchak, L.V. Piskach, Phase equilibria in the $\text{Cu}_2\text{S}-\text{ZnS}-\text{SnS}_2$ system, *Journal of Alloys and Compounds*, 368 (2004) 135-143.
- [91] I.V. Dudchak, L.V. Piskach, Phase equilibria in the $\text{Cu}_2\text{SnSe}_3-\text{SnSe}_2-\text{ZnSe}$ system, *Journal of Alloys and Compounds*, 351 (2003) 145-150.
- [92] A. Weber, R. Mainz, H.W. Schock, On the Sn loss from thin films of the material system $\text{Cu}-\text{Zn}-\text{Sn}-\text{S}$ in high vacuum, *Journal of Applied Physics*, 107 (2010) 013516.
- [93] J.J. Scragg, T. Ericson, T. Kubart, M. Edoff, C. Platzer-Björkman, Chemical Insights into the Instability of $\text{Cu}_2\text{ZnSnS}_4$ Films during Annealing, *Chemistry of Materials*, 23 (2011) 4625-4633.
- [94] A. Redinger, D.M. Berg, P.J. Dale, S. Susanne, The Consequences of Kesterite Equilibria for Efficient Solar Cells-Supporting information, *Journal of the American Chemical Society*, 133 (2011) 3320-3323.
- [95] S. Schorr, A. Weber, V. Honkimäki, H.-W. Schock, In-situ investigation of the kesterite formation from binary and ternary sulphides, *Thin Solid Films*, 517 (2009) 2461-2464.
- [96] W.-C. Hsu, B. Bob, W. Yang, C.-H. Chung, Y. Yang, Reaction pathways for the formation of $\text{Cu}_2\text{ZnSn}(\text{Se},\text{S})_4$ absorber materials from liquid-phase hydrazine-based precursor inks, *Energy & Environmental Science*, 5 (2012) 8564.
- [97] S. Siebentritt, S. Schorr, Kesterites-a challenging material for solar cells, *Progress in Photovoltaics: Research and Applications*, 20 (2012) 512-519.
- [98] N. Momose, M.T. Htay, K. Sakurai, S. Iwano, Y. Hashimoto, K. Ito, $\text{Cu}_2\text{ZnSnS}_4$ Thin-Film Solar Cells Utilizing Simultaneous Reaction of a Metallic Precursor with Elemental Sulfur and Selenium Vapor Sources, *Applied Physics Express*, 5 (2012) 081201.
- [99] L. Vegard, Die Konstitution der Mischkristalle und die Raumffüllung der Atome, *Zeitschrift für Physik*, 5 (1921) 17-26.
- [100] P.A. Fernandes, P.M.P. Salomé, A.F. da Cunha, Growth and Raman scattering characterization of $\text{Cu}_2\text{ZnSnS}_4$ thin films, *Thin Solid Films*, 517 (2009) 2519-2523.
- [101] A. Redinger, K. Hönes, X. Fontané, V. Izquierdo-Roca, E. Saucedo, N. Valle, A. Pérez-Rodríguez, S. Siebentritt, Detection of a ZnSe secondary phase in coevaporated $\text{Cu}_2\text{ZnSnSe}_4$ thin films, *Applied Physics Letters*, 98 (2011) 101907.

References

- [102] A.J. Cheng, M. Manno, A. Khare, C. Leighton, S.A. Campbell, E.S. Aydil, Imaging and phase identification of $\text{Cu}_2\text{ZnSnS}_4$ thin films using confocal Raman spectroscopy, *Journal of Vacuum Science & Technology A: Vacuum, Surfaces, and Films*, 29 (2011) 051203.
- [103] N. Vora, J. Blackburn, I. Repins, C. Beall, B. To, J. Pankow, G. Teeter, M. Young, R. Noufi, Phase identification and control of thin films deposited by co-evaporation of elemental Cu, Zn, Sn, and Se, *Journal of Vacuum Science & Technology A: Vacuum, Surfaces, and Films*, 30 (2012) 051201.
- [104] M. Himmrich, H. Haeuseler, Far infrared studies on stannite and wurtzstannite type compounds, *Spectrochimica Acta*, 47 (1991) 933-942.
- [105] P.K. Sarswat, M.L. Free, A. Tiwari, Temperature-dependent study of the Raman A mode of $\text{Cu}_2\text{ZnSnS}_4$ thin films, *Physica Status Solidi (b)*, (2011) 2170-2174.
- [106] T. Gürel, C. Sevik, T. Çağın, Characterization of vibrational and mechanical properties of quaternary compounds $\text{Cu}_2\text{ZnSnS}_4$ and $\text{Cu}_2\text{ZnSnSe}_4$ in kesterite and stannite structures, *Physical Review B*, 84 (2011) 205201.
- [107] X. Fontané, V. Izquierdo-Roca, E. Saucedo, S. Schorr, V.O. Yukhymchuk, M.Y. Valakh, A. Pérez-Rodríguez, J.R. Morante, Vibrational properties of stannite and kesterite type compounds: Raman scattering analysis of $\text{Cu}_2(\text{Fe,Zn})\text{SnS}_4$, *Journal of Alloys and Compounds*, 539 (2012) 190-194.
- [108] X. Fontané, L. Calvo-Barrío, V. Izquierdo-Roca, E. Saucedo, A. Pérez-Rodríguez, J.R. Morante, D.M. Berg, P.J. Dale, S. Siebentritt, In-depth resolved Raman scattering analysis for the identification of secondary phases: Characterization of $\text{Cu}_2\text{ZnSnS}_4$ layers for solar cell applications, *Applied Physics Letters*, 98 (2011) 181905.
- [109] H. Yoo, J. Kim, Growth of $\text{Cu}_2\text{ZnSnS}_4$ thin films using sulfurization of stacked metallic films, *Thin Solid Films*, 518 (2010) 6567-6572.
- [110] D. Papadimitriou, N. Esser, C. Xue, Structural properties of chalcopyrite thin films studied by Raman spectroscopy, *Physica Status Solidi (b)*, 242 (2005) 2633-2643.
- [111] J. He, L. Sun, S. Chen, Y. Chen, P. Yang, J. Chu, Composition dependence of structure and optical properties of $\text{Cu}_2\text{ZnSn}(\text{S,Se})_4$ solid solutions: An experimental study, *Journal of Alloys and Compounds*, 511 (2012) 129-132.
- [112] C. Zou, L. Zhang, D. Lin, Y. Yang, Q. Li, X. Xu, X.a. Chen, S. Huang, Facile synthesis of $\text{Cu}_2\text{ZnSnS}_4$ nanocrystals, *CrystEngComm*, 13 (2011) 3310-3313.

References

- [113] J. He, L. Sun, K. Zhang, W. Wang, J. Jiang, Y. Chen, P. Yang, J. Chu, Effect of post-sulfurization on the composition, structure and optical properties of $\text{Cu}_2\text{ZnSnS}_4$ thin films deposited by sputtering from a single quaternary target, *Applied Surface Science*, 264 (2013) 133-138.
- [114] H. Chandrasekhar, R. Humphreys, U. Zwick, M. Cardona, Infrared and Raman spectra of the IV-VI compounds SnS and SnSe , *Physical Review B*, 15 (1977) 2177-2183.
- [115] P. Sinsersuksakul, J. Heo, W. Noh, A.S. Hock, R.G. Gordon, Atomic Layer Deposition of Tin Monosulfide Thin Films, *Advanced Energy Materials*, 1 (2011) 1116-1125.
- [116] P.A. Fernandes, P.M.P. Salomé, A.F.d. Cunha, A study of ternary Cu_2SnS_3 and Cu_3SnS_4 thin films prepared by sulfurizing stacked metal precursors, *Journal of Physics D: Applied Physics*, 43 (2010) 215403.
- [117] A.J.M. Smith, P E; , W.Y. and Liang, Raman scattering studies of SnS_2 and SnSe_2 ., *J. Phys. C: Solid State Phys.*, 10 (1977) 1321-1333.
- [118] O.P. Agnihotri, A.K. Garg, H.K. Sehgal, Laser excited Raman spectrum of SnSe_2 , *Solid State Communications*, 17 (1975) 1537-1540.
- [119] A. Nag, M.V. Kovalenko, J.-S. Lee, W. Liu, B. Spokoyny, D.V. Talapin, Metal-free Inorganic Ligands for Colloidal Nanocrystals: S^{2-} , HS^- , Se^{2-} , HSe^- , Te^{2-} , HTe^- , TeS_3^{2-} , OH^- , and NH_2^- as Surface Ligands, *Journal of the American Chemical Society*, 133 (2011) 10612-10620.
- [120] H. Zhang, B. Hu, L. Sun, R. Hovden, F.W. Wise, D.A. Muller, R.D. Robinson, Surfactant Ligand Removal and Rational Fabrication of Inorganically Connected Quantum Dots, *Nano Letters*, 11 (2011) 5356-5361.
- [121] Y. Cao, M.S. Denny, J.V. Caspar, W.E. Farneth, Q. Guo, A.S. Ionkin, L.K. Johnson, M. Lu, I. Malajovich, D. Radu, H.D. Rosenfeld, K.R. Choudhury, W. Wu, High-Efficiency Solution-Processed $\text{Cu}_2\text{ZnSn}(\text{S},\text{Se})_4$ Thin-Film Solar Cells Prepared from Binary and Ternary Nanoparticles, *Journal of the American Chemical Society*, 134 (2012) 15644-15647.
- [122] J.I. Pankove, Optical process in semiconductors, in, Dover Publications, New York, 1971.
- [123] F. Luckert, D.I. Hamilton, M.V. Yakushev, N.S. Beattie, G. Zoppi, M. Moynihan, I. Forbes, A.V. Karotki, A.V. Mudryi, M. Grossberg, J. Krustok, R.W. Martin, Optical properties of high quality $\text{Cu}_2\text{ZnSnSe}_4$ thin films, *Applied Physics Letters*, 99 (2011) 062104.

References

- [124] K. Tanaka, Y. Miyamoto, H. Uchiki, K. Nakazawa, H. Araki, Donor-acceptor pair recombination luminescence from $\text{Cu}_2\text{ZnSnS}_4$ bulk single crystals, *Physica Status Solidi (a)*, 203 (2006) 2891-2896.
- [125] Y. Miyamoto, K. Tanaka, M. Oonuki, N. Moritake, H. Uchiki, Optical Properties of $\text{Cu}_2\text{ZnSnS}_4$ Thin Films Prepared by Sol-Gel and Sulfurization Method, *Japanese Journal of Applied Physics*, 47 (2008) 596-597.
- [126] K. Hönes, E. Zscherpel, J. Scragg, S. Siebentritt, Shallow defects in $\text{Cu}_2\text{ZnSnS}_4$, *Physica B: Condensed Matter*, 404 (2009) 4949-4952.
- [127] M. Grossberg, J. Krustok, K. Timmo, M. Altosaar, Radiative recombination in $\text{Cu}_2\text{ZnSnSe}_4$ monograins studied by photoluminescence spectroscopy, *Thin Solid Films*, 517 (2009) 2489-2492.
- [128] M. Grossberg, J. Krustok, J. Raudoja, K. Timmo, M. Altosaar, T. Raadik, Photoluminescence and Raman study of $\text{Cu}_2\text{ZnSn}(\text{SexS}_{1-x})_4$ monograins for photovoltaic applications, *Thin Solid Films*, 519 (2011) 7403-7406.
- [129] M. Grossberg, J. Krustok, J. Raudoja, T. Raadik, The role of structural properties on deep defect states in $\text{Cu}_2\text{ZnSnS}_4$ studied by photoluminescence spectroscopy, *Applied Physics Letters*, 101 (2012) 102102.
- [130] S. Levchenko, V.E. Tezlevan, E. Arushanov, S. Schorr, T. Unold, Free-to-bound recombination in near stoichiometric $\text{Cu}_2\text{ZnSnS}_4$ single crystals, *Physical Review B*, 86 (2012) 045206.
- [131] J.P. Leitão, N.M. Santos, P.A. Fernandes, P.M.P. Salomé, A.F. da Cunha, J.C. González, G.M. Ribeiro, F.M. Matinaga, Photoluminescence and electrical study of fluctuating potentials in $\text{Cu}_2\text{ZnSnS}_4$ -based thin films, *Physical Review B*, 84 (2011) 024120.
- [132] X. Lin, J. Kavalakkatt, K. Kornhuber, S. Levchenko, M.C. Lux-Steiner, A. Ennaoui, Structural and optical properties of $\text{Cu}_2\text{ZnSnS}_4$ thin film absorbers from ZnS and Cu_3SnS_4 nanoparticle precursors, *Thin Solid Films*, (2012).
- [133] S. Chen, A. Walsh, J.-H. Yang, X.G. Gong, L. Sun, P.-X. Yang, J.-H. Chu, S.-H. Wei, Compositional dependence of structural and electronic properties of $\text{Cu}_2\text{ZnSn}(\text{S,Se})_4$ alloys for thin film solar cells, *Physical Review B*, 83 (2011).

References

- [134] S.C. Riha, B.A. Parkinson, A.L. Prieto, Compositionally Tunable $\text{Cu}_2\text{ZnSn}(\text{S}_{1-x}\text{Se}_x)_4$ Nanocrystals: Probing the Effect of Se-Inclusion in Mixed Chalcogenide Thin Films, *Journal of the American Chemical Society*, 133 (2011) 15272-15275.
- [135] R. Dingle, Radiative Lifetimes of Donor-Acceptor Pairs in p-Type Gallium Arsenide, *Physical Review*, 184 (1969) 788-796.
- [136] D. Thomas, J. Hopfield, W. Augustyniak, Kinetics of Radiative Recombination at Randomly Distributed Donors and Acceptors, *Physical Review*, 140 (1965) A202-A220.
- [137] J.r. Krustok, H. Collan, K. Hjelt, Does the low-temperature Arrhenius plot of the photoluminescence intensity in CdTe point towards an erroneous activation energy?, *Journal of Applied Physics*, 81 (1997) 1442.
- [138] S. Chen, A. Walsh, X.-G. Gong, S.-H. Wei, Classification of Lattice Defects in the Kesterite $\text{Cu}_2\text{ZnSnS}_4$ and $\text{Cu}_2\text{ZnSnSe}_4$ Earth-Abundant Solar Cell Absorbers, *Advanced Materials*, (2013) 1522-1539.
- [139] X.Z. Lin, T. Dittrich, S. Fengler, M.C. Lux-Steiner, A. Ennaoui, Correlation between processing conditions of $\text{Cu}_2\text{ZnSn}(\text{S}_x\text{Se}_{1-x})_4$ and modulated surface photovoltage, *Applied Physics Letters*, 102 (2013) 143903.
- [140] H.C. Gatos, Surface Photovoltage Spectroscopy—A New Approach to the Study of High-Gap Semiconductor Surfaces, *Journal of Vacuum Science and Technology*, 10 (1973) 130.
- [141] T. Dittrich, S. Bönisch, P. Zabel, S. Dube, High precision differential measurement of surface photovoltage transients on ultrathin CdS layers, *Review of Scientific Instruments*, 79 (2008) 113903.
- [142] A.M. Goodman, A Method for the Measurement of Short Minority Carrier Diffusion Lengths in Semiconductors, *Journal of Applied Physics*, 32 (1961) 2550.
- [143] B. Johnson, J. Klaer, C.H. Fischer, I. Lauermann, Depth profiling of a CdS buffer layer on CuInS_2 measured with X-ray photoelectron spectroscopy during removal by HCl etching, *Thin Solid Films*, 520 (2012) 2829-2832.
- [144] V. Duzhko, V. Timoshenko, F. Koch, T. Dittrich, Photovoltage in nanocrystalline porous TiO_2 , *Physical Review B*, 64 (2001) 075204.
- [145] S. Levenco, D. Dumcenco, Y.P. Wang, Y.S. Huang, C.H. Ho, E. Arushanov, V. Tezlevan, K.K. Tiong, Influence of anionic substitution on the electrolyte electroreflectance

References

study of band edge transitions in single crystal $\text{Cu}_2\text{ZnSn}(\text{S}_x\text{Se}_{1-x})_4$ solid solutions, *Optical Materials*, 34 (2012) 1362-1365.

[146] S. Chen, J.-h. Yang, X.G. Gong, A. Walsh, S.-h. Wei, Intrinsic point defects and complexes in the quaternary kesterite semiconductor $\text{Cu}_2\text{ZnSnS}_4$, *Physical Review B*, 81 (2010) 245204.

[147] M.A. Green, K. Emery, Y. Hishikawa, W. Warta, Solar cell efficiency tables (version 33), *Progress in Photovoltaics: Research and Applications*, 17 (2009) 85-94.

[148] P. Pistor, Formation and Electronic Properties of $\text{In}_2\text{S}_3/\text{Cu}(\text{In,Ga})\text{Se}_2$ Junctions and Related Thin Film Solar Cells, PhD Thesis, Freien Universität Berlin, (2009).

[149] O. Gunawan, T.K. Todorov, D.B. Mitzi, Loss mechanisms in hydrazine-processed $\text{Cu}_2\text{ZnSn}(\text{Se,S})_4$ solar cells, *Applied Physics Letters*, 97 (2010) 233506.

[150] V. Nadenau, U. Rau, A. Jasenek, H.W. Schock, Electronic properties of CuGaSe [sub 2]-based heterojunction solar cells. Part I. Transport analysis, *Journal of Applied Physics*, 87 (2000) 584.

[151] O. Gunawan, T.K. Todorov, D.B. Mitzi, Loss mechanisms in hydrazine-processed $\text{Cu}_2\text{ZnSn}(\text{Se,S})_4$ solar cells, *Applied Physics Letters*, 97 (2010) 233506.

[152] X. Lin, J. Kavalakkatt, K. Kornhuber, D. Abou-Ras, S. Schorr, M.C. Lux-Steiner, A. Ennaoui, Synthesis of $\text{Cu}_2\text{Zn}_x\text{Sn}_y\text{Se}_{1+x+2y}$ nanocrystals with wurtzite-derived structure, *RSC Advances*, 2 (2012) 9894.

[153] S. Ahn, S. Jung, J. Gwak, A. Cho, K. Shin, K. Yoon, D. Park, H. Cheong, J.H. Yun, Determination of band gap energy E_g of $\text{Cu}_2\text{ZnSnSe}_4$ thin films: On the discrepancies of reported band gap values, *Applied Physics Letters*, 97 (2010) 021905.

[154] Y.B. Kishore Kumar, G. Suresh Babu, P. Uday Bhaskar, V. Sundara Raja, Preparation and characterization of spray-deposited $\text{Cu}_2\text{ZnSnS}_4$ thin films, *Solar Energy Materials & Solar Cells*, 93 (2009) 1230-1237.

[155] H.W. Hillhouse, M.C. Beard, Solar cells from colloidal nanocrystals: Fundamentals, materials, devices, and economics, *Current Opinion in Colloid & Interface Science*, 14 (2009) 245-259.

[156] S.E. Habas, H.a.S. Platt, M.F.a.M. van Hest, D.S. Ginley, Low-Cost Inorganic Solar Cells From Ink To Printed Device, *Chemical Reviews*, 110 (2010) 6571-6594.

References

- [157] S. Nakamura, T. Maeda, T. Wada, Phase Stability and Electronic Structure of In-Free Photovoltaic Materials: $\text{Cu}_2\text{ZnSiSe}_4$, $\text{Cu}_2\text{ZnGeSe}_4$, and $\text{Cu}_2\text{ZnSnSe}_4$, *Japanese Journal of Applied Physics*, 49 (2010) 121203.
- [158] S. Chen, A. Walsh, Y. Luo, J.-H. Yang, X.G. Gong, S.-H. Wei, Wurtzite-derived polytypes of kesterite and stannite quaternary chalcogenide semiconductors, *Physical Review B*, 82 (2010) 1-8.
- [159] S.C. Riha, B.a. Parkinson, A.L. Prieto, Solution-Based Synthesis and Characterization of $\text{Cu}_2\text{ZnSnS}_4$ Nanocrystals, *Journal of the American Chemical Society*, 131 (2009) 12054-12055.
- [160] A. Shavel, J. Arbiol, A. Cabot, Synthesis of Quaternary Chalcogenide Nanocrystals Stannite $\text{Cu}_2\text{Zn}_x\text{Sn}_y\text{Se}_{1+x+2y}$, *Journal of the American Chemical Society*, 132 (2010) 4514-4515.
- [161] H. Wei, W. Guo, Y. Sun, Z. Yang, Y. Zhang, Hot-injection synthesis and characterization of quaternary $\text{Cu}_2\text{ZnSnSe}_4$ nanocrystals, *Materials Letters*, 64 (2010) 1424-1426.
- [162] W. Haas, T. Rath, A. Pein, J. Rattenberger, G. Trimmel, F. Hofer, The stoichiometry of single nanoparticles of copper zinc tin selenide, *Chemical Communications*, 47 (2011) 2050.
- [163] L. Shi, Q. Li, Thickness tunable $\text{Cu}_2\text{ZnSnSe}_4$ nanosheets, *CrystEngComm*, 13 (2011) 6507-6510.
- [164] X. Lu, Z. Zhuang, Q. Peng, Y. Li, Wurtzite $\text{Cu}_2\text{ZnSnS}_4$ nanocrystals: a novel quaternary semiconductor, *Chemical Communications*, 47 (2011) 3141.
- [165] A. Singh, H. Geaney, F. Laffir, K.M. Ryan, Colloidal Synthesis of Wurtzite $\text{Cu}_2\text{ZnSnS}_4$ Nanorods and Their Perpendicular Assembly, *Journal of the American Chemical Society*, 134 (2012) 2910-2913.
- [166] M.D. Regulacio, C. Ye, S.H. Lim, M. Bosman, E. Ye, S. Chen, Q.-H. Xu, M.-Y. Han, Colloidal Nanocrystals of Wurtzite-Type $\text{Cu}_2\text{ZnSnS}_4$: Facile Noninjection Synthesis and Formation Mechanism, *Chemistry - A European Journal*, 18 (2012) 3127-3131.
- [167] H. Jiang, P. Dai, Z. Feng, W. Fan, J. Zhan, Phase selective synthesis of metastable orthorhombic $\text{Cu}_2\text{ZnSnS}_4$, *Journal of Materials Chemistry*, 22 (2012) 7502.
- [168] J.-J. Wang, J.-S. Hu, Y.-G. Guo, L.-J. Wan, Wurtzite $\text{Cu}_2\text{ZnSnSe}_4$ nanocrystals for high-performance organic-inorganic hybrid photodetectors, *NPG Asia Materials*, 4 (2012) e2.

References

- [169] T. Rath, W. Haas, A. Pein, R. Saf, E. Maier, B. Kunert, F. Hofer, R. Resel, G. Trimmel, Synthesis and characterization of copper zinc tin chalcogenide nanoparticles: Influence of reactants on the chemical composition, *Solar Energy Materials & Solar Cells*, 101 (2012) 87-94.
- [170] J. Park, K. An, Y. Hwang, J.-G. Park, H.-J. Noh, J.-Y. Kim, J.-H. Park, N.-M. Hwang, T. Hyeon, Ultra-large-scale syntheses of monodisperse nanocrystals, *Nature Materials*, 3 (2004) 891-895.
- [171] J. Rodriguez-Carvajal, Recent advances in magnetic structure determination by neutron powder diffraction, *Physica B*, 192 (1993) 55-69.
- [172] L. Shi, C. Pei, Y. Xu, Q. Li, Template-Directed Synthesis of Ordered Single-Crystalline Nanowires Arrays of $\text{Cu}_2\text{ZnSnS}_4$ and $\text{Cu}_2\text{ZnSnSe}_4$, *Journal of the American Chemical Society*, 133 (2011) 10328-10331.
- [173] M. Altosaar, J. Raudoja, K. Timmo, M. Danilson, M. Grossberg, J. Krustok, E. Mellikov, $\text{Cu}_2\text{Zn}_{1-x}\text{Cd}_x\text{Sn}(\text{Se}_{1-y}\text{S}_y)_4$ solid solutions as absorber materials for solar cells, *Physica Status Solidi (a)*, 205 (2008) 167-170.

List of publications

Journal Publications

- **X. Z. Lin**, S. Fengler, Th. Dittrich, M. Ch. Lux-Steiner, A. Ennaoui, Correlation between processing conditions of $\text{Cu}_2\text{ZnSn}(\text{S}_x\text{Se}_{1-x})_4$ and modulated surface photovoltage, *Appl. Phys. Lett.*, 2013, **102**, 143903.
- **X. Z. Lin**, J. Kavalakkatt, K. Kornhuber, Sergiu Levenco, M. Ch.Lux-Steiner, and A. Ennaoui, Structural and optical properties of $\text{Cu}_2\text{ZnSnS}_4$ thin film absorbers from ZnS and Cu_3SnS_4 nanoparticle precursors, *Thin Solid Films*, 2013, 535, 10.
- **X. Z. Lin**, J. Kavalakkatt, K. Kornhuber, D. Abou-Ras, S. Schorr, M. Ch.Lux-Steiner, and A. Ennaoui, Synthesis of $\text{Cu}_2\text{Zn}_x\text{Sn}_y\text{Se}_{1+x+2y}$ Nanocrystals with Wurtzite-Derived Structure, *RSC Adv.*, 2012, 2, 9894.
- **X. Z. Lin**, A. Steigert, M. Ch. Lux-Steiner and A. Ennaoui, One-step Solution-based Synthesis and Characterization of Kuramite Cu_3SnS_4 Nanocrystals, *RSC Adv.*, 2012, 2, 9798.
- E. Zillner, A. Paul, J. Jutimoosik, S. Chandarak, T. Monnor, S. Rujirawat, R. Yimnirun, **X. Z. Lin**, A. Ennaoui, Th. Dittrich, M. Lux-Steiner, Lattice positions of Sn in $\text{Cu}_2\text{ZnSnS}_4$ nanoparticles and thin films studied by synchrotron X-ray absorption near edge structure analysis, *Appl. Phys. Lett.*, 2013, 102, 221908.
- K. Kornhuber, J. Kavalakkatt, **X. Z. Lin**, M. Ch.Lux-Steiner, and A. Ennaoui, In-Situ Monitoring of Electrophoretic Deposition of $\text{Cu}_2\text{ZnSnS}_4$ Nanocrystals, *RSC Adv.* 2013,**3**, 5845.
- J. Kavalakkatt, **X. Z. Lin**, K. Kornhuber, Patryk Kusch, A. Ennaoui, Stephanie Reich, M. Ch.Lux-Steiner, $\text{Cu}_2\text{ZnSn}(\text{S},\text{Se})_4$ from Cu_xSnS_y nanoparticle precursors on ZnO nanorod arrays, *Thin Solid Films*, 2013, 535, 380.

Conference Proceedings

- **X. Z. Lin**, J. Kavalakkatt, Th. Dittrich, M. Ch. Lux-Steiner, and A. Ennaoui, Next generation of low cost photovoltaics with Cu-Zn-Sn-S nanoparticle inks: correlation

List of publications

- between processing conditions of $\text{Cu}_2\text{ZnSn}(\text{S}_x\text{Se}_{1-x})_4$ and modulated surface photovoltage, *proceeding of 28th EU PVSEC*, 2013, 3BV, 2259 .
- **X. Z. Lin**, J. Kavalakkatt, M. Ch.Lux-Steiner and A. Ennaoui, Air-stable solution processing $\text{Cu}_2\text{ZnSn}(\text{S}_x\text{Se}_{1-x})_4$ thin film solar cells: influence of ink precursors and preparation process, *MRS Proceedings*, 2013, 1538, 107.
 - **X. Z. Lin**, J. Kavalakkatt, M. Ch.Lux-Steiner and A. Ennaoui, New formulation of Copper Zinc Tin Sulfide compounds: An Ink precursors route to printed photovoltaics, *proceeding of 27th EU PVSEC*, 2012, 3DV, 2794.
 - **X. Z. Lin**, J. Kavalakkatt, M. Ch.Lux-Steiner and A. Ennaoui, Thin-Film Solar Cell Absorber $\text{Cu}_2\text{ZnSnS}_4$ (CZTS) by Annealing of Monodisperse Kesterite Nanoparticle Precursors, *proceeding of 26th EU PVSEC*, 2011, 3DV, 2896.
 - J. Kavalakkatt, **X. Z. Lin**, A. Ennaoui, M. Ch.Lux-Steiner, Next Generation of Low Cost Photovoltaic: New concept with designed substrate/ZnO-NRs/barrier/CZTS structure, *proceeding of 28th EU PVSEC*, 2013, 3BV, 2362.

Curriculum Vitae

For reasons of dataprotection, the Curriculum Vitae is not included in the online version.

Declaration

Declaration

Ich erkläre an Eides Statt, dass die vorliegende Dissertation in allen Teilen von mir selbständig angefertigt wurde und die benutzten Hilfsmittel vollständig angegeben worden sind.